

Ab initio investigation of topological magnetism in two-dimensional van der Waals heterostructures

Nihad Abuawwad

Schlüsseltechnologien / Key Technologies

Band / Volume 291

ISBN 978-3-95806-808-7

Forschungszentrum Jülich GmbH
Peter Grünberg Institut (PGI)
Quanten-Theorie der Materialien (PGI-1)

Ab initio investigation of topological magnetism in two-dimensional van der Waals heterostructures

Nihad Abuawwad

Schriften des Forschungszentrums Jülich
Reihe Schlüsseltechnologien / Key Technologies

Band / Volume 291

ISSN 1866-1807

ISBN 978-3-95806-808-7

Bibliografische Information der Deutschen Nationalbibliothek.
Die Deutsche Nationalbibliothek verzeichnet diese Publikation in der
Deutschen Nationalbibliografie; detaillierte Bibliografische Daten
sind im Internet über <http://dnb.d-nb.de> abrufbar.

Herausgeber und Vertrieb: Forschungszentrum Jülich GmbH
Zentralbibliothek, Verlag
52425 Jülich
Tel.: +49 2461 61-5368
Fax: +49 2461 61-6103
zb-publikation@fz-juelich.de
www.fz-juelich.de/zb

Umschlaggestaltung: Grafische Medien, Forschungszentrum Jülich GmbH

Druck: Grafische Medien, Forschungszentrum Jülich GmbH

Copyright: Forschungszentrum Jülich 2025

Schriften des Forschungszentrums Jülich
Reihe Schlüsseltechnologien / Key Technologies, Band / Volume 291

D 464 (Diss. Duisburg-Essen, Univ., 2024)

ISSN 1866-1807
ISBN 978-3-95806-808-7

Vollständig frei verfügbar über das Publikationsportal des Forschungszentrums Jülich (JuSER)
unter www.fz-juelich.de/zb/openaccess.



This is an Open Access publication distributed under the terms of the [Creative Commons Attribution License 4.0](https://creativecommons.org/licenses/by/4.0/), which permits unrestricted use, distribution, and reproduction in any medium, provided the original work is properly cited.

Hiermit versichere ich, die vorliegende Dissertation selbstständig, ohne fremde Hilfe und ohne Benutzung anderer als den angegebenen Quellen angefertigt zu haben. Alle aus fremden Werken direkt oder indirekt übernommenen Stellen sind als solche gekennzeichnet. Die vorliegende Dissertation wurde in keinem anderen Promotionsverfahren eingereicht. Mit dieser Arbeit strebe ich die Erlangung des akademischen Grades Doktor der Naturwissenschaften (Dr. rer. nat.) an.

Ort, Datum

Author name (on the line the signature)

Acknowledgments

I express my sincere gratitude for the invaluable chance to work with Prof. Dr. Samir Lounis, whose guidance has been really remarkable. I cannot sufficiently express my appreciation for his consistent readiness to answer my questions and provide advice whenever I need it. His unwavering encouragement has kept me going despite the difficulties I have faced while conducting my studies, and his continual backing has strengthened my confidence. It was an honor to work with him, and I will always be grateful for the information and abilities I have acquired along the way.

I would like to express my sincere gratitude to Prof. Dr. Hongbin Zhang for agreeably acting as my thesis's second referee. His dedication to the academic community and expertise in my field is a true honor. I am grateful for his invaluable feedback and contributions that have enriched my work.

Dr. Hazem Abusara represents Birzeit University and serves as the Palestinian partner within the funding framework of my thesis. I am profoundly thankful for his unwavering support and expertise on this path. This research was made possible through funding from the German Federal Ministry of Education and Research (BMBF) via the Palestinian German Scientific Bridge (PGSB), and I extend my sincere gratitude to them for their invaluable support. Without their financial assistance, this research would not have been achievable. My heartfelt thanks to all who contributed to this project.

I am grateful to Dr. Manuel dos Santos Dias for his unwavering support since the inception of my work. His extensive knowledge, particularly in the theoretical background and programming, has significantly enriched my thesis. His contributions are immeasurable.

I wish to express my gratitude to Prof. Dr. Stefan Blügel for giving me the opportunity to conduct my thesis at his institute, "Quantum Theory of Materials," situated within the Peter Grünberg Institut. His consistent support and encouragement have played a pivotal role in my scientific journey. Moreover, I would also like to express my gratitude to the members of the Funsilab group.

A special acknowledgment goes to Mrs. Ute Winkler, and Ms. Yasmin Ergüven for their outstanding administrative support. Her prompt and dependable assistance has been indispensable in resolving administrative matters.

A special thanks to my friend and collaborator Yixuan Zhang from the Institute of Materials Science at Technical University Darmstadt, for his help with the machine learning part of

my thesis. I enjoyed working with him, and his support was invaluable.

I would like to express my sincere gratitude to my family for their constant encouragement during my academic career. Their support, love, and persistent trust in me have served as a constant source of motivation and inspiration. Having a family that has supported me through good times and bad is a true blessing. Your unwavering support has enabled us to do this.

Nihad AbuAwwad
2024

Abstract

Magnetism in two-dimensional (2D) van der Waals (vdW) materials is a rapidly evolving field in condensed matter physics and materials science, marked by intriguing discoveries and potential applications. Unlike traditional three-dimensional materials, 2D vdW materials are characterized by their ultra-thin, often single-layer, structure leading to unique magnetic properties triggered by proximity-effects, which are facilitated by the underlying vdW gap. Such properties are not only fundamental for understanding the physics of low-dimensional systems but also hold immense promise for the development of advanced technologies in data storage, spintronics, and quantum computing.

Building on the foundational understanding of magnetism in 2D materials, this thesis dives deeper into the specific case of CrTe₂ and CrSBr. Based on a multiscale modelling approach that combines first-principles calculations and a Heisenberg model supplied with ab-initio parameters, we report a strong magnetoelastic coupling in a free-standing monolayer of CrTe₂. We demonstrate that different crystal structures of a single CrTe₂ give rise to non-collinear magnetism through magnetic frustration and the emergence of the Dzyaloshinskii-Moriya interaction (DMI). Utilizing atomistic spin relaxation, we perform a detailed investigation of the complex magnetic properties pertaining to this 2D material impacted by the presence of various types of structural distortions akin to charge density waves.

Also, we demonstrate that interfacing a CrTe₂ layer with various Te-based layers enables the control of the magnetic exchange and Dzyaloshinskii-Moriya interactions as well as the magnetic anisotropy energy of the whole heterobilayer, and thereby the emergence of topological magnetic phases such as skyrmions and antiferromagnetic Néel merons. The latter are novel particles in the world of topological magnetism since they arise in a frustrated Néel magnetic environment and manifest as multiples of intertwined hexamer-textures. Our findings pave a promising road for proximity-induced engineering of both ferromagnetic and long-sought antiferromagnetic chiral objects in the very same 2D material, which is appealing for new information technology devices employing quantum materials.

Moreover, we demonstrate the all-electric switching of the topological nature of individual magnetic objects emerging in 2D vdW heterobilayers. We show that an external electric field modifies the vdW gap between CrTe₂ and (Rh, Ti)Te₂ layers and alters the underlying magnetic interactions. This enables switching between ferromagnetic skyrmions and meron pairs in the CrTe₂/RhTe₂ heterobilayer while it enhances the stability of frustrated antiferromagnetic merons in the CrTe₂/TiTe₂ heterobilayer. We envision that the electrical engineering of distinct topological magnetic solitons in a single device could pave the way for novel energy-efficient mechanisms to store and transmit information with applications in spintronics.

Finally, via machine learning concepts we integrated linear spin wave theory (LSWT) with active-learning sampling to develop a Kalman Filter Adversarial Bayesian Optimization (KFABO) algorithm. This algorithm excels at managing highly noisy experimental spectra of 2D bulk CrSBr, aiming to map the experimentally extracted magnon spectrum with minimal sampling points and iterations. Additionally, the KFABO algorithm is designed to accurately extract magnetic parameters from inelastic neutron scattering data, significantly enhancing the efficiency and accuracy of experimental measurements.

Zusammenfassung

Magnetismus in 2D-Materialien ist ein sich schnell entwickelndes Feld in der Physik der kondensierten Materie und Materialwissenschaft, ausgezeichnet durch faszinierende Entdeckungen und potenzielle Anwendungen. Im Gegensatz zu traditionellen 3D-Materialien zeichnen sich 2D-Materialien durch ihre ultradünne, oft einlagige Struktur aus, was zu einzigartigen magnetischen Eigenschaften führt. Solche Eigenschaften sind nicht nur grundlegend für das Verständnis der Physik von Systemen mit niedrigen Dimensionen, sondern versprechen die Entwicklung fortschrittlicher Technologien in der Datenspeicherung, Spintronik und Quantencomputer.

Aufbauend auf dem grundlegenden Verständnis des Magnetismus in 2D-Materialien, vertieft sich diese Arbeit in den spezifischen Fall von CrTe_2 . Basierend auf einem Multiskalen-Modellierungsansatz, der ab-initio-Verfahren und ein Heisenberg-Modell mit ab-initio-Parametern kombiniert, berichten wir über eine starke magnetoelastische Kopplung in einer freistehenden Monoschicht von CrTe_2 . Wir zeigen, dass verschiedene Kristallstrukturen eines einzelnen CrTe_2 durch magnetische Frustration und das Auftreten der Dzyaloshinskii-Moriya-Interaktion (DMI) zu nicht-kollinearem Magnetismus führen. Unter Verwendung von atomistischen Spin-Relaxationen führen wir eine detaillierte Untersuchung der komplexen magnetischen Eigenschaften dieses 2D-Materials durch, die von der Anwesenheit verschiedener Arten struktureller Verzerrungen, ähnlich den Ladungsdichtewellen, beeinflusst werden.

Außerdem zeigen wir, dass die Oberfläche einer CrTe_2 -Schicht mit verschiedenen Te-basierten Schichten die Kontrolle über die magnetische Austauschwechselwirkung und die Dzyaloshinskii-Moriya-Interaktion sowie die magnetische Anisotropieenergie der gesamten Heterodoppelschicht ermöglicht und damit das Auftreten topologischer magnetischer Phasen wie Skyrmionen und antiferromagnetischen Néel-Merons hervorbringt. Letztere sind neuartige Partikel in der Welt des topologischen Magnetismus, da sie in einer frustrierten Néel-magnetischen Umgebung entstehen und sich als Vielfache von ineinander verwobenen Hexamer-Texturen manifestieren. Unsere Erkenntnisse bahnen einen vielversprechenden Weg für die Entwicklung sowohl ferromagnetischer als auch lang gesuchter antiferromagnetischer chiraler Objekte im selben 2D-Material, was für neue Informationstechnologegeräte, die Quantenmaterialien verwenden, attraktiv ist.

Schließlich demonstrieren wir das rein elektrische Umschalten der topologischen Natur einzelner magnetischer Objekte, die in 2D-vdW-Heterodoppelschichten auftreten. Wir zeigen, dass ein externes elektrisches Feld den vdW-Abstand zwischen CrTe_2 und $(\text{Rh}, \text{Ti})\text{Te}_2$ -Schichten modifiziert und die zugrundeliegenden magnetischen Interaktionen verändert. Dies ermöglicht das Umschalten zwischen ferromagnetischen Skyrmionen und Meron-Paaren in der $\text{CrTe}_2/\text{RhTe}_2$ -Heterodoppelschicht, während es die Stabilität frustrierter antiferromagnetischer Merons in der $\text{CrTe}_2/\text{TiTe}_2$ -Heterodoppelschicht verbessert. Wir stellen uns vor, dass die elektrische Erzwingung verschiedener topologischer magnetischer Solitonen in einem einzigen Gerät den Weg für neuartige, energieeffiziente Mechanismen zur Speicherung und Übertragung von Informationen mit Anwendungen in der Spintronik ebnet könnte.

Schließlich haben wir die lineare Spinwellentheorie (LSWT) mit aktivem Lernasampling kombiniert, um einen Kalman-Filter-Adversarial-Bayesian-Optimierungsalgorithmus (KFABO) zu entwickeln. Dieser Algorithmus ist hervorragend geeignet, um hochrauschende experimentelle Spektren von 2D-Bulk- CrSBr zu handhaben, und zielt darauf ab, das experimentell extrahierte Magnonspektrum mit minimalen Abtastpunkten und Iterationen zu kartieren. Darüber hinaus ist der KFABO-Algorithmus darauf ausgelegt, magnetische Parameter aus inelastischen Neutronenstreuendaten genau zu extrahieren, was die Effizienz und Genauigkeit experimenteller Messungen erheblich verbessert.

List of publications

Publications related to the thesis

- Nihad Abuawwad, Yixuan Zhang, Samir Lounis, and Hongbin Zhang. Adversarial Bayesian optimization for active sampling in inelastic neutron spectroscopy. (Submitted to Nature Communications). <https://arxiv.org/abs/2407.04457>.
- Nihad Abuawwad, Manuel dos Santos Dias, Hazem Abusara, and Samir Lounis. Electrical engineering of topological magnetism in two-dimensional heterobilayers. *npj Spintronics* 2, 10 (2024). <https://doi.org/10.1038/s44306-024-00015-6>.
- Nihad Abuawwad, Manuel dos Santos Dias, Hazem Abusara, and Samir Lounis. *Phys. Rev. B*, 108, 094409 (2023). <https://link.aps.org/doi/10.1103/PhysRevB.108.094409>.
- Nihad Abuawwad, Manuel dos Santos Dias, Hazem Abusara, and Samir Lounis. *J. Phys.: Condens. Matter* 34 454001 (2022). <https://doi.org/10.1088/1361-648X/ac8f08>.

Publications previous to the thesis

- Nihad Abuawwad, Hazem Abusara, and Shakeb Ahmad. *Phys. Rev. C* 101, 064322 (2020). <https://link.aps.org/doi/10.1103/PhysRevC.101.064322>.

Conference contributions

1. Electrical engineering of topological magnetism in two-dimensional heterobilayers, **Nihad Abuawwad**, Manuel dos Santos Dias, Hazem Abusara, and Samir Lounis, **Talk**, ICM2024, Bologna, Italy, July 2024.
2. Electrical engineering of topological magnetism in two-dimensional heterobilayers, **Nihad Abuawwad**, Manuel dos Santos Dias, Hazem Abusara, and Samir Lounis, **Talk**, German Physical Society meeting (DPG2024), Berlin, Germany, March 2024.
3. Electrical engineering of topological magnetism in two-dimensional heterobilayers, **Nihad Abuawwad**, Manuel dos Santos Dias, Hazem Abusara, and Samir Lounis, **Talk**, SPP Skyrmionics, Young Researchers' Retreat, Dietmannsried, Germany, April 2024.
4. Electrical engineering of topological magnetism in two-dimensional heterobilayers, **Nihad Abuawwad**, Manuel dos Santos Dias, Hazem Abusara, and Samir Lounis, **Talk**, German Physical Society meeting (DPG2024), Berlin, Germany, March 2024.
5. Ab initio investigation of the magnetoelectricity of two-dimensional Van der Waals heterostructures, **Nihad Abuawwad**, Manuel dos Santos Dias, Hazem Abusara, and Samir Lounis, **Talk**, TMM Team-Prof. Hongbin Zhang, Darmstadt, Germany, January 2024.
6. Electrical engineering of topological magnetism in two-dimensional heterobilayers, **Nihad Abuawwad**, Manuel dos Santos Dias, Hazem Abusara, and Samir Lounis, **Talk**, SPP Skyrmionics, Retreat-Meeting SPP2137, Hamburg, Germany, September 2023.
7. CrTe₂ as a two-dimensional layer for topological magnetism in complex heterostructures, **Nihad Abuawwad**, Manuel dos Santos Dias, Hazem Abusara, and Samir Lounis, **Talk**, Psi-k: WE-Heraeus workshop, First-principles Green function formalisms: algorithms, method developments and applications to spinorbitronics and magneto-superconductivity, Athens, Greece, September 2023.
8. CrTe₂ as a two-dimensional layer for topological magnetism in complex heterostructures, **Nihad Abuawwad**, Manuel dos Santos Dias, Hazem Abusara, and Samir Lounis, **Poster**, Joint European Magnetic Symposia 2023 (JEMS2023), Madrid, Spain, August 2023.
9. CrTe₂ as a two-dimensional layer for topological magnetism in complex heterostructures, **Nihad Abuawwad**, Manuel dos Santos Dias, Hazem Abusara, and Samir Lounis, **Poster**, 3rd CENIDE conference, Bergisch Gladbach, Germany, May, 2023.

10. CrTe₂ as a two-dimensional layer for topological magnetism in complex heterostructures, **Nihad Abuawwad**, Manuel dos Santos Dias, Hazem Abusara, and Samir Lounis, **Poster**, meeting SPP 2244, Physikzentrum Bad Honnef, Germany, March, 2023.
11. CrTe₂ as a two-dimensional layer for topological magnetism in complex heterostructures, **Nihad Abuawwad**, Manuel dos Santos Dias, Hazem Abusara, and Samir Lounis, **Talk**, German Physical Society meeting (DPG2023), Dresden, Germany, March 2023.
12. Noncollinear magnetism in two-dimensional CrTe₂, **Nihad Abuawwad**, Manuel dos Santos Dias, Hazem Abusara, and Samir Lounis, **Poster**, meeting SPP 2244, Dresden, Germany, March, 2023.
13. Noncollinear magnetism in two-dimensional CrTe₂, **Nihad Abuawwad**, Manuel dos Santos Dias, Hazem Abusara, and Samir Lounis, **Talk**, German Physical Society meeting (DPG2022), Regensburg, Germany, September 2022.
14. Noncollinear magnetism in two-dimensional CrTe₂, **Nihad Abuawwad**, Manuel dos Santos Dias, Hazem Abusara, and Samir Lounis, **Poster**, Psi-K conference, Switzerland, August 2022.
15. Noncollinear magnetism in two-dimensional CrTe₂, **Nihad Abuawwad**, Manuel dos Santos Dias, Hazem Abusara, and Samir Lounis, **Talk**, Joint European Magnetic Symposia 2022 (JEMS2022), Warsaw, Poland, July 2022.
16. Charge density waves as enablers for chiral magnetism in two-dimensional CrTe₂, **Nihad Abuawwad**, Manuel dos Santos Dias, Hazem Abusara, and Samir Lounis, **Talk**, German Physical Society meeting (DPG2023), Online, Germany, September 2021.

List of Symbols

Symbols with Greek and Latin letters

- E - Energy
- F - Force
- Ψ - Wavefunction
- \mathbf{r}_i - Position vector of electrons
- \mathbf{R}_A - Position vector of nuclei
- T_e - Kinetic energy of electrons
- T_n - Kinetic energy of nuclei
- V_{n-n} - Repulsion between nuclei
- V_{e-e} - Electron-electron repulsion
- V_{e-n} - Attraction between electrons and nuclei
- V_{ext} - External potential
- E_{n-n} - Nuclear interaction term
- T_s - Kinetic energy of non-interacting particles
- E_H - Hartree energy
- E_{exc} - Exchange-correlation energy
- V_{eff} - Effective potential
- V_H - Hartree potential
- V_{exc} - Exchange-correlation potential
- R_{MT} - Muffin-tin radius
- R_{WS} - Wigner-Seitz radius
- R_{BS} - Bounding sphere radius
- Θ - Shape function
- Y_L - Real spherical harmonics
- C - Gaunt coefficient
- g - Free-electron gas Green function
- j_l - Spherical Bessel function
- h_l - Spherical Hankel function
- R_L - Regular solution
- S_L - Irregular solution
- ϵ_i - Single-particle energies
- ∇^2 - Laplacian operator
- ∇ - Nabla (gradient) operator
- ν_i - Volume of the Voronoi cell
- $n(r)$ - Charge density
- \mathbf{q} - Wavevector in spin spirals
- \mathbf{m} - Magnetization vector
- \mathbf{B} - External magnetic field
- γ - Gyromagnetic ratio
- \mathcal{J}_{ij} - Exchange interaction tensor
- \mathbf{D} - Dzyaloshinskii-Moriya vector
- ε - Levi-Civita symbol

Abbreviations

- DFT - Density Functional Theory
- KKR - Korringa-Kohn-Rostoker
- QE - Quantum ESPRESSO code
- PSLibrary - Pseudopotential Library
- SOC - Spin-Orbit Coupling
- LSDA - Local Spin Density Approximation
- GGA - Generalized Gradient Approximation
- PBE - Perdew, Burke, and Ernzerhof method
- NCPP - Norm-Conserving Pseudopotentials
- USPP - Ultrasoft Pseudopotentials
- LLG - Landau-Lifshitz-Gilbert equation
- GNEB - Geodesic Nudged Elastic Band method
- JuKKR-Jülich KKR code

Contents

Acknowledgments	i
Abstract	iii
Zusammenfassung	v
List of publications	vii
List of Symbols	xi
1. Introduction	1
2. Theory of magnetism	7
2.1. Magnetic interactions and classical ground state	7
2.1.1. Exchange interaction	7
2.1.2. Zeeman interaction	9
2.1.3. Magnetocrystalline Anisotropy	9
2.1.4. Dzyaloshinskii–Moriya Interaction(DMI)	10
2.2. Generalized Heisenberg Hamiltonian	11
2.3. Spin spirals in two-dimensional lattices	11
2.3.1. Some definitions	12
2.3.2. Case of a square lattice	13
2.3.3. Spin models on a general Bravais lattice	18
2.4. Topological magnetism: skyrmions and merons	20
2.4.1. Skyrmions	20
2.4.2. Merons and antimerons	23
3. Methods: Density Functional Theory	25
3.1. The many-body problem	25
3.2. Density functional theory: Overview	26
3.2.1. Kohn-Sham Formulation	27
3.2.2. DFT for spin-polarized systems	29
3.2.3. Approximations to the exchange-correlation energy functional	30
3.3. Plane wave basis and pseudopotentials method	30
3.3.1. Structural Optimization	31
3.3.2. Quantum ESPRESSO code	32
3.4. Korringa-Kohn-Rostoker (KKR) Green function method	33
3.4.1. General properties of the Green function	33

3.4.2. Voronoi construction in the full potential method	36
3.4.3. Free electron gas	38
3.4.4. Single site scattering	39
3.4.5. Multiple scattering theory	40
3.4.6. Finite-temperature complex contour integration	41
3.4.7. Relativistic corrections	42
3.4.8. KKR self-consistent cycle	42
3.4.9. KKR for extraction of the magnetic interactions	43
3.4.10. JuKKR code	46
4. Atomistic spin model and machine learning concepts	48
4.1. Atomistic spin model	49
4.1.1. Landau-Lifshitz-Gilbert equation	49
4.1.2. Geodesic Nudged Elastic Band (GNEB)	50
4.1.3. Spirit code	50
4.2. Linear Spin Wave Theory	50
4.2.1. Holstein-Primakoff Transformation	51
4.2.2. Bogoliubov Transformation	53
4.2.3. SpinW code	53
4.3. Machine learning techniques	53
4.3.1. Bayesian optimization	54
4.3.2. Trust region Bayesian optimization	56
4.3.3. Adversarial Bayesian optimization with Kalman filter (KFABO)	57
5. Magnetoelastic coupling in free-standing 2D CrTe₂ layer	59
5.1. Computational details	59
5.1.1. First-principles calculations	59
5.1.2. Magnetic interactions and atomistic spin relaxations	60
5.2. Geometric and magnetic properties	60
5.3. Magnetic interactions	61
5.4. Atomistic spin relaxation and magnetic ground states	65
5.5. Conclusions	66
6. CrTe₂ as a 2D material for topological magnetism in complex heterobilayers	69
6.1. Computational details	70
6.2. New topological AFM magnetic state in monolayer CrTe ₂	71
6.3. Various stacking orders in CrTe ₂ /XTe ₂ heterobilayers	73
6.4. Topological magnetic states in CrTe ₂ /XTe ₂ heterobilayers	74
6.5. Conclusions	77

7. Electrical engineering of topological magnetism in 2D heterobilayers	79
7.1. Computational details	80
7.2. Electric field modulation of the electronic properties in heterobilayers	81
7.3. Electric field control of magnetism in CrTe ₂ /XTe ₂ heterobilayers	83
7.4. Electric field control properties of topological states in CrTe ₂ /XTe ₂ heterobilayers	85
7.5. Conclusions	86
8. Active learning for spin waves probed by inelastic neutron scattering	88
8.1. Computational details	90
8.2. Algorithm benchmarking	91
8.3. Experimental spin wave spectrum fitting	93
8.4. Conclusion	96
9. Conclusions	98
A. Appendix (Chapter 2)	102
A.1. Spin models on a Bravais lattice	102
A.1.1. Exchange interactions	102
A.1.2. Dzyaloshinskii-Moriya interaction	103
A.1.3. Magnetic anisotropy	103
B. Appendix (Chapter 5)	105
B.1. Hubbard parameter U	105
C. Appendix (Chapter 6)	106
C.1. Electronic properties of the different stacking orders	106
C.2. Saddle points of the AFM merons, and FM skyrmions	106
D. Appendix (Chapter 7)	108
E. Appendix (Chapter 8)	111
E.1. Algorithm benchmarking with choosing specific q-path, and inclusion DMI	111
Bibliography	118

List of Figures

1-1. Various families of 2D materials and examples of their structures.	2
2-1. Illustration of different magnetic interactions.	9
2-2. Illustration of two different spiral states influenced by the direction of the DMI.	10
2-3. Schematic representation of spiral spin configurations with different cone angles θ	13
2-4. Spin configurations for a 2D square lattice and energy distribution profiles for different magnetic interactions	15
2-5. Illustration of an example of DMI vectors with C_{4v} symmetry	16
2-6. Cycloid state including DMI.	18
2-7. Two examples of skyrmionic textures due to different types of DMI.	21
2-8. Spin-textures of merons and antimerons with the projection onto the surface of a unit sphere.	23
3-1. Illustration of the Voronoi construction for a hexagonal unit cell.	37
3-2. Flowchart outlines the steps involved in the KKR self-consistent cycle.	43
4-1. Minimum energy path of metastable state's collapse.	51
4-2. The KFABO workflow.	58
5-1. Crystal structures of CrTe_2 monolayer for different assumed magnetic states.	62
5-2. Energetics of magnetic states for the different crystal structures of a CrTe_2 monolayer based on the computed exchange interactions.	64
5-3. Dzyaloshinskii-Moriya interactions in CrTe_2	66
5-4. Spiral states in different structures of a CrTe_2 monolayer.	67
6-1. Overview of the heterostructures and magnetic states.	70
6-2. Magnetic state in the free standing CrTe_2	72
6-3. The different AA, AA', AB, and AB' stacking arrangements for $\text{CrTe}_2/\text{XTe}_2$ heterobilayers.	73
6-4. Topological magnetic textures in heterobilayers.	76
6-5. Single skyrmion in $\text{CrTe}_2/(\text{Zr, Ni, Rh})\text{Te}_2$ heterobilayers.	77
7-1. Overview of the magnetic topological states with and without an electric field in heterobilayers.	80
7-2. Impact of the perpendicular electric field on the interlayer distances.	81
7-3. Magnetic interactions as a function of the distance for the heterobilayers.	83
7-4. Topological magnetic textures in heterobilayers.	85

8-1. Illustration of bulk CrSBr crystal structure.	90
8-2. Magnon spectrum for CrSBr with only J -values along three q-paths ($(1, k, 0)$, $(h, 2, 0)$, and $(h - 1, h + 1, 0)$).	91
8-3. Experimental magnon spectrum for CrSBr along three q-paths ($(1, k, 0)$, $(h, 2, 0)$, and $(h - 1, h + 1, 0)$).	95
9-1. Potential technological device concept combining 2D CrTe ₂ with other 2D layers, such as (Ta, Nb, Ti)Te ₂	99
9-2. Technological device concepts combining 2D CrTe ₂ with RhTe ₂	100
B-1. Magnetic state in bulk CrTe ₂	105
C-1. Electronic properties of the different stacking orders.	106
C-2. The spin-texture associated with the saddle point.	107
D-1. Charge accumulation with respect to the perpendicular (both positive and negative) electric field.	108
D-2. Selected orbital contributions to the local density of states.	109
D-3. Energetics of magnetic states for the heterobilayers based on the computed exchange interactions.	110
E-1. The pixel-by-pixel absolute differences plot of of bulk CrSBr between the spin wave with and without the interlayer AFM coupling (0.21 meV) for three different wavevector paths: $(1, k, 0)$, $(h, 2, 0)$, and $(h - 1, h + 1, 0)$	111
E-2. Magnon spectrum for CrSBr with only J -values for specific q-paths	113
E-3. Magnon spectrum for CrSBr with including the DMI along three q-paths ($(1, k, 0)$, $(h, 2, 0)$, and $(h - 1, h + 1, 0)$).	114
E-4. Illustration of magnetic properties of bulk CrSBr.	116
E-5. Magnon spectrum fitting in La ₂ CuO ₄ if we have portion information around the high symmetry point M.	117

List of Tables

5-1. Lattice parameters, bond lengths, and spin moments of the different CrTe ₂ monolayer structures hosting various FM and AFM phases.	61
5-2. The Heisenberg exchange coupling (J), the magnitude of the Dzyaloshinskii-Moriya vector ($ \mathbf{D} $), and magnetic anisotropy energy (K) for the different structures and magnetic phases of the CrTe ₂ monolayer.	63
5-3. Combined magnetic energy lowering for each of the considered crystal structures.	67
6-1. Total energy difference between various stacking orders and the ground state AA structure for all CrTe ₂ /XTe ₂ heterobilayers. Energies in meV.	74
6-2. Lattice constant a , interlayer distance h in the AA stacking. As a reference, the free-standing CrTe ₂ has a lattice constant of 3.71 Å.	74
6-3. Magnetic anisotropy energies (K) and Dzyaloshinskii-Moriya interaction (D) of the CrTe ₂ /XTe ₂ heterobilayers in the AA stacking.	75
6-4. Effect of the magnetic field on the topological charge of the AFM multi-meronic spin-texture.	77
8-1. Comparison between the KFABO fitted and target Heisenberg exchange interactions up to eight nearest neighbors.	94
8-2. Comparison between the KFABO fitted and Ab-initio Heisenberg exchange interactions up to eight nearest neighbors.	97
D-1. Energy differences in meV of various stacking with respect to AA for TiTe ₂ and RhTe ₂ under positive/negative electric field.	108
E-1. Comparison between the KFABO fitted and target Heisenberg exchange interactions up to eight nearest neighbors.	112
E-2. Comparison of KFABO fitted parameters versus target parameters using only one $(1, k, 0)$ path and two paths $(1, k, 0)$ with $(h, 2, 0)$	115

1. Introduction

In 2010, Kostya Novoselov and Andre Geim were granted the Nobel Prize in Physics for the discovery of graphene [1], a single layer of graphite. That was a turning point in the history of modern nanotechnology that opened the door for a new and unique field of two-dimensional (2D) materials. In recent years, lots of research has been conducted to prepare 2D materials beyond graphene. Geometrically, 2D materials are quantum-confined in one dimension, setting them apart from traditional materials. While conventional materials have strong intralayer covalent bonds, 2D materials are characterized by weak van der Waals (vdW) forces between layers. This atomic thinness in 2D materials leads to exceptional properties, including high transparency, a large surface-to-volume ratio, high flexibility, remarkable carrier mobility, outstanding electrical conductivity, broadband optical absorption, strong light-matter interactions, excellent heat extraction, and low inter-diffusion [2–6]. Moreover, a diverse range of 2D materials has been predicted and discovered, exhibiting energy bandgaps from semiconductors (e.g., transition metal dichalcogenides (TMDs)) to insulators (e.g., hexagonal boron nitride (hBN) and HfS_2) as shown in Figure. 1-1. The most significant discovery is that when 2D materials are stacked in blocks called heterostructures, their properties change, resulting in materials with novel hybrid characteristics. This makes them highly promising for next-generation nanoelectronics, as they enable the creation of high-performance structures tailored for specific applications. A notable aspect of these heterostructures is that the layers interact via very weak van der Waals forces. Due to this weak interlayer coupling, layers can be easily combined and separated, allowing for flexible assembly and reconfiguration of the materials.

These properties make 2D materials and their heterostructures promising candidates for a variety of functional devices across fields such as electronics, optoelectronics, energy storage, and spintronics. For example, semiconducting TMDCs are used to fabricate Field-Effect Transistors (FETs) by offering enhanced performance and novel design possibilities. These materials, such as SnSe_2 , WSe_2 , and SnSe , exhibit unique electronic properties ideal for FET applications, including atomically thin structures, and high carrier mobility [7,8]. Also, topological insulators (TIs) made from transition metal dichalcogenides find applications in Magnetic Random-Access Memories (MRAMs) through various mechanisms such as giant spin-orbit torque (SOT) offering an energy-efficient writing method for magnetic memory, potentially leading to SOT-based MRAMs [9]. Additionally, the integration of 2D materials like graphene, TMDCs, and the family of transition metal carbides, carbonitrides and nitrides (MXenes), has shown great promise in enhancing the performance of optoelectronic devices such as photodetectors, Light Emitting diodes (LEDs), and photovoltaics [10].

One interesting aspect related to 2D materials and their heterostructures is their magnetism. Back in 1966, Mermin and Wagner proved that 2D systems with continuous symmetry cannot be magnetically ordered at finite temperature [11]. This makes magnetic order in 2D

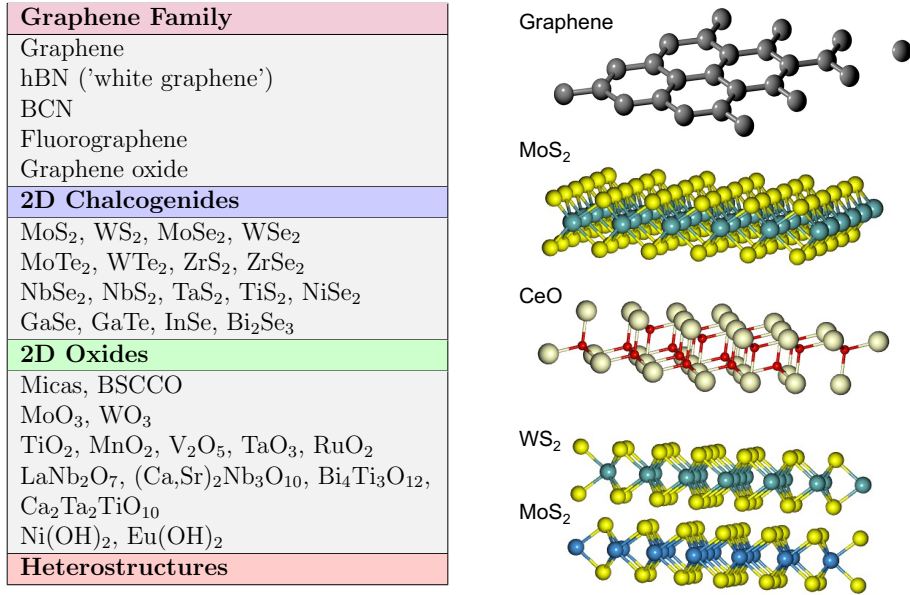


Figure 1-1.: Various families of 2D materials and examples of their structures that inspired by [2].

reliant on interactions that breaks the spin-rotational invariance, for instance, an external magnetic field or the magnetocrystalline anisotropy, which are typically much weaker than exchange interactions and so might lead to very low ordering temperatures. It was thus very surprising that 2D magnets were discovered experimentally in 2017 in CrI₃ [12] and Cr₂Ge₂Te₆ [13] down to the mono- and bilayer limit, respectively. Afterwards, intense research activities were made to expand the development of 2D magnets [14–18]. The possibility of heterostructuring offers the unprecedented possibility to engineer quantum materials with exquisite properties facilitated by the quasi-perfect interfaces expected by the van der Waals (vdW) gaps. This enables the realization of totally new heterostructures hosting novel functionalities that are not otherwise seen in the individual building blocks. In most cases, these 2D materials have a simple collinear magnetic order, such as Ferromagnetic (FM), or Antiferromagnetic (AFM). However, they can also exhibit complex noncollinear magnetism and host ferromagnetic skyrmions, to give just two examples. Skyrmions are topologically-protected chiral spin textures of great interest for potential applications as information carriers in information technology devices [19, 20]. These chiral magnetic states typically arise due to the interplay between Heisenberg exchange and relativistic Dzyaloshinskii-Moriya interaction (DMI) [21, 22] in materials that lack inversion symmetry and have non-zero spin-orbit coupling. In a 2D material, skyrmions are solitonic magnetic objects that arise within

a magnetization background pointing out of the plane of the magnetic layer. When the background magnetization is in-plane, merons can emerge, which represent another form of chiral spin-textures. The topological charge for skyrmions is integer, while it is half-integer for merons, hence both kinds of spin textures are qualitatively distinct [23–25]. These topological defects are discussed in the next chapter.

In the context of 2D heterostructures, FM skyrmions have been experimentally observed in Fe_3GeTe_2 [26–30], and their theoretical existence has been proposed in many systems like MnXTe ($X = \text{S}$ and Se) [31], CrInX_3 ($X = \text{Te}, \text{Se}$) [32], bilayer Bi_2Se_3 - EuS [33]. However, FM merons remain undetected in 2D van der Waals (vdW) heterostructures, with their identification limited to more conventional thin films and disks [34–36]. Theoretically, a free standing monolayer of CrCl_3 has been predicted to host such half-integer spin-textures, which are stabilized by the magnetic dipolar coupling that favors an overall in-plane orientation of the magnetization [37]. CrTe_2 is a new entrant in the field of 2D magnets, although it has been known for a few years in the bulk form [38] and has been simulated in the monolayer form [39]. Recently, magnetic circular dichroism experiments demonstrated that thin CrTe_2 grown either on SiO_2/Si or bilayer graphene substrates are FM with a Curie temperature of 200 K [40, 41]. This Curie temperature is high when compared to other 2D magnetic materials such as CrI_3 , which as a single monolayer has a Curie temperature of 45 K. In contrast to the previous finding, a monolayer of CrTe_2 deposited on graphene was found to host a zig-zag AFM state as revealed by spin-polarised scanning tunnelling microscopy (SP-STM) combined with first-principles calculations, with an applied magnetic field driving the monolayer into a noncollinear spin texture [42]. Interestingly, when simulating a free standing CrTe_2 by density functional theory (DFT), a charge density wave (CDW) phase has been found after observing a clear instability in the phonon band structure [43]. Further theoretical studies unveiled the strong dependence of the magnetic ground states of 1T- CrTe_2 on the film thickness: an intralayer and interlayer AFM-FM transition occurs at a critical thickness of five CrTe_2 layers, which represents the bulk magnetic state [44]. Moreover, DFT calculations for a monolayer of CrTe_2 show an AFM metallic behavior in 1T phase, and FM semiconductor in a deformed phase of 1T called 1T' phase [45].

In this study, utilizing a multi-pronged approach based on first-principles calculations combined with an ab-initio parameterized Heisenberg model, we found a strong coupling between magnetism and crystal structure in a single layer of CrTe_2 , whose magnetic states are subsequently explored via atomistic spin dynamics. Also, we investigated the possibility of engineering 2D topological magnetism in a CrTe_2 monolayer by constructing heterostructures with Te-based layers involving other non-magnetic transition metal atoms. We unveiled new topological AFM objects already arising in the free-standing 1T phase of CrTe_2 . These objects consist of multi-meronic particles emerging in a frustrated in-plane Néel magnetic environment. Such AFM topological states have long been sought in the context of skyrmionics as ideal information carriers since they are expected to be unaffected by the skyrmion Hall effect [20, 46–50] responsible for the undesired deflection of conventional skyrmions from a

straight trajectory upon application of a current. Their AFM nature should also lead to a weak sensitivity to external magnetic fields and potentially terahertz dynamics [51, 52], further motivating efforts towards their experimental realization. Once interfaced with various Te-based layers containing either heavy or light transition metal atoms, we demonstrate the ability to engineer the stability and nature of the underlying magnetic state. Surprisingly, with the right vdW heterostructure, the AFM merons can be converted to FM skyrmions, which opens unique opportunities for designing devices made of 2D materials to realize fundamental concepts for information technology based on topological magnetic bits.

Moreover, we uncover the non-trivial impact of the electric field on noncollinear magnetic structures in CrTe₂/(Rh, Ti) Te₂ heterobilayers. For the CrTe₂/RhTe₂ bilayer, we discover all-electrical switching between two topologically different magnetic structures, FM skyrmions and FM meron pairs. The perpendicular electric field has a strong influence on the interlayer spacing between the 2D materials, which modifies several key magnetic interactions: the Heisenberg exchange interaction, the DMI and the MA. These electric-field-induced alterations enable the transition of skyrmions into meron structures and vice-versa. A very different scenario arises when interfacing CrTe₂ with TiTe₂, which leads to the emergence of frustrated AFM merons whose stability and size can be tuned by the applied electric field. Our findings provide the foundation for further exploration in electrically tunable magnetic systems, offering innovative avenues for the design and control of novel spintronic functionalities.

Finally, we shift our focus to another two-dimensional material, CrSBr, known for its unique magnetic and optoelectronic properties [53–56]. In its bulk form, it exhibits magnetic ordering at a Néel temperature (T_N) of 132 K [57–59], with A-type antiferromagnetism characterized by ferromagnetic planes with a magnetization aligned along the b -axis, which alternate direction, resulting in an overall AFM configuration. Moreover, CrSBr stands out for its strong spin-orbit coupling which imposes an in-plane magnetization. Other spin-orbit driven interactions such as the DMI can be significant in this material, which can lead to rich topological magnetic phases, enabling the design of specific magnonic band structures and optimizing the propagation and interaction of magnons for desired applications.

Spin waves, or magnons, are fundamental excitations in magnetic materials, providing insights into their dynamic properties and interactions. Spin-excitation spectra are typically derived by measuring the dynamical structure factor through inelastic neutron or x-ray scattering techniques. These spectra are then analyzed by comparing the experimental outcomes with theoretical predictions, where experiment planning, data processing, and analysis are time-consuming. In this study, by taking the CrSBr magnon spectrum as an example, we introduce a machine learning platform that integrates active learning sampling with Linear Spin Wave Theory (LSWT), leading to a Kalman Filter Adversarial Bayesian Optimization (KFABO) algorithm capable of tackling significantly noisy experimental spectra. The objective of this algorithm is to map the experimentally extracted magnon spectrum using the minimum number of sampling points and iterations. The ABO algorithm is designed

to accurately extract magnetic parameters from inelastic neutron scattering data, thereby substantially improving the efficiency and accuracy of experimental measurements in complex systems where unveiling hidden and weak magnetic interactions not accessible with conventional fitting procedures.

The thesis is organized as follows:

- **Chapter 2:** This chapter discusses some fundamental concepts for magnetic interactions, including Heisenberg exchange, DMI, magnetic anisotropy, and Zeeman interactions, which contribute to the Heisenberg Hamiltonian utilized in this thesis. Additionally, we explain how these interactions lead to non-collinear states, such as spiral states. Finally, the chapter introduces the topological magnetic states discussed in this thesis (skyrmions, merons).
- **Chapter 3:** This chapter provides an introduction to DFT and its fundamental concepts. We then present one theoretical DFT-based framework utilized in the thesis. We start with plane waves [60] and pseudopotentials [61, 62], as implemented in the Quantum Espresso software [63–65]. Next, we shift our focus to a second variant of the DFT-based methodology used in the thesis, which consists of the Korringa-Kohn-Rostoker (KKR) Green function method [66, 67]. We emphasize the underlying principles based on multiple scattering theory and implemented in the Jülich KKR (JuKKR) family of codes [68–71]. We introduce the multiscale modelling approach utilized in the thesis which is based on mapping from ab-initio the magnetic interactions of a Heisenberg Hamiltonian.
- **Chapter 4:** This chapter delves into the description of the theoretical framework utilized in exploring the atomic spin dynamics properties as implemented in the Jülich Spirit software [72, 73]. This tool enables us to identify ground state properties within an extended Heisenberg model, with parameters extracted from first-principles simulations. The chapter also introduces a machine learning algorithm that integrates active learning sampling with linear spin wave theory leading to an efficient KFABO algorithm to address complex and noisy neutron scattering data measuring magnon spectra.
- **Chapter 5:** This chapter presents multi-scale simulations of the diverse behavior of the monolayer of CrTe₂ by demonstrating a strong coupling between magnetism and the crystal structure.
- **Chapter 6:** In this chapter, we explore the interfacing of a CrTe₂ layer with various tellurium-based (Te-based) layers, which enables the manipulation of key magnetic properties, such as the isotropic magnetic exchange interactions, Dzyaloshinskii-Moriya interactions, and the magnetic anisotropy energy. We predict the formation of topological magnetic phases, including skyrmions and antiferromagnetic Néel merons.

- **Chapter 7:** Here, we investigate the impact of an external electric field on topological magnetism in 2D heterostructures. Our first-principles analysis reveals that applying an external electric field can effectively modify the vdW spacing between CrTe₂ and (Rh, Ti)Te₂ layers, consequently influencing the fundamental magnetic interactions. This adjustment allows for the transition between ferromagnetic skyrmions and meron pairs in the CrTe₂/RhTe₂ heterobilayer system. Simultaneously, it significantly enhances the stability of antiferromagnetic merons that are characteristically frustrated, in the CrTe₂/TiTe₂ heterobilayer.
- **Chapter 8:** In this chapter, we applied our machine learning algorithm to the 2D CrSBr material. The algorithm successfully recovers the shape of the theoretical and experimental spin wave spectra. It also achieves a good fit for the magnetic parameters, including the Heisenberg exchange parameter and Dzyaloshinskii-Moriya Interaction [74]. Additionally, the algorithm was applied to noisy experimental magnon spectra with various resolutions, demonstrating its robustness and accuracy. From the experimental data, we could recover a significant AFM interlayer coupling responsible for the large Néel temperature of CrSBr, which could not be extracted by regular fitting and is in accordance with our ab-initio simulations.
- **Chapter 9:** This chapter concludes the thesis. We summarize the thesis and provide a short outlook on future exciting research directions.

2. Theory of magnetism

Magnetic materials play a crucial role in our society, with numerous applications including data storage devices, energy generation, and medical therapies. Magnetism is intrinsically quantum mechanical in nature, and magnetic ordering can only be explained by the use of quantum theory. At the atomic level, magnetism arises mainly from two sources: the spin of the electrons and the orbital motion of electrons around the nucleus. Each electron possesses an intrinsic property known as spin, which generates a magnetic moment. The magnetic moment associated with an electron's spin is a quantum mechanical property, meaning it can have discrete orientations, typically referred to as "spin-up" and "spin-down." When many spins align in the same direction, their individual magnetic moments combine to produce a net magnetic moment, leading to ferromagnetism, as seen in materials like iron, cobalt, and nickel. The magnetic properties of a material depend on the interactions between individual magnetic moments. This chapter establishes some key concepts on magnetic interactions and the ground state, offering a detailed analysis of these interactions in reciprocal space and exploring spin models on a general Bravais lattice. It also covers advanced topics in topological magnetism, including skyrmions and merons.

2.1. Magnetic interactions and classical ground state

In this section, we explore various types of magnetic interactions that can lead to the emergence of magnetic long-range order. We begin by discussing the bilinear Heisenberg exchange interaction, which is the fundamental mechanism behind magnetic ordering in many materials. Additionally, we examine other types of magnetic interactions, such as Dzyaloshinskii–Moriya Interaction (DMI) and magnetocrystalline anisotropy, and discuss their role in stabilizing different magnetic ground states.

2.1.1. Exchange interaction

The exchange interaction in magnetic materials originates from the fundamental principles of electrostatics and quantum mechanics, particularly the Coulomb interaction between electrons and the Pauli exclusion principle [75, 76]. To understand the origin of the exchange interaction, consider a hydrogen molecule (H_2) where the Hamiltonian for two hydrogen nuclei (A and B) and two electrons (1 and 2) is given by:

$$\mathcal{H} = \mathcal{H}_0(\mathbf{r}_1 - \mathbf{R}_A) + \mathcal{H}_0(\mathbf{r}_2 - \mathbf{R}_B) + \mathcal{H}_{\text{int}}, \quad (2-1)$$

where \mathcal{H}_0 represents the one-electron Hamiltonian:

$$\mathcal{H}_0 = \frac{p^2}{2m_e} + U(\mathbf{r}), \quad (2-2)$$

where m_e is the mass of electron and \mathcal{H}_{int} is the Coulomb interaction between the electrons:

$$\mathcal{H}_{\text{int}} = \frac{e^2}{|\mathbf{r}_1 - \mathbf{r}_2|}. \quad (2-3)$$

The wave function of the two-electron system is:

$$\Psi(1, 2) = \psi(\mathbf{r}_1, \mathbf{r}_2)\chi(\sigma_1, \sigma_2), \quad (2-4)$$

where $\psi(\mathbf{r}_1, \mathbf{r}_2)$ is the spatial (orbital) part and $\chi(\sigma_1, \sigma_2)$ is the spin part.

According to the Pauli exclusion principle, the total wave function must be antisymmetric $\Psi(1, 2) = -\Psi(2, 1)$. This antisymmetry requirement can be satisfied in two ways: First, the singlet state ($S = 0$) where $\chi(\sigma_1, \sigma_2)$ is antisymmetric and $\psi(r_1, r_2)$ is symmetric. Second, the triplet state ($S = 1$) where $\chi(\sigma_1, \sigma_2)$ is symmetric and $\psi(r_1, r_2)$ is antisymmetric. The energy difference between these states arises from the spatial part of the wave function interacting with the Coulomb potential \mathcal{H}_{int} :

$$\Delta E = E_{\text{triplet}} - E_{\text{singlet}} = -J_{12}(\mathbf{S}_1 \cdot \mathbf{S}_2), \quad (2-5)$$

where \mathbf{S}_1 and \mathbf{S}_2 are the spin vectors, and J_{12} represents the exchange integral:

$$J_{12} \propto \int \psi_1^*(\mathbf{r}_1)\psi_2^*(\mathbf{r}_2) \frac{e^2}{|\mathbf{r}_1 - \mathbf{r}_2|} \psi_1(\mathbf{r}_2)\psi_2(\mathbf{r}_1) dr_1 dr_2. \quad (2-6)$$

The Heisenberg model can then be postulated as the generalization of the above developments for N interacting spins:

$$\mathcal{H}_{\text{Exc}} = - \sum_{i,j} J_{ij} \mathbf{S}_i \cdot \mathbf{S}_j, \quad (2-7)$$

where J_{ij} represents the exchange integral between spins at sites i and j , and \mathbf{S}_i and \mathbf{S}_j are the unit direction of the magnetic moment at these sites:

$$\mathbf{S}_i = (\cos(\phi) \sin(\theta), \sin(\phi) \sin(\theta), \cos(\theta)). \quad (2-8)$$

The sign and magnitude of J_{ij} determine the type of magnetic ordering. This interaction is responsible for the alignment of magnetic moments or spins in a material, leading to various types of magnetic order such as ferromagnetism (FM) ($J_{ij} > 0$) and antiferromagnetism (AFM) ($J_{ij} < 0$). In special cases, where spins interact antiferromagnetically with their nearest and next-nearest neighbors, magnetic competition among interactions arises, leading to magnetic frustration, and preventing all the spins from being in a collinear magnetic state. The system 'frustrates' in an attempt to find a compromise that can lower the overall energy in a non-collinear magnetic state. This can result in complex spin textures like spiral orders

or even disordered magnetic states.

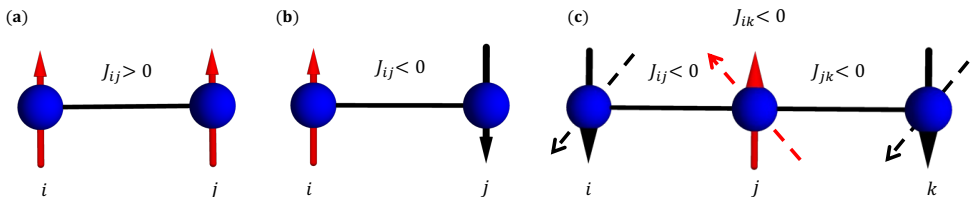


Figure 2-1.: **Illustration of different magnetic interactions.** (a) Ferromagnetic (FM) where $J_{ij} > 0$ leading to parallel spin alignment. (b) Antiferromagnetic (AFM) with $J_{ij} < 0$ resulting in antiparallel alignment. (c) Frustrated exchange interactions with for example AFM interactions between nearest and next-nearest neighbors.

2.1.2. Zeeman interaction

Zeeman interaction often referred to as the Zeeman effect [77, 78], describes the influence of an external magnetic field on the energy levels of a quantum system with magnetic moments. The Hamiltonian for the Zeeman interaction can be expressed as:

$$\mathcal{H}_{\text{Zeeman}} = - \sum_i \mathbf{S}_i \cdot m_i \mathbf{B}, \quad (2-9)$$

where \mathbf{B} denotes the external magnetic field, and m_i spin magnetic moment.

2.1.3. Magnetocrystalline Anisotropy

Magnetic anisotropy energy can arise from various origins. In this context, we will focus exclusively on magnetocrystalline anisotropy, disregarding shape anisotropy, which is a macroscopic effect due to dipole-dipole interactions. In the context of 2D materials explored in the thesis, the shape anisotropy favors an in-plane orientation of the magnetic moments. Magnetocrystalline anisotropy stems from spin-orbit coupling and directly reflects the crystal lattice symmetries in the energy profile as a function of the magnetic moment's orientation. For simplicity, we will consider the system exhibits uniaxial anisotropy. In this simple case, the corresponding spin Hamiltonian for this interaction is expressed as:

$$\mathcal{H}_{\text{Anisotropy}} = - \sum_i K_i (S_i^\alpha)^2, \quad (2-10)$$

where α is a unit vector along the preferred direction (eg. x, y, z), and K represents the magnetic anisotropy energy (MAE) parameter. If $K > 0$, the system possesses an easy axis, which minimizes energy when the magnetic moments align parallel to α . Conversely,

a negative K implies an easy plane, where the energy is minimized when the magnetic moments are perpendicular to α .

2.1.4. Dzyaloshinskii–Moriya Interaction(DMI)

Dzyaloshinskii–Moriya Interaction (DMI) is a type of antisymmetric exchange interaction (See Eq. 2-11) that arises in systems with broken inversion symmetry and strong spin-orbit coupling [21, 22].

$$\mathcal{H}_{\text{DMI}} = - \sum_{i,j} \mathbf{D}_{ij} \cdot (\mathbf{S}_i \times \mathbf{S}_j) . \quad (2-11)$$

DMI plays a crucial role in breaking inversion symmetry leading to the stabilization of a specific chiral magnetic structure like spin spirals and skyrmions. The orientation of the \mathbf{D}_{ij} influences the chirality of spin spiral states, determining whether the spin rotates clockwise (left-handed spiral state) or anti-clockwise (right-handed spiral state). When the DMI vector (\mathbf{D}_{ij}) is oriented out of the plane of rotation of the moments it leads to a left-handed spiral state as shown in Figure. 2-2 (a). Conversely, as shown in the figure. 2-2 (b), the DMI vector pointing in the opposite direction results in a right-handed spiral state. Moriya’s symmetry rules provide a specific symmetry element (like mirrors or rotation axes) to determine the direction and the strength of the DMI vector based on the crystal symmetry and the arrangement of magnetic ions [21].

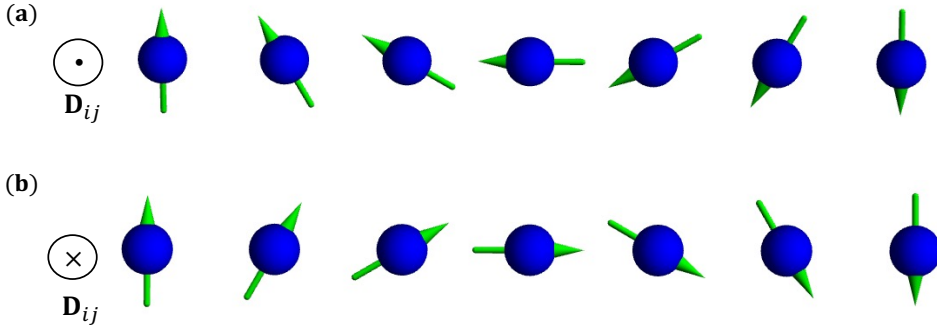
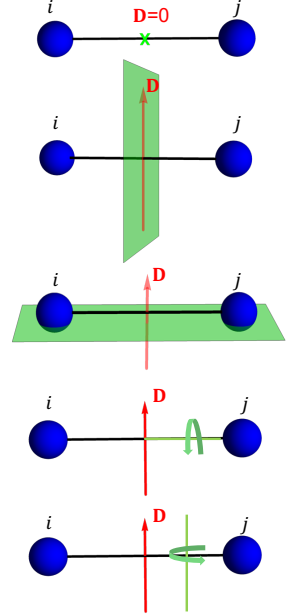


Figure 2-2.: Illustration of two different spiral states influenced by the direction of the DMI. (a) A left-handed spiral state occurs when the DMI vector \mathbf{D}_{ij} is oriented out of the plane. (b) A right-handed spiral state forms when the DMI vector \mathbf{D}_{ij} is oriented in the opposite direction.

- **Centrosymmetric sites:** No DMI exists if the midpoint between two interacting magnetic ions possesses inversion symmetry.
- **Mirror planes:** If the line connecting two magnetic ions lies in a mirror plane, then the DMI vector is perpendicular to this plane.
- **Mirror planes (bisecting):** If a mirror plane bisects the line connecting two magnetic ions, then the DMI vector lies within this plane and is perpendicular to the connecting line.
- **Two-fold rotation axes:** If a two-fold rotation axis lies along the line connecting two magnetic ions, then the DMI vector is perpendicular to this axis.
- **Two-fold rotation axes (bisecting):** If a two-fold rotation axis bisects the line connecting two magnetic ions, the DMI vector lies along this axis.



2.2. Generalized Heisenberg Hamiltonian

We can finally incorporate all the magnetic interactions discussed thus far into the following generalized Heisenberg Hamiltonian:

Heisenberg Hamiltonian

$$\mathcal{H} = - \underbrace{\sum_i \mathbf{B} \cdot \mathbf{S}_i}_{\text{Zeeman energy}} - \underbrace{\sum_i K_i (S_i^\alpha)^2}_{\text{Anisotropy energy}} - \underbrace{\sum_{i,j} J_{ij} \mathbf{S}_i \cdot \mathbf{S}_j}_{\text{Exchange energy}} - \underbrace{\sum_{i,j} \mathbf{D}_{ij} \cdot (\mathbf{S}_i \times \mathbf{S}_j)}_{\text{Dzyaloshinskii-Moriya energy}} \quad (2-12)$$

The last two parameters J_{ij} and \mathbf{D}_{ij} are calculated by the method of the infinitesimal rotation where the Heisenberg Hamiltonian is written in matrix representation as shown in Sec. 3.4.9.

2.3. Spin spirals in two-dimensional lattices

After introducing the magnetic interactions relevant to the study presented in the thesis, we discuss in this section spin spirals and their energetics for a general two-dimensional bravais lattice, by taking the example of a simple case of a square lattice. As will be shown in the results chapters, in the investigated 2D vdW heterostructures there can be rather complex

spiraling states forming, which can be either ferromagnetic or antiferromagnetic in nature. It is thus educational to introduce how such states form in a simple model. We will analyze the possible energy minima characterizing such a lattice in two steps. First considering the impact of Heisenberg exchange interactions, limited to the second nearest neighboring interactions. Second by exploring the impact of the nearest neighboring DMI.

2.3.1. Some definitions

We consider two-dimensional systems. The points of a Bravais lattice are specified by integer combinations of two primitive vectors,

$$\mathbf{R}_n = n_1 \mathbf{a}_1 + n_2 \mathbf{a}_2 . \quad (2-13)$$

The reciprocal lattice is generated in a similar way using the primitive vectors that satisfy the conditions

$$\mathbf{b}_i \cdot \mathbf{a}_j = 2\pi \delta_{ij} . \quad (2-14)$$

A function with values on the direct lattice can be given in terms of its Fourier coefficients

$$f(\mathbf{R}_n) = f_n = \sum_{\mathbf{q}} e^{i\mathbf{q} \cdot \mathbf{R}_n} f(\mathbf{q}) , \quad f(\mathbf{q}) = \frac{1}{N} \sum_n e^{-i\mathbf{q} \cdot \mathbf{R}_n} f_n , \quad (2-15)$$

with the sum over all the wave vectors in the first Brillouin zone of the reciprocal lattice. N is the total number of lattice points in the direct lattice and is crucial for normalizing the transformation between the direct and reciprocal lattice representations of the function. The wave vector can be expressed as

$$\mathbf{q} = q_1 \mathbf{b}_1 + q_2 \mathbf{b}_2 . \quad (2-16)$$

Since

$$\mathbf{q} \cdot \mathbf{R}_n = 2\pi (q_1 n_1 + q_2 n_2) , \quad (2-17)$$

then

$$\sum_{\mathbf{q}} e^{i\mathbf{q} \cdot \mathbf{R}_n} = N \delta_{n,0} , \quad \sum_n e^{i\mathbf{q} \cdot \mathbf{R}_n} = N \delta_{\mathbf{q},0} . \quad (2-18)$$

In the study of spiral states, various configurations exist. For example: (i) helical spirals are characterized by spins rotating perpendicular to the propagation vector, (ii) cycloidal spirals, where spins rotate in a plane containing the propagation vector, and (iii) conical spirals, where spins form a cone along the propagation vector. Here we focus on the conical spirals, which are more general than the helical and cycloidal ones.

We consider the Hamiltonian \mathcal{H} in Eq. 2-12, the goal is to evaluate the energy of a family of magnetic states in a conical spiral given by:

$$\mathbf{S}_i = \sin \theta (\cos(\mathbf{q} \cdot \mathbf{R}_i) \mathbf{n}_1 + \sin(\mathbf{q} \cdot \mathbf{R}_i) \mathbf{n}_2) + \cos \theta \mathbf{n}_3 , \quad (2-19)$$

where the spins rotate on the surface of a cone around the direction $\mathbf{n}_3 = \mathbf{n}_1 \times \mathbf{n}_2$. Here θ is the cone angle and the rotation angle is given by $\mathbf{q} \cdot \mathbf{R}_i$. When $\theta = 0$, all spins align in direction of \mathbf{n}_3 , while spins rotate in plane perpendicular to \mathbf{n}_3 when $\theta = \pi/2$.

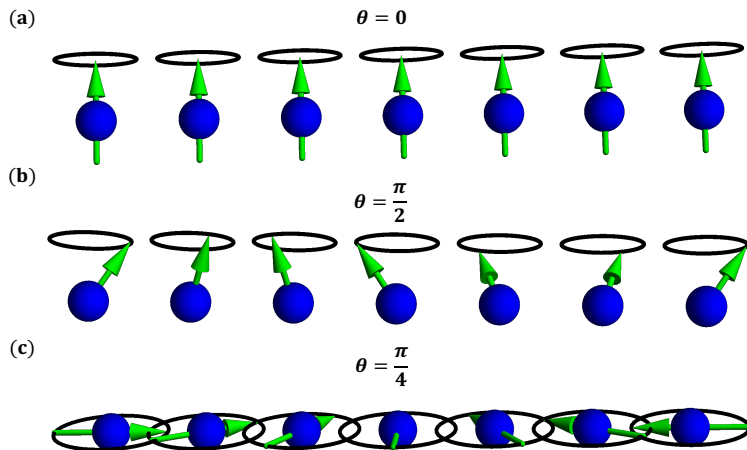


Figure 2-3.: Schematic representation of spiral spin configurations with different cone angles θ . (a) FM state when $\theta=0$. (b) $\theta = \pi/2$. (c) $\theta = \pi/4$.

2.3.2. Case of a square lattice

For simplicity, we first consider a square lattice with nearest- and next-nearest-neighbor interactions, and we discard the magnetic field, the DMI, and the magnetic anisotropy from Eq. (2-12). Let J_1 and J_2 be the value of J_{ij} for nearest-neighbors and next-nearest-neighbor interactions, respectively. In this system, the first Brillouin zone, is characterized by reciprocal lattice vectors q_1 and q_2 , so the contribution of the J_{ij} 's to the energy of the magnetic state is:

$$\mathcal{E}_J = -2J_1[\cos 2\pi q_1 + \cos 2\pi q_2] - 2J_2[\cos 2\pi(q_1 + q_2) + \cos 2\pi(q_1 - q_2)]. \quad (2-20)$$

By taking derivatives of \mathcal{E}_J in Eq. (2-20) with respect to q_1, q_2 we get:

$$\sin 2\pi q_1 \left(1 + \frac{2J_2}{J_1} \cos 2\pi q_2 \right) = 0, \quad (2-21)$$

$$\sin 2\pi q_2 \left(1 + \frac{2J_2}{J_1} \cos 2\pi q_1 \right) = 0. \quad (2-22)$$

The possible solutions for these two equations are $(0, 0)$, $(0, \pm\frac{1}{2})$, $(\pm\frac{1}{2}, 0)$, $(\pm\frac{1}{2}, \pm\frac{1}{2})$, $(\pm q^*, \pm q^*)$ with $q^* = \frac{1}{2\pi} \arccos\left(\frac{-J_1}{2J_2}\right)$. The latter points $(\pm\frac{1}{2}, \pm\frac{1}{2})$, $(\pm q^*, \pm q^*)$ are defined for $|J_1| < 2|J_2|$

but turn out to be saddle points, meaning that they cannot minimize the energy of the magnetic state.

With these results at hand, one can determine the minima depending on J_1 and J_2 . The four points $(\pm\frac{1}{2}, \pm\frac{1}{2})$ are equivalent because they are connected by a reciprocal lattice vector and so can be replaced by one point (e.g. $(\frac{1}{2}, \frac{1}{2})$). Also, for the same reason both points in the two pairs $(0, \pm\frac{1}{2}), (\pm\frac{1}{2}, 0)$ are equivalent and can be replaced by two points $(0, \frac{1}{2}), (\frac{1}{2}, 0)$, respectively. Thus, we have four possible critical points $(0, 0), (0, \frac{1}{2}), (\frac{1}{2}, 0), (\frac{1}{2}, \frac{1}{2})$ to consider in our energy analysis. Now, by symmetry $(0, \frac{1}{2}), (\frac{1}{2}, 0)$ represent the same type of critical point. Then, to find the local minima, we used Morse theory [79], which studies the manifold by examining the critical points of a smooth function defined on it:

$$n_{max} - n_{sp} + n_{min} = \xi(M). \quad (2-23)$$

$\xi(M)$ is the Euler characteristic of the manifold M , n_{max} represents the number of critical points that are local maxima, n_{sp} is the number of critical points that are saddle points, and n_{min} is the number of critical points that are local minima. In the specific case of a closed, compact surface without boundary, this relationship simplifies, and the sum should match the Euler characteristic, which can be zero for certain manifolds like tori. By applying the Morse theory to these points, where we know that there is one minimum at $(0, 0)$, and one maximum at $(\frac{1}{2}, \frac{1}{2})$, it follows that the points $(0, \frac{1}{2}), (\frac{1}{2}, 0)$ must be saddle points and not minima.

Consequently, there are two possibilities for the energy minimum depending on the sign of J_1 :

- If $|J_1| > 2|J_2|$ and
 - $J_1 > 0$, the energy minimum is at $(0, 0)$ which is the FM state shown in Fig. 2-4 (a).
 - $J_1 < 0$, the minimum is at $(\frac{1}{2}, \frac{1}{2})$, which is the AFM-1 state shown in Fig. 2-4 (b).
- If $|J_1| < 2|J_2|$ and
 - $J_2 > 0$, then we have maxima at $(0, \frac{1}{2}), (\frac{1}{2}, 0)$, while we have minima at $(0, 0), (\frac{1}{2}, \frac{1}{2})$, and the sign of J_1 determine the location of the global minimum ($J_1 > 0$, we have minima at $(0, 0)$ which is the FM state as in Fig. 2-4, while we have minima at $(\frac{1}{2}, \frac{1}{2})$ when $J_1 < 0$ which is the AFM-1 state shown in Fig. 2-4 (b)).
 - $J_2 < 0$, the energy minimum switches to $(0, \frac{1}{2}), (\frac{1}{2}, 0)$ which is the AFM-2 state illustrated in Fig. 2-4 (c).

After our energy analysis assuming the only presence of the Heisenberg exchange interactions, we extend our discussion to include the DMI. To specify the latter, which is a vector, we need to know something about the symmetry. We set $i = 0$ to be the origin and j some

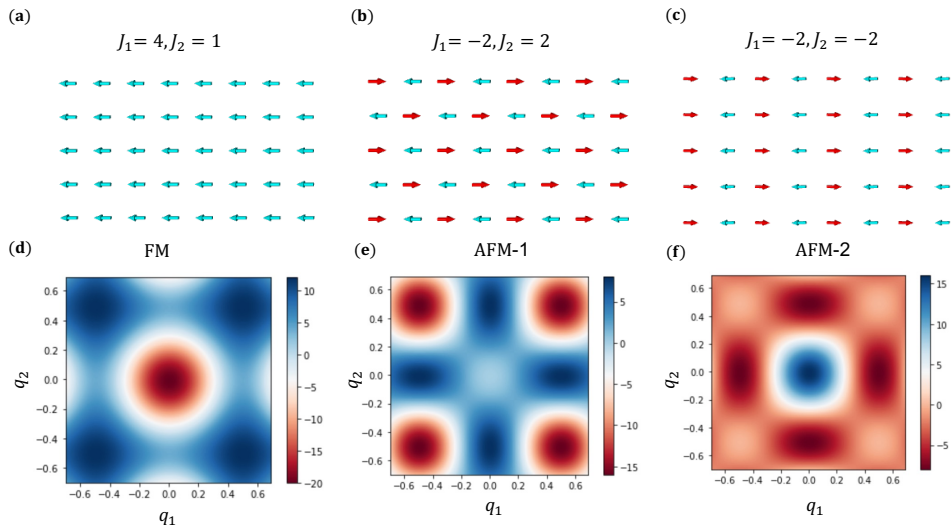


Figure 2-4.: **Spin configurations for a 2D square lattice and energy distribution profiles for different magnetic interactions.** (a) Ferromagnetic (FM) alignment with $J_1 = 4J_2 = 1$. (b) Antiferromagnetic (AFM-1) arrangement with $J_1 = -2J_2 = 2$. (c) Another antiferromagnetic (AFM-2) state with $J_1 = -2J_2 = -2$. (d-f) The \mathcal{E}_J as a function of reciprocal vectors q_1 , and q_2 for the FM, AFM-1, and AFM-2; respectively. The dark red color is the minimum and the dark blue is the maximum.

neighboring site, given by the coordinates (n_1, n_2) . Assuming C_{4v} symmetry, the DMI vectors are:

$$\mathbf{D}_{01} = D_1 (0, 1, 0) , \quad \mathbf{D}_{02} = D_1 (-1, 0, 0) , \quad \mathbf{D}_{03} = D_1 (0, -1, 0) , \quad \mathbf{D}_{04} = D_1 (1, 0, 0) , \quad (2-24)$$

where D_1 is the DMI interaction strength for the nearest neighbors: $j = 1$ is $(1, 0)$; $j = 2$ is $(0, 1)$; $j = 3$ is $(-1, 0)$; $j = 4$ is $(0, -1)$ as shown in Figure.2-5. The contribution of the \mathbf{D}_{ij} 's to the energy of the magnetic state given in Eq. (2-19) is:

$$\mathcal{E}_D = 2D_1 (\mathbf{x} \cdot \mathbf{n}_3) \sin 2\pi q_2 - 2D_1 (\mathbf{y} \cdot \mathbf{n}_3) \sin 2\pi q_1 . \quad (2-25)$$

Setting for simplicity J_2 to zero and combining Eq. (2-20) with Eq. (2-25), we get

$$\mathcal{E} = -2J_1 [\cos 2\pi q_1 + \cos 2\pi q_2] + 2D_1 \cos \phi \sin 2\pi q_2 - 2D_1 \sin \phi \sin 2\pi q_1 . \quad (2-26)$$

Our goal is to check how the DMI leads to spiral states along either q_1 or q_2 , such as the ones shown in the results part of CrTe₂. To do that, consider the angle $\phi = \pi/2$, so the 2nd

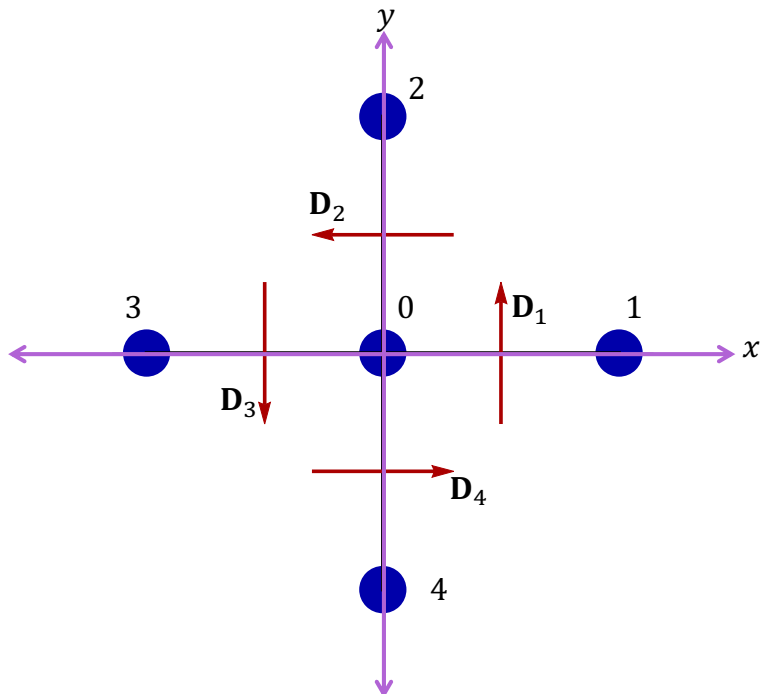


Figure 2-5.: Illustration of an example of DMI vectors with C_{4v} symmetry. The central blue circle represents the origin (0), and the neighboring sites are labeled as follows: right (1), up (2), left (3), and down (4). The red arrows indicate the direction of the DMI vectors.

term in Eq. 2-26 will be zero and the minimization of the other terms with respect to q_1 will lead to:

$$\tan 2\pi q_1 = \frac{D_1}{J_1}. \quad (2-27)$$

Now, by taking the limit of small DMI with respect to the Heisenberg exchange ($\frac{D_1}{J_1} \ll 1$), then $\tan 2\pi q_1 \approx 2\pi q_1$, which means:

$$2\pi q_1 = \frac{D_1}{J_1}. \quad (2-28)$$

This leads to a spiral state characterized with the $q_1 = -\frac{1}{2\pi} \frac{D_1}{J_1}$. Depending on the sign of J_1 , the spiral is FM ($J_1 > 0$) or AFM ($J_1 < 0$).

However, to minimize the combined energy for any angle ϕ , we take the derivatives with

respect to q_1, q_2, ϕ and find:

$$\tan 2\pi q_1 = \frac{D_1}{J_1} \sin \phi, \quad (2-29)$$

$$\tan 2\pi q_2 = -\frac{D_1}{J_1} \cos \phi, \quad (2-30)$$

$$\tan \phi = \frac{\sin 2\pi q_1}{\sin 2\pi q_2}. \quad (2-31)$$

Again, by taking the limit of small DMI with respect to the Heisenberg exchange ($\frac{D_1}{J_1} \ll 1$), then $\tan 2\pi q_1 \approx 2\pi q_1$, which means:

$$2\pi q_1 = \frac{D_1}{J_1} \sin \phi, \quad (2-32)$$

$$2\pi q_2 = -\frac{D_1}{J_1} \cos \phi, \quad (2-33)$$

$$\phi = \frac{q_1}{q_2}, \quad (2-34)$$

which simplifies Eq. 2-26 to:

$$\mathcal{E} = -4J_1 - \frac{D_1^2}{J_1}. \quad (2-35)$$

In this case, the competition between the D_1 and J_1 leads to either FM or AFM cycloids that are characterized by an optimal wave vector \mathbf{q}^* which can be derived from the given energy expressions and wave vector relations. The total energy of the system is given by Eq. 2-35, and the wave vector components are expressed as in Eqs. 2-32 and 2-33. Substituting these components, we find that the magnitude of the wave vector is

$$|\mathbf{q}^*| = \sqrt{q_1^2 + q_2^2} = \frac{1}{2\pi} \frac{D_1}{J_1}. \quad (2-36)$$

Therefore, the optimal wave vector \mathbf{q}^* that minimizes the energy is:

$$\mathbf{q}^* = \frac{1}{2\pi} \frac{D_1}{J_1} (\sin \phi, -\cos \phi), \quad (2-37)$$

with a magnitude of $|\mathbf{q}^*| = \frac{1}{2\pi} \frac{D_1}{J_1}$, indicating that the wave vector's components and orientation depend on the ratio of the DM interaction to the exchange interaction which leads to a FM- or AFM-cycloid state depending on the sign of J_1 (see Fig. 2-6). Finally, for any value of θ (conical spirals), we can write expand Eqs. (2-20) and (2-25) as:

$$\begin{aligned} \mathcal{E}_J = & -2J_1 [\sin^2 \theta (\cos 2\pi q_1 + \cos 2\pi q_2) + \cos^2 \theta] \\ & - 2J_2 [\sin^2 \theta (\cos 2\pi(q_1 + q_2) + \cos 2\pi(q_1 - q_2)) + \cos^2 \theta] \end{aligned} \quad (2-38)$$

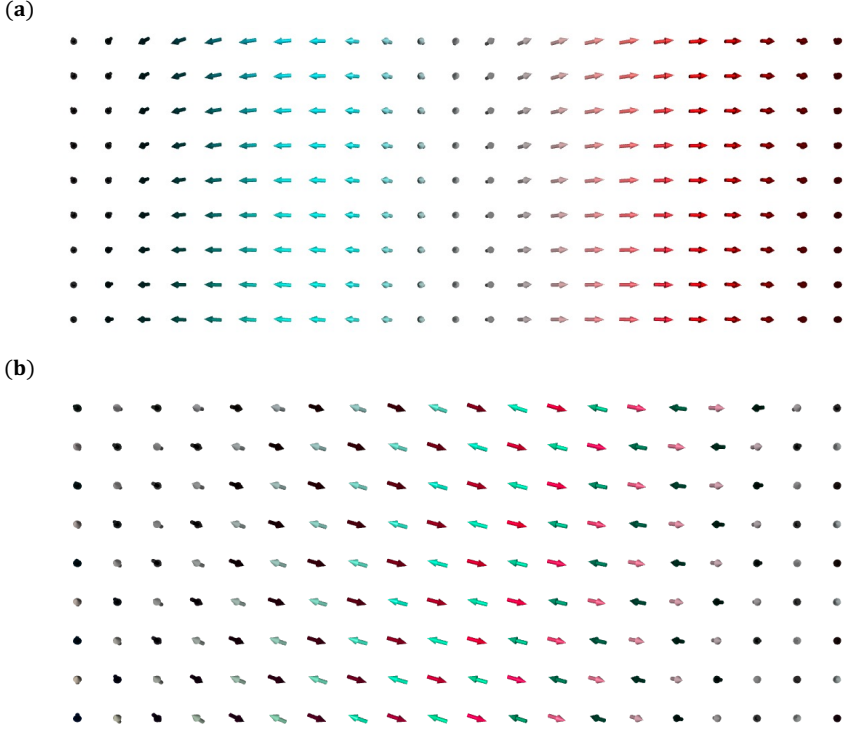


Figure 2-6.: Cycloid state including DMI. (a) FM-Cycloid state when $J_1 > 0$. (b) AFM-Cycloid state when $J_1 < 0$.

and

$$\mathcal{E}_D = 2D_1 (\mathbf{x} \cdot \mathbf{n}_3) \sin^2 \theta \sin 2\pi q_1 - 2D_1 (\mathbf{y} \cdot \mathbf{n}_3) \sin^2 \theta \sin 2\pi q_1 . \quad (2-39)$$

2.3.3. Spin models on a general Bravais lattice

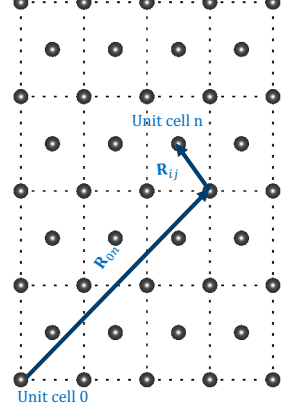
In this section, we want to calculate the contributions from each type of magnetic interaction to the total magnetic energy per site for any Bravais lattice, and to do this we rewrite Eq. 2-19 as:

$$\mathbf{S}_i = \sin \theta \left(\frac{e^{i\mathbf{q} \cdot \mathbf{R}_i} + e^{-i\mathbf{q} \cdot \mathbf{R}_i}}{2} \mathbf{n}_1 + \frac{e^{i\mathbf{q} \cdot \mathbf{R}_i} - e^{-i\mathbf{q} \cdot \mathbf{R}_i}}{2i} \mathbf{n}_2 \right) + \cos \theta \mathbf{n}_3 . \quad (2-40)$$

From the dot product $\mathbf{S}_i \cdot \mathbf{S}_j$ pertaining to the Heisenberg exchange interaction, we find a contribution to the total magnetic energy per site (See Appendix Sec. A.1.1):

Exchange energy

$$\mathcal{E}_J = -\sin^2 \theta [J(\mathbf{q}) - J(0)] - J(0), \quad (2-41)$$



where :

$$J(\mathbf{q}) = \sum_{nij} J_{0i,nj} e^{-i\mathbf{q} \cdot (\mathbf{R}_{0n} + \mathbf{R}_{ij})} \quad (2-42)$$

$$J(0) = \sum_j J_{0j}. \quad (2-43)$$

with \mathbf{R}_{0n} is a vector connecting unit cells 0 and n , and \mathbf{R}_{ij} is a vector connecting atoms μ and ν in the same unit cell.

From the cross product $\mathbf{S}_i \times \mathbf{S}_j$ associated with the DMI the contribution to the total energy is (See Appendix Sec. A.1.2):

DMI energy

$$\mathcal{E}_D = -\sin^2 \theta \sum_{nij} (\mathbf{n}_3 \cdot \mathbf{D}_{0i,nj}) \sin \mathbf{q} \cdot (\mathbf{R}_{0n} + \mathbf{R}_{ij}). \quad (2-44)$$

The remaining contributions of our interest to the total energy are the Zeeman and magnetic anisotropy contributions. Here the phase angle ϕ to the spins in Eq. 2-12 is needed. The contribution to the energy from the magnetic field is:

Zeeman energy

$$\mathcal{E}_B = -\sin \theta (\cos \phi \mathbf{n}_1 + \sin \phi \mathbf{n}_2) \cdot \mathbf{B} \delta_{\mathbf{q},0} - \cos \theta \mathbf{n}_3 \cdot \mathbf{B}, \quad (2-45)$$

while the magnetic anisotropy contribution reads (See Appendix Sec. A.1.3):

Magnetic anisotropy energy

$$\begin{aligned}
 \mathcal{E}_A = & -K (\mathbf{n}_1 \cdot \mathbf{z})^2 \sin^2 \theta \left(\frac{1}{2} + \frac{1}{2} \delta_{\mathbf{q}, \frac{\mathbf{z}}{2}} \cos 2\phi \right) - K \sin^2 \theta (\mathbf{n}_2 \cdot \mathbf{z})^2 \left(\frac{1}{2} - \frac{1}{2} \delta_{\mathbf{q}, \frac{\mathbf{z}}{2}} \cos 2\phi \right) \\
 & - K \cos^2 \theta (\mathbf{n}_3 \cdot \mathbf{z})^2 - 2K \delta_{\mathbf{q}, \mathbf{0}} \sin \theta \cos \theta \cos \phi (\mathbf{n}_1 \cdot \mathbf{z}) (\mathbf{n}_3 \cdot \mathbf{z}) \\
 & - 2K \delta_{\mathbf{q}, \mathbf{0}} \sin \theta \cos \theta \sin \phi (\mathbf{n}_2 \cdot \mathbf{z}) (\mathbf{n}_3 \cdot \mathbf{z}) - 2K \delta_{\mathbf{q}, \frac{\mathbf{z}}{2}} \sin^2 \theta \sin 2\phi (\mathbf{n}_1 \cdot \mathbf{z}) (\mathbf{n}_2 \cdot \mathbf{z}).
 \end{aligned} \tag{2-46}$$

If we consider θ equal to zero, only the third term of the previous equation remains, simplifying to $-K (\mathbf{n}_3 \cdot \mathbf{z})^2$. Consequently, this leads to the expression detailed in Eq. 2-10, where $\alpha = \mathbf{z}$.

2.4. Topological magnetism: skyrmions and merons

Topological magnetism is an advanced field in condensed matter physics that involves the study of magnetic systems where the spatial arrangements of the magnetic moments form stable configurations due to their topological characteristics. These configurations are referred to as topological spin textures and exhibit stability that arises from topological invariants, rather than from energetic considerations that govern conventional magnetic systems. In this section, we discuss three distinct types of topological spin textures, namely skyrmions, merons, and antimerons.

2.4.1. Skyrmions

Magnetic skyrmions are topological swirling spin configurations that exhibit unique quasi-particle properties and possess a helical chiral structure. This structure is characterized by gradual changes in the atomic spin direction from the outer edge to the center, demonstrating a fixed chirality when the DMI is present. The optimal chiral structure of a skyrmion is primarily attributed to the interplay between the Heisenberg exchange interaction and the DMI. Generally, there are two main types of magnetic skyrmions: Bloch-type [80] and Néel-type [81] skyrmions, depending on how the swirling of the DMI vectors, which is imposed by the nature of the material. The underlying spin-textures are illustrated in Fig. 2-7. The DMI can be categorized into two types based on the source of inversion symmetry breaking: Bulk DMI and Interfacial DMI. The Bulk DMI (See Fig. 2-7 (d)) occurs in materials where the crystal structure itself lacks inversion symmetry, such as in the B20 phase of materials like MnSi [82] or FeGe [83], leading to a uniform DMI vector throughout the crystal and typically resulting in Bloch-type skyrmions (See Fig. 2-7 (b)). In these skyrmions, the spins rotate in the tangential planes, perpendicular to the radial directions from the core to the periphery. On the other hand, Interfacial DMI (See Fig. 2-7 (c)) arises

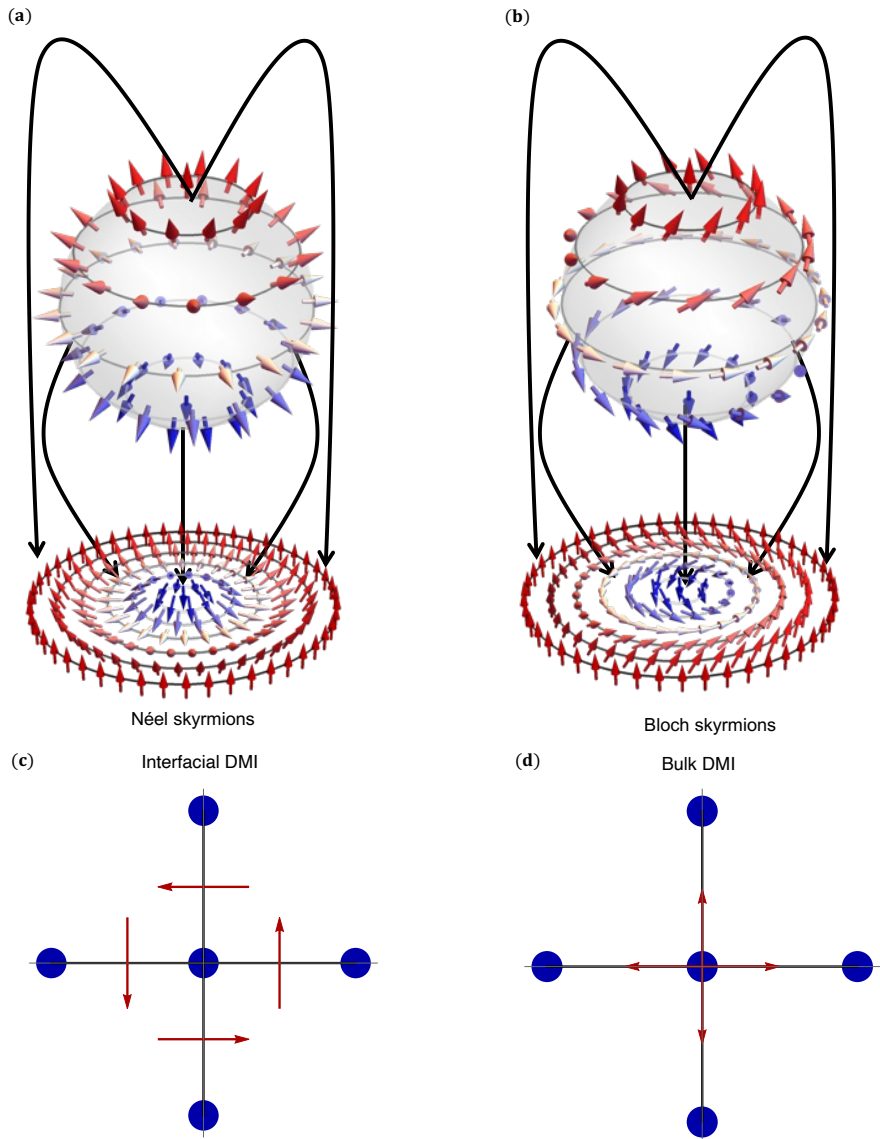


Figure 2-7.: **Two examples of skyrmionic textures due to different types of DMI.** (a,b) The spin-textures of Néel, and Bloch skyrmions; respectively, where the black arrows represent the projection onto the surface of a unit sphere. (c,d) Schematic representation of DMI vectors leading to two distinct skyrmions.

in thin film systems or at interfaces between different materials where inversion symmetry is explicitly broken, commonly observed in multilayer systems (eg. Co/Pt) [84, 85] and 2D Van der Waals heterostructures [27]. This interaction is strongest at the interface and decays away from it, leading to the formation of Néel-type skyrmions (See Fig. 2-7 (a)), where the spins rotate in the radial planes from the core to the periphery.

Compared with conventional ferromagnetic or antiferromagnetic states, magnetic skyrmions exhibit non-trivial topological properties. These properties can be quantified by a topological number, also known as a topological charge T . This topological charge is a quantized value, indicating the number of times a texture wraps around the unit sphere. As shown in Figure 2-7, the wrapping process of Néel and Bloch skyrmions is illustrated by the black arrows. The arrows indicate the direction of the wrapping around the core of the skyrmion. It is mathematically expressed by the integral [86]:

$$T = \frac{1}{4\pi} \int d^2r \mathbf{S} \cdot \left(\frac{\partial \mathbf{S}}{\partial x} \times \frac{\partial \mathbf{S}}{\partial y} \right), \quad (2-47)$$

where \mathbf{S} denotes the unit vector in the direction of the local magnetization as defined in the micromagnetic limit. This vector may be represented in spherical coordinates utilizing the symmetry of skyrmionic textures as:

$$\mathbf{S}(\mathbf{r}) = \begin{pmatrix} \cos \Phi(\phi) \sin \theta(r) \\ \sin \Phi(\phi) \sin \theta(r) \\ \cos \theta(r) \end{pmatrix}, \quad (2-48)$$

where the polar angle $\Phi(\phi)$ of the magnetization depends on the polar angle ϕ of the position vector \mathbf{r} and $\theta(r)$ depends on the length r of the position vector \mathbf{r} .

We can rewrite the equation of topological charge from Eq. 2-48 [20]:

$$T = \frac{1}{4\pi} \int_0^\infty dr \int_0^{2\pi} d\phi \frac{d\theta}{dr} \sin \theta \left(\frac{d\Phi}{d\phi} \right) = p \cdot w \quad (2-49)$$

where polarity p and vorticity w reference the magnetization. Polarity specifies the orientation of the magnetization at the core of the spin texture, indicating whether it points upward or downward. On the other hand, vorticity characterizes the sense of rotation within the in-plane magnetic texture. Therefore, polarity p can take values of ± 1 , representing either an upward or downward core magnetization orientation. Vorticity w can have values of $0, \pm 1, \pm 2$, and so on, indicating various degrees of in-plane magnetic rotation. For example, both Néel-type, and Bloch skyrmions have a topological charge T equal -1, which is due to $p = +1$ and $w = -1$.

2.4.2. Merons and antimerons

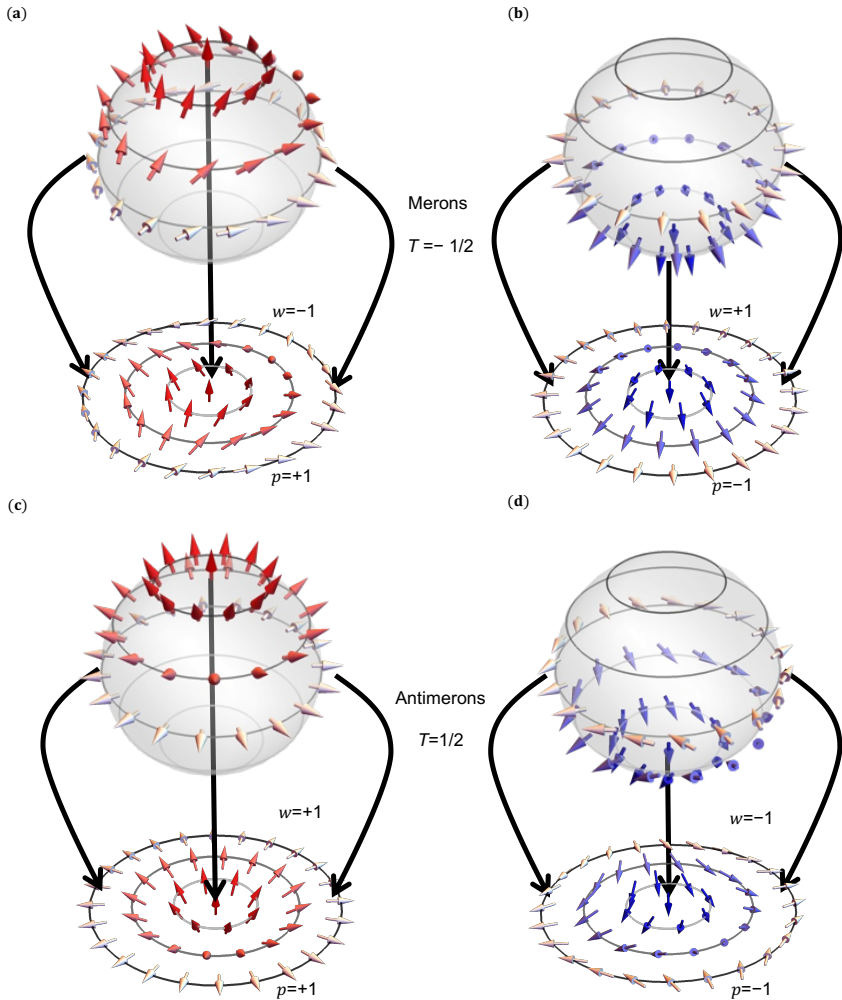


Figure 2-8.: Spin-textures of merons and antimerons with the projection onto the surface of a unit sphere. Case of (a) a meron with polarity $p = +1$, and $w = -1$; (b) a meron with polarity $p = -1$, and $w = +1$; (c) an antimeron with polarity $p = +1$, and $w = +1$; (d) an antimeron with polarity $p = -1$, and $w = -1$.

Merons and antimerons are characterized by half-integer topological charges, with $T = -1/2$ for merons and $T = +1/2$ for antimerons. A meron represents a half skyrmion, where the spin texture wraps only a semi-sphere, which is reflected in the figure by the arrows that encompass just half of the hemisphere as shown in Fig. 2-8 (a,b). An antimeron covers the complementary hemisphere of the sphere as shown in Fig. 2-8 (c,d). Similarly to the skyrmion, the winding number and polarity are important to characterize the topology of the meron/antimeron. The sign of the winding number w indicates whether one has a vortex for a value of +1 or an antivortex for a value of -1.

3.Methods: Density Functional Theory

In the realm of computational materials science and solid-state physics, many theoretical techniques exist to study and simulate the properties and behaviors of materials. Each technique offers unique insights into specific length and time scales under exploration, providing rich details about the systems under study. One of the standout methods is the Density Functional Theory (DFT) which solves the many-body problem by focusing on the electronic density, instead of finding the wave functions. In DFT the total energy of a system is minimized to find the underlying ground state. The approach follows in practice a self-consistent iterative scheme and enables the simulation of the electronic structure of realistic materials. This chapter delves deep into the fundamental principles of DFT, focusing on two DFT-based methodologies utilized in the thesis. The first approach is based on plane waves [60] and pseudopotentials [61,62] as implemented in the Quantum Espresso code [63–65]. The second approach employs the Korringa-Kohn-Rostoker (KKR) green function method [66,67], which is based on multiple scattering theory as implemented in JuKKR code [68–71] and developed in our group at the Research Center of Jülich.

3.1. The many-body problem

For a solid system consisting of N electrons and n nuclei, the fundamental equation to be solved to extract the eigenenergies and eigenstates is the time-independent many-electron Schrödinger equation:

$$\hat{H}\Psi(\mathbf{r}_1, \mathbf{r}_2, \dots, \mathbf{r}_N, \mathbf{R}_1, \mathbf{R}_2, \dots, \mathbf{R}_n) = E\Psi(\mathbf{r}_1, \mathbf{r}_2, \dots, \mathbf{r}_N, \mathbf{R}_1, \mathbf{R}_2, \dots, \mathbf{R}_n), \quad (3-1)$$

where:

- $\Psi(\mathbf{r}_1, \mathbf{r}_2, \dots, \mathbf{r}_N)$ is the many-electron wavefunction representing the quantum state of all N electrons, each defined by its position vector \mathbf{r}_i .
- $\Psi(\mathbf{R}_1, \mathbf{R}_2, \dots, \mathbf{R}_n)$ is the wavefunction representing the quantum state of all n nuclei, each defined by its position vector \mathbf{R}_A .
- E is the energy eigenvalue associated with the wavefunction Ψ .

The Hamiltonian operator \hat{H} , which describes the total energy of the system, is given by:

Hamiltonian operator

$$\begin{aligned}
 \hat{H} = & \underbrace{\sum_{i=1}^N \frac{\hbar^2}{2m_e} \nabla_i^2}_{\text{Kinetic energy of electrons } (T_e)} + \underbrace{\sum_{A=1}^n \frac{\hbar^2}{2M_A} \nabla_A^2}_{\text{Kinetic energy of nuclei } (T_n)} + \underbrace{\sum_{A<B}^n \frac{Z_A Z_B e^2}{4\pi\epsilon_0 |\mathbf{R}_A - \mathbf{R}_B|}}_{\text{Repulsion between nuclei } (V_{n-n})} \\
 + & \underbrace{\sum_{i<j}^N \frac{e^2}{4\pi\epsilon_0 |\mathbf{r}_i - \mathbf{r}_j|}}_{\text{Electron-electron repulsion } (V_{e-e})} + \underbrace{\sum_{i=1}^N \sum_{A=1}^n \frac{-Z_A e^2}{4\pi\epsilon_0 |\mathbf{r}_i - \mathbf{R}_A|}}_{\text{Attraction between electrons and nuclei } (V_{e-n})}.
 \end{aligned} \tag{3-2}$$

Since electrons are much lighter than nuclei, they move faster. So, when we look at how electrons move, it is easier to think of nuclei as not moving at all. This insight allows for a modification in Eq. 3-2, where the nuclear interaction term can be replaced by a constant E_{n-n} , while also neglecting the kinetic energy of the nuclei (T_n). This simplification is referred to as the Born-Oppenheimer approximation (BO) [87]:

$$\hat{H}_{BO} = T_e + V_{e-n} + V_{e-e} + E_{n-n}. \tag{3-3}$$

By merging the third and fourth terms of this equation, we introduce V_{ext} , leading to a more concise Hamiltonian for electrons:

$$\hat{H}_{BO} = T_e + V_{e-e} + V_{ext}. \tag{3-4}$$

Notably, even with the Born-Oppenheimer approximation, the electronic problem remains a complex quantum many-body problem. The system's wavefunction, $\Psi(\mathbf{r}_1, \mathbf{r}_2, \dots, \mathbf{r}_N)$, hinges upon the position coordinates of every electron due to their interactions, preventing a breakdown into individual particle contributions. This intricacy means an exact solution remains elusive for multi-electrons realistic materials. The complexity of the problem grows exponentially with the number of particles (N). For example, a Cr atom contains 24 electrons, giving $3 \times 24 = 72$ degrees of freedom. Solving the Hamiltonian on a real-space grid with 12 points in each dimension would require storing 12^{72} numbers—a very large number-. Considering that systems in solids contain thousands of atoms, storing such an amount of data is impractical. We need a better way to study solids using quantum mechanics. This can be achieved with Density Functional Theory (DFT), which will be explored in the next section.

3.2. Density functional theory: Overview

In 1964, Hohenberg and Kohn [88] pioneered the foundation for DFT. At its core, DFT aims to tackle the complex many-body electronic problem by focusing on the single-particle probability density, which only relies on a single spatial variable. The single-particle probability

density of the ground state, denoted as $n_0(\mathbf{r})$, for a collection of N interacting electrons described by the Hamiltonian in Eq. 3-4 is given by:

$$n_0(\mathbf{r}) = \int |\Psi(\mathbf{r}, \mathbf{r}_2, \mathbf{r}_3, \dots, \mathbf{r}_N)|^2 dr_2 dr_3 \dots dr_N. \quad (3-5)$$

It is evident that if V_{ext} in Eq. 3-4 is known, the wave function can be determined, which in turn determines $n_0(\mathbf{r})$. Likewise, and as stated in the first Hohenberg-Kohn theorem, the ground-state electron density $n_0(\mathbf{r})$ uniquely determines the external potential $V_{\text{ext}}(\mathbf{r})$, up to an additive constant. This theorem implies that for any given ground-state density $n_0(\mathbf{r})$, there is a unique corresponding external potential $V_{\text{ext}}(\mathbf{r})$ (up to a constant). To prove that, suppose there are two different external potentials, $V_{\text{ext}}^{(1)}(\mathbf{r})$ and $V_{\text{ext}}^{(2)}(\mathbf{r})$, that yield the same ground-state density $n_0(\mathbf{r})$. Let $\Psi_0^{(1)}$ and $\Psi_0^{(2)}$ be the corresponding ground-state wavefunctions. These wavefunctions should produce the same electron density:

$$n_0(\mathbf{r}) = \langle \Psi_0^{(1)} | \hat{n}(\mathbf{r}) | \Psi_0^{(1)} \rangle = \langle \Psi_0^{(2)} | \hat{n}(\mathbf{r}) | \Psi_0^{(2)} \rangle. \quad (3-6)$$

Since $V_{\text{ext}}^{(1)}(\mathbf{r}) \neq V_{\text{ext}}^{(2)}(\mathbf{r})$, the Hamiltonians \hat{H}_1 and \hat{H}_2 differ by more than a constant. Therefore, the wavefunctions $\Psi_0^{(1)}$ and $\Psi_0^{(2)}$ should correspond to different energy expectation values. However, the variational principle states that the ground-state energy for a given density is unique and minimal. If $\Psi_0^{(1)}$ and $\Psi_0^{(2)}$ produce the same density, they should have the same ground-state energy, leading to a contradiction. Thus, $n_0(\mathbf{r})$ uniquely determines $V_{\text{ext}}(\mathbf{r})$. This principle implies that any observation of the ground state of a system is exclusively portrayed as a function of its ground-state electron density, leading to the term density functional theory.

The energy of the entire many-body system can thus be expressed as a functional of the electron density:

$$E = E[n] = T_e[n] + V_{e-e}[n] + V_{\text{ext}}[n]. \quad (3-7)$$

Furthering their study, Hohenberg and Kohn showcased a second theorem asserting that the total energy function $E[n]$ finds its minimal value at the ground state density $n_0(\mathbf{r})$. This insinuates that this density can be deduced using the variational method. While the theorems put forward by Hohenberg-Kohn are instrumental, they do not offer a feasible plan for minimizing Eq. 3-7 to achieve the ground state density. Kohn and Sham provided more details on this topic, which are summarized briefly below [89].

3.2.1. Kohn-Sham Formulation

Kohn and Sham [89] offers a structured technique to minimize the total energy functional, thereby establishing the foundation for contemporary DFT calculations. Their method revolves around representing the complex interactions within a many-body system by using a simpler system of non-interacting entities. This is done under the stipulation that the latter has the identical ground state density and hence, the same ground state energy as the sys-

tem under analysis. The system of non-interacting particles is inherently straightforward to tackle. The corresponding single-particle wavefunctions, ψ_i , formulate the electron density:

$$n(\mathbf{r}) = \sum_i |\psi_i(\mathbf{r})|^2, \quad (3-8)$$

which is the fundamental component for establishing the Kohn-Sham energy functional:

Kohn-Sham energy functional

$$E_{KS}[n] = T_s[n] + \int n(\mathbf{r})V_{ext}(\mathbf{r})d\mathbf{r} + E_H[n] + E_{xc}[n], \quad (3-9)$$

where :

- $T_s[n]$ represents the kinetic energy of the non-interacting particles:

$$T_s[n] = -\frac{\hbar^2}{2m_e} \sum_i \langle \psi_i | \nabla^2 | \psi_i \rangle. \quad (3-10)$$

- The second term denotes the energy due to the electron's interaction with the external potential V_{ext} .
- $E_H[n]$ signifies the classical Coulomb repulsion (Hartree) energy:

$$E_H[n] = \frac{e^2}{2} \int \frac{n(\mathbf{r})n(\mathbf{r}')}{|\mathbf{r} - \mathbf{r}'|} d\mathbf{r}d\mathbf{r}'. \quad (3-11)$$

- $E_{xc}[n]$ encapsulates the exchange and correlation (xc) energy, factoring in all many-body effects pivotal to mapping the non-interacting particles to the many-body system.

While all contributions to the Kohn-Sham energy functional in Eq. 3-9 are clearly elucidated for every system, the latter term is conventionally approximated. Applying the variational principle on Eq. 3-9, single-particle Kohn-Sham equations are derived:

$$\hat{H}_{KS}\psi_i(\mathbf{r}) = \epsilon_i\psi_i(\mathbf{r}), \quad (3-12)$$

or

$$\left[\frac{\hbar^2}{2m_e} \nabla^2 + V_{eff}(\mathbf{r}) \right] \psi_i(\mathbf{r}) = \epsilon_i\psi_i(\mathbf{r}). \quad (3-13)$$

Here, ϵ_i stands for the single-particle energies. The effective Kohn-Sham potential $V_{eff}(\mathbf{r})$ stands for the functional derivative of the energy functional with respect to $n(\mathbf{r})$ of $E_{KS}[n]$

excluding the kinetic energy term $T_s[n]$:

$$V_{eff}(\mathbf{r}) = \frac{\delta(E_{KS}[n] - T_s[n])}{\delta n(\mathbf{r})} = V_{ext}(\mathbf{r}) + V_H(\mathbf{r}) + V_{xc}(\mathbf{r}), \quad (3-14)$$

where:

- $V_H(\mathbf{r})$ corresponds to the electrostatic Hartree potential:

$$V_H(\mathbf{r}) = \frac{\delta E_H[n]}{\delta n(\mathbf{r})}. \quad (3-15)$$

- $V_{exc}(\mathbf{r})$ symbolizes the exchange-correlation potential:

$$V_{exc}(\mathbf{r}) = \frac{\delta E_{exc}[n]}{\delta n(\mathbf{r})}. \quad (3-16)$$

3.2.2. DFT for spin-polarized systems

Through a decomposition of the charge density $n(\mathbf{r})$ into its individual spin components, DFT is broadened to encompass spin-polarized systems [90, 91]:

$$n(\mathbf{r}) = n_{\uparrow}(\mathbf{r}) + n_{\downarrow}(\mathbf{r}) \quad (3-17)$$

In this representation, $n_{\uparrow}(\mathbf{r})$ and $n_{\downarrow}(\mathbf{r})$ symbolize respectively the density of majority and minority spin electrons. Consequently, the magnetic density can be defined as:

$$m(\mathbf{r}) = n_{\uparrow}(\mathbf{r}) - n_{\downarrow}(\mathbf{r}). \quad (3-18)$$

Disregarding spin-orbit coupling and assuming collinear magnetism, both majority and minority spin electrons adhere to two distinct Kohn-Sham equations, each to be solved for each spin channel independently from the other. The spin-dependent effective Kohn-Sham potential can be expressed as:

$$V_{\text{eff}}^{\sigma}(\mathbf{r}) = V_{\text{ext}}(\mathbf{r}) + \int \frac{e^2 n(\mathbf{r}')}{|\mathbf{r} - \mathbf{r}'|} d\mathbf{r}' + \frac{\delta E_{exc}[n_{\uparrow}(\mathbf{r}), n_{\downarrow}(\mathbf{r})]}{\delta n_{\sigma}(\mathbf{r})}, \quad (3-19)$$

where σ symbolizes the spin index, explicitly $\sigma = (\uparrow, \downarrow)$. Additionally, the Kohn-Sham equations are expandable to incorporate relativistic modifications, spin-orbit coupling [92] and non-collinear magnetism [93, 94], facilitated by the introduction of dual component spinor wavefunctions. While Kohn and Sham provide a mapping procedure between the true many-body system and the auxiliary one made of non-interacting particles, the exchange-correlation energy functional remains unknown but can be approximated, as discussed in the next section.

3.2.3. Approximations to the exchange-correlation energy functional

Determining an accurate approximation for the exchange-correlation energy is pivotal in DFT due to its computational cost and impact on system property predictions. This section provides an overview of two popular methods:

- **Local Spin Density Approximation (LSDA)** [95]: This approximation was one of the first approximations introduced and remains a widely used DFT functional. Its extension, LSDA, factors in different spin channels. Using this approach, the exchange-correlation energy is derived from a homogeneous electron gas:

$$E_{\text{exc}}^{\text{LSDA}}[n_{\uparrow}, n_{\downarrow}] = \int n(\mathbf{r}) \epsilon_{\text{exc}}^{\text{hom}}(n_{\uparrow}(\mathbf{r}), n_{\downarrow}(\mathbf{r})) d\mathbf{r} . \quad (3-20)$$

Generally, LSDA performs well for metals and offers reasonable results for varied density systems due to systematic error cancellations [96–98]. However, LSDA often underestimates semiconductor band gaps, sometimes erroneously predicting a metallic ground state.

- **Generalized Gradient Approximation (GGA)** [99]: GGA builds on LSDA by incorporating not just the local electron density but also its gradient. The energy functional for the spin-polarized GGA is expressed as:

$$E_{\text{exc}}^{\text{GGA}}[n_{\uparrow}, n_{\downarrow}] = \int n(\mathbf{r}) \epsilon_{\text{exc}}(n_{\uparrow}(\mathbf{r}), n_{\downarrow}(\mathbf{r}), \nabla n_{\uparrow}(\mathbf{r}), \nabla n_{\downarrow}(\mathbf{r})) d\mathbf{r} . \quad (3-21)$$

Among the various GGA formulations, the Perdew, Burke, and Ernzerhof (PBE) method stands out. GGA functionals usually outperform LSDA, enhancing total energies and structural energy differences.

As we discussed before, the DFT is a widely used computational approach for investigating the electronic structure of many-body systems. The central challenge of DFT is to solve the Kohn-Sham equations, which transform the complex many-body problem into a set of self-consistent single-particle equations. In this thesis, two prominent methods for solving the Kohn-Sham equations are used: the plane-wave pseudo-potential method Quantum Espresso and the Korringa-Kohn-Rostoker (KKR) Green function method. To study the magnetic properties of 2D materials, we primarily employed the KKR method, which is thus the main method discussed in the subsequent sections. Quantum Espresso is mainly used for geometrical relaxations and is briefly introduced in the next section.

3.3. Plane wave basis and pseudopotentials method

In DFT, one of the most common approaches to solving the Kohn-Sham equations involves using plane waves as a basis set. The rationale for this choice lies in the periodicity of plane

waves, which makes them naturally suitable for studying periodic systems, such as crystalline materials. A plane wave, represented as $e^{i\mathbf{G}\cdot\mathbf{r}}$, where \mathbf{G} is a reciprocal lattice vector and \mathbf{r} is a position vector in real space, can be thought of as a wave oscillating uniformly in all directions. By combining multiple such waves, one can approximate more complex functions, especially over periodic domains. The Bloch theorem postulates that the wave functions of electrons in a periodic potential can be written as a product of a plane wave and a function with the same periodicity as the crystal. Given this, the Kohn-Sham orbitals, which describe the behavior of electrons in a system, can be expanded in terms of plane waves [60]:

$$\psi_{i,\mathbf{k}}(\mathbf{r}) = \sum_{|\mathbf{G}| < G_{\max}} c_{i\mathbf{k},\mathbf{G}} e^{i(\mathbf{k}+\mathbf{G})\cdot\mathbf{r}}, \quad (3-22)$$

where $\psi_{i,\mathbf{k}}(\mathbf{r})$ is the KS wave function for band index i and wavevector \mathbf{k} , $c_{i\mathbf{k},\mathbf{G}}$ are the expansion coefficients, \mathbf{G} represents the reciprocal lattice vectors, and the sum is restricted by a cutoff G_{\max} , which limits the plane waves included in the representation and defines an energy cutoff, often denoted E_{cut} . The latter determines the maximum kinetic energy of the plane waves included in the basis set. Mathematically, this restriction can be expressed as:

$$\frac{\hbar^2}{2m_e} |\mathbf{G} + \mathbf{k}|^2 \leq E_{\text{cut}}. \quad (3-23)$$

In atomic systems, the core electrons remain largely static during chemical reactions. Thus, pseudopotentials emerge as a practical approach to sidestep the direct consideration of these core electrons [61, 62]. By replacing them with an effective potential, pseudopotentials encapsulate the interaction between valence electrons and atomic nuclei. The focus on valence electrons instead of considering all electrons at once reduces the computational overhead. Within the plane wave framework, pseudopotentials are particularly beneficial as they permit the application of a plane wave energy cutoff by omitting high kinetic energy states of core electrons. There are various families of pseudopotentials, characterized by the position of the core cut-off radius, the mathematical structure, the shape, and the conditions imposed on the pseudo-wavefunction. Norm-conserving pseudopotentials (NCPPs) require that the pseudo-wavefunction preserves the norm of the original full-potential wavefunction. However, this norm-preservation condition can be computationally expensive for many systems, such as transition metals, as it requires a large number of plane waves to expand the wave function. To mitigate this computational cost, Projector-Augmented Waves (PAW) [100] relax this condition, reducing the number of \mathbf{G} -vectors needed to describe the pseudo-wavefunction's variation in the core region.

3.3.1. Structural Optimization

Structural optimization relies heavily on calculating forces and stresses. The forces on atoms are obtained as derivatives of the total energy with respect to atomic positions. According to the Hellmann-Feynman theorem [101], these forces are given by the expectation value of

the derivative of the external potential:

$$F_\mu = -\frac{\partial E}{\partial R_\mu} = -\sum_i f_i \langle \psi_i | \left. \frac{\partial V_{ext}}{\partial R_\mu} \right| \psi_i \rangle = -\int n(\mathbf{r}) \frac{\partial V_{ext}}{\partial R_\mu} d\mathbf{r}, \quad (3-24)$$

where F_μ is the force on atom μ , E is the total energy, R_μ is the position of atom μ , ψ_i are the electronic wavefunctions, and $n(r)$ is the electron density. In periodic systems, there are two types of displacements to consider:

- **Atomic Displacements:** These are the movements of atoms within the unit cell and are determined by the forces.
- **Elastic Displacements:** These change the shape of the unit cell and are determined by the stresses. The stress tensor $\sigma_{\alpha\beta}$ is given by:

$$\sigma_{\alpha\beta} = -\frac{1}{\Omega} \frac{\partial E}{\partial \epsilon_{\alpha\beta}}, \quad (3-25)$$

where Ω is the volume of the unit cell and $\epsilon_{\alpha\beta}$ is the strain tensor.

A common approach is to use quasi-Newton methods, such as the Broyden-Fletcher-Goldfarb-Shanno (BFGS) algorithm.

3.3.2. Quantum ESPRESSO code

We utilize the Quantum ESPRESSO (QE) code for relaxing our structures using the BFGS algorithm [63–65]. QE is a suite of computer programs for electronic structure calculations and materials modeling at the nanoscale. It is based on DFT, plane waves as the basis set, which is essential for solid-state electronic structure calculations because of their inherent periodic nature, and pseudopotentials [61, 62] from PSLibrary [102] to replace the core electrons, simplifying calculations for valence electrons. For our 2D vdW materials, we used the non-local vdW-DF to correct the standard exchange-correlation (exc) functionals [103]. The vdW-DF functional is expressed as:

$$E_{xc} = E_{GGA,x} + E_{LDA,c} + E_{nl,c}, \quad (3-26)$$

where $E_{nl,c}$ is the non-local correlation energy term calculated as:

$$E_{nl,c} = \frac{1}{2} \int d^3r \int d^3r' n(\mathbf{r}) \kappa(\mathbf{r}, \mathbf{r}') n(\mathbf{r}'). \quad (3-27)$$

$\kappa(\mathbf{r}, \mathbf{r}')$ is the kernel analogous to the Coulomb interaction, and $n(\mathbf{r})$ is the electron density. This inclusion provides a more accurate description of dispersion interactions by integrating corrections directly within the DFT formalism. This approach addresses the critical need

for incorporating dispersion interactions in DFT, especially for accurately predicting the properties of materials involving weakly interacting systems.

In this thesis, we conduct our calculations using this code in several steps. First, define the system structure by specifying the arrangement, positions, and types of atoms in the 2D vdW materials. Then, perform PAW self-consistent calculations using the Quantum Espresso `pw.x` code with the PAW option to conduct self-consistent DFT calculations, allowing the relaxation of the atoms, and the unit cell to converge the system as explained in the previous subsection. Finally, extract the relaxed positions of the magnetic atoms to use in KKR DFT calculations. KKR will be discussed in the next section.

3.4. Korringa-Kohn-Rostoker (KKR) Green function method

As we discussed before, the Korringa-Kohn-Rostoker (KKR) Green function method [66,67] is another method used to solve the Kohn-Sham equation in unique approach. It leans on the principles of multiple scattering theory, visualizing the electron wave's journey within a solid as a series of single scattering events occurring at distinct atoms. The initial step involves calculating the singular scattering event caused by the wave encountering the potential of individual atoms, represented by the single site scattering "t-matrix". Subsequent steps consider the multiple scatterings based on the specific atomic arrangement in the crystal. The resulting equations show a beautiful separation between potential and structural properties, which are typical for the KKR method. This method is based on a Green function approach which is the starting point of the following discussion. For additional details, we recommend consulting the references [69,104–107].

3.4.1. General properties of the Green function

Consider a system characterized by the time-independent Hamiltonian \mathcal{H} with a complete set of eigenfunctions $\{|\psi_n\rangle\}$ and corresponding eigenvalues E_n , such that

$$\mathcal{H}|\psi_n\rangle = E_n|\psi_n\rangle . \quad (3-28)$$

The Green function $G(z)$ is defined as the operator that satisfies the equation

$$(z\mathbb{I} - \mathcal{H})G(z) = \mathbb{I} , \quad (3-29)$$

where z is a complex number with a finite imaginary part and \mathbb{I} is the identity operator. Using the eigenvalues and eigenfunctions, the Green function can be represented in its spectral form, known as the Lehmann representation,

$$G(z) = \sum_n \frac{|\psi_n\rangle\langle\psi_n|}{z - E_n} . \quad (3-30)$$

3.4.1.1. Dyson equation

Some of the most useful properties of Green functions become evident when examining a perturbed system. Consider a Hamiltonian \mathcal{H} for a system of interest, which can be expressed as

$$\mathcal{H} = \mathcal{H}_0 + V, \quad (3-31)$$

where \mathcal{H}_0 represents an unperturbed, solvable physical problem and V denotes the perturbation introducing the difference to the complete system.

The Green functions for the full Hamiltonian and the reference Hamiltonian are then given by

$$G(z) = (z\mathbb{I} - \mathcal{H})^{-1}, \quad G_0(z) = (z\mathbb{I} - \mathcal{H}_0)^{-1}. \quad (3-32)$$

One can relate the two Green functions via the well-known Dyson equation:

$$G(z) = G_0(z) + G_0(z)VG(z) = G_0(z)(\mathbb{I} - VG(z))^{-1}. \quad (3-33)$$

By iteratively inserting this expression into itself, we obtain

$$\begin{aligned} G(z) &= G_0(z) + G_0(z)VG(z) \\ &= G_0(z) + G_0(z)VG_0(z) + G_0(z)VG_0(z)VG(z) \\ &= G_0(z) + G_0(z)VG_0(z) + G_0(z)VG_0(z)VG_0(z) + \dots \end{aligned} \quad (3-34)$$

Such a series allows us to express the desired Green function G exclusively in terms of the two operators G_0 and V . If the potential V is a small perturbation, the series in [Eq. 3-34](#) converges. By applying [Eq. 3-34](#) up to a certain order in V , one can achieve the desired accuracy for G without computing the matrix inversion in [Eq. 3-33](#). [Eq. 3-34](#) can be rewritten as

$$G(z) = G_0(z) + G_0(z)T(z)G_0(z), \quad (3-35)$$

where $T(z)$ is the transition matrix or T-matrix. It can be verified that

$$T(z) = V + VG_0(z)V + VG_0(z)VG_0(z)V + \dots \quad (3-36)$$

or

$$T(z) = V + VG_0(z)T(z). \quad (3-37)$$

Thus, finding the full Green function $G(z)$ is reduced to finding the T-matrix $T(z)$.

3.4.1.2. Lippmann-Schwinger equation

The aforementioned Hamiltonian operators \mathcal{H} and \mathcal{H}_0 solve the equations

$$(z\mathbb{I} - \mathcal{H}_0)|\psi_0\rangle = 0, \quad (3-38)$$

$$(z\mathbb{I} - \mathcal{H})|\psi\rangle = (z\mathbb{I} - \mathcal{H}_0)|\psi\rangle - V|\psi\rangle, \quad (3-39)$$

with their respective wave functions $|\psi\rangle$ and $|\psi_0\rangle$. Using the ansatz

$$|\psi\rangle = |\psi_0\rangle + \delta|\psi\rangle, \quad (3-40)$$

leads to

$$0 = (z\mathbb{I} - \mathcal{H}_0)(|\psi\rangle - |\psi_0\rangle) = (z\mathbb{I} - \mathcal{H}_0)\delta|\psi\rangle - V|\psi\rangle. \quad (3-41)$$

Multiplying by $G_0(z) = (z\mathbb{I} - \mathcal{H}_0)^{-1}$ yields the Lippmann-Schwinger equation:

$$|\psi\rangle = |\psi_0\rangle + G_0(z)V|\psi\rangle, \quad (3-42)$$

which illustrates the connection between the wave function of the perturbed system and that of the unperturbed one. By iteratively inserting the wave function expression into itself, we obtain the series

$$|\psi\rangle = |\psi_0\rangle + G_0V|\psi_0\rangle + G_0VG_0V|\psi_0\rangle + \dots. \quad (3-43)$$

This is the Born series. Using the T-matrix, one finds

$$|\psi\rangle = |\psi_0\rangle + G_0(z)T(z)|\psi_0\rangle, \quad (3-44)$$

which allows the association

$$\delta|\psi\rangle = G(z)V|\psi\rangle = G_0(z)T(z)|\psi_0\rangle. \quad (3-45)$$

3.4.1.3. Physical observables through the Green function

For a system of fermionic particles, the statistical average of a physical observable A is given by

$$\langle A \rangle = \sum_n f(E_n) \langle n | A | n \rangle, \quad (3-46)$$

where A is the corresponding Hermitian operator and the Fermi-Dirac distribution $f(E)$ is

$$f(E) = \frac{1}{e^{\beta(E-\mu)} + 1}, \quad (3-47)$$

with $\beta = 1/k_B T$, k_B the Boltzmann constant, T the system's temperature, and μ the chemical potential. By forming the expression

$$f(z)\text{Tr}[AG(z)] = \sum_n \frac{f(z)\langle n|A|n\rangle}{z - E_n}, \quad (3-48)$$

where $\text{Tr}[AG(z)]$ denotes the trace of an operator, and applying Cauchy's theorem, one obtains

$$\langle A \rangle = -\frac{1}{\pi} \lim_{\eta \rightarrow 0} \int dE f(E) \text{Im} [AG^-(E)]. \quad (3-49)$$

The density of states can be obtained by taking the trace of the Green function:

$$n(E) = \mp \frac{1}{\pi} \text{Im Tr } G^\pm(E), \quad (3-50)$$

where G^\pm stands for the advanced/retarded Green function.

3.4.2. Voronoi construction in the full potential method

Before addressing how the Green functions are obtained in the KKR formalism, we discuss space decomposition when simulating materials. In KKR, the space is decomposed into atomic cells centered at the nuclei. They are found by a Voronoi construction, which assigns each point of space to a given atomic cell. The aim of this space decomposition is to separate the calculation of the Green function of the crystal into two parts. First, one considers a set of local problems defined within each single atomic cell (see section. 3.4.4), which can be solved independently. Second, one connects the solutions of all atomic problems to obtain the full Green function of the crystal (see section. 3.4.5).

Within KKR, there are two distinct methods for handling the geometry. First, the Atomic Sphere Approximation (ASA), assumes each cell as a sphere with a spherically symmetric potential, thus overlooking any region between cells. Second, the full potential method does not simplify the potential's shape and accurately portrays the gaps between atoms. Due to the cell construction, the spatial coordinates of the KKR Green function are centered around the corresponding sites i and j at \mathbf{R}_i and \mathbf{R}_j , respectively as illustrated in Fig. 3-1.

$$G(\mathbf{x}, \mathbf{x}', E) = G(\mathbf{r} + \mathbf{R}_i, \mathbf{r}' + \mathbf{R}_j; E) = G_{ij}(\mathbf{r}, \mathbf{r}', E). \quad (3-51)$$

Using this separation, the Green function can be split into an on-site contribution and a structural contribution accounting for the multiple scattering,

KKR Green function

$$G_{ij}(\mathbf{r}, \mathbf{r}', E) = G_{ij}^{single}(\mathbf{r}, \mathbf{r}', E)\delta_{ij} + G_{ij}^{structure}(\mathbf{r}, \mathbf{r}', E). \quad (3-52)$$

With the Voronoi construction, the potential of a site i is solely defined within the volume

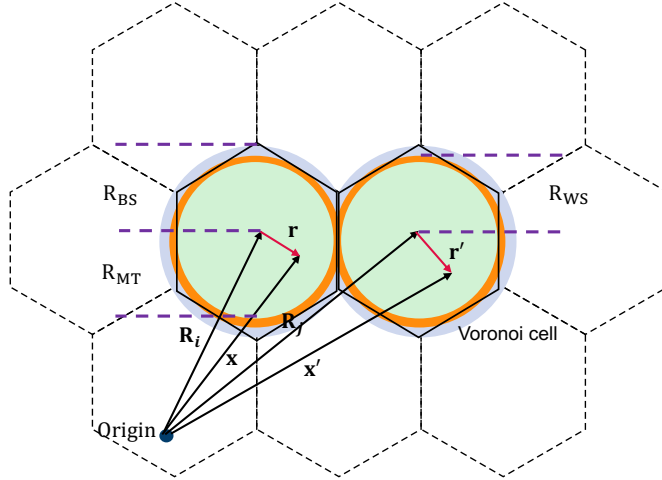


Figure 3-1.: **Illustration of the Voronoi construction for a hexagonal unit cell.** The Voronoi cell of site i is centered at \mathbf{R}_i defining a local frame $\mathbf{x} = \mathbf{r} + \mathbf{R}_i$. Each cell has an associated muffin tin radius R_{MT} , which is defined by the largest sphere fitting completely inside the Wigner-Seitz cell, a Wigner-Seitz radius R_{WS} , which defines a sphere having the same volume as the Wigner-Seitz cell, and the radius of the bounding sphere R_{BS} , which is the smallest sphere enclosing the full Wigner-Seitz cell. .

ν_i of the respective cell:

$$V_i(\mathbf{r}) = \begin{cases} V_i(\mathbf{r}), & \text{if } \mathbf{r} \in \nu_i \\ 0, & \text{else} \end{cases} \quad (3-53)$$

This leads to the definition of the so-called shape function $\Theta_i(\mathbf{r})$:

$$\Theta_i(\mathbf{r}) = \begin{cases} 1, & \text{if } \mathbf{r} \in \nu_i \\ 0, & \text{else} \end{cases} \quad (3-54)$$

The potential of each site i is considered in the local frames and expanded in real spherical harmonics:

$$V_i(\mathbf{r})\Theta_i(\mathbf{r}) = \sum_L V_L(r)Y_L(\hat{r}), \quad (3-55)$$

where $L = l, m$ is the combined angular index, $r = |\mathbf{r}|$ is the absolute distance, and $\hat{r} = \frac{\mathbf{r}}{r}$

represents the unit direction. In this notation, $V_L(r)$ is intertwined with the shape function,

$$V_L(r) = \sum_{L'L''} C_{LL'L''} V_L^0(r) \Theta_{L''}(r), \quad (3-56)$$

with the Gaunt coefficient $C_{LL'L''}$ given by

$$C_{LL'L''} = \int d\hat{r} Y_L(\hat{r}) Y_{L'}(\hat{r}) Y_{L''}(\hat{r}), \quad (3-57)$$

where $V_L^0(r)$ is the expansion of the potential in spherical harmonics without considering any spatial constraints and $\Theta_L(r)$ denotes the expansion coefficient of the shape function. In full potential, the radial argument \mathbf{r} is defined up to the radius of the bounding sphere, which is the smallest sphere enclosing the full Wigner-Seitz cell as illustrated in Fig. 3-1. In the following, the Green function formalism is utilized to solve the Schrödinger equation for the single site scattering starting from the free electron gas.

3.4.3. Free electron gas

As an introduction to the scattering problem, we address the scattering at a single spherical atomic site embedded in free space. Here, the system of free space serves as a reference system for which the Green function satisfies the equation:

$$[\nabla^2 + E]g(\mathbf{r}, \mathbf{r}'; E) = \delta(\mathbf{r} - \mathbf{r}'). \quad (3-58)$$

Its momentum representation is:

$$[-k^2 + E]g(k; E) = 1, \quad (3-59)$$

which readily gives the solution:

$$g(\mathbf{r}, \mathbf{r}'; E) = \int \frac{d^3k}{(2\pi)^3} \frac{e^{ik \cdot (\mathbf{r} - \mathbf{r}')}}{E - k^2}. \quad (3-60)$$

If we integrate the right-hand side of this equation, we get the Green function of a free-electron system:

$$g(\mathbf{r}, \mathbf{r}') = g(\mathbf{r} - \mathbf{r}') = -\frac{e^{i\sqrt{E}|\mathbf{r} - \mathbf{r}'|}}{4\pi|\mathbf{r} - \mathbf{r}'|}. \quad (3-61)$$

Partial wave expansion of the free space Green function is obtained from the similar expansion of the plane waves:

$$\psi_{\mathbf{k}}(\mathbf{r}) = e^{-k \cdot \mathbf{r}} = 4\pi \sum_L i^l j_l(kr) Y_L(\hat{r}) Y_L(\hat{\mathbf{k}}), \quad (3-62)$$

which leads to:

Free electron Green function

$$g(\mathbf{r}, \mathbf{r}'; E) = \sum_L Y_L(\hat{r}) g_l(r, r'; E) Y_L(\hat{r}'), \quad (3-63)$$

where

$$g_l(r, r'; E) = -i\sqrt{E} \sum_l j_l(r_{<}; E) h_l(r_{>}; E), \quad (3-64)$$

and $h_l = j_l + n_l$ are spherical Hankel functions, n_l are spherical Neumann functions, and $r_{<}$ and $r_{>}$ are the smaller and bigger of the radii r and r' respectively.

3.4.4. Single site scattering

In this section, we consider the presence of a potential V that scatters the electronic waves. The Schrödinger equation is solved in order to obtain the electronic wave function $\psi_{\mathbf{k}}$. An ansatz for the latter can be inspired from Eq. 3-62:

$$\Psi_{\mathbf{k}}(\mathbf{r}) = \sum_L 4\pi i^l Y_L(\hat{\mathbf{k}}) R_L(\mathbf{r}; E). \quad (3-65)$$

Here, $R_L(\mathbf{r}; E)$ represents the regular solution of the Schrödinger equation in the presence of the potential, otherwise, it would be simply the Bessel function. In a spherical harmonics basis, it is expressed as

$$R_L(\mathbf{r}; E) = \sum_{L'} \frac{1}{r} R_{LL'}(r; E) Y_{L'}(\hat{r}). \quad (3-66)$$

It generally relies on the angular index L , representing the partial wave component of the initial free-electron plane wave, and another index L' that describes the spatial shape adopted by the partial wave during scattering by a non-spherical potential. By substituting Eqs. 3-62, and 3-65 in the Lippmann-Schwinger equation that provides a recursive solution for the wave function of the full system, $H = H_0 + V$, using the Green function of the unperturbed system $G_0(\mathbf{r}; E)$,

$$\psi(\mathbf{r}; E) = \psi_0(\mathbf{r}; E) + \int d\mathbf{r}' G_0(\mathbf{r}; \mathbf{r}'; E) V(\mathbf{r}') \psi(\mathbf{r}'; E).$$

leads to:

$$R_{LL'}(r; E) = r j_l(\sqrt{E}r) \delta_{LL'} + \int dr' g_l(r, r'; E) \sum_{L''} V_{LL''}(r') R_{LL''}(r'; E). \quad (3-67)$$

For the matrix elements of the non-spherical potential with two spherical harmonics, we have

$$V(\mathbf{r}) = \sum_{LL'} Y_L(\hat{r}) V_{LL'}(r) Y_{L'}(\hat{r}), \quad (3-68)$$

where

$$V_{LL'}(r) = \sum_{L''} C_{LL'L''} V_{L''}(r).$$

Moreover, besides the regular solution, we need a few other basis functions to construct the single Green function. The first such function is the irregular solution based on the Hankel functions, labeled as $S_{L'L}(r; E)$. Given that the Schrödinger equation is a set of interlinked second-order linear differential equations, right and left solutions are possible if the potential is not diagonal in spin space. While, we previously discussed the right solutions, here we list the left solutions, known as $R_{L'L}^*$ and $S_{L'L}^*$ for the regular and irregular solutions respectively:

$$S_{L'L}(r; E) = r h_l(\sqrt{E}r) \beta_{L'L} + \int dr' g_L(r, r'; E) \sum_{L''} V_{LL''}(r') S_{L'L''}(r'; E), \quad (3-69)$$

$$R_{L'L}^*(r; E) = r j_l(\sqrt{E}r) \delta_{LL'} + \int dr' \sum_{L''} R_{L'L''}^*(r'; E) V_{L''L}(r') g_l(r', r; E), \quad (3-70)$$

$$S_{L'L}^*(r; E) = \beta_{L'L}^* r h_l(\sqrt{E}r) + \int dr' \sum_{L''} S_{L'L''}^*(r'; E) V_{L''L}(r') g_l(r', r; E), \quad (3-71)$$

with

$$\beta_{L'L} = \delta_{LL'} - \sqrt{E} \int dr' r j_l(\sqrt{E}r') \sum_{L''} V_{LL''}(r') S_{L'L''}(r'; E), \quad (3-72)$$

$$\beta_{L'L}^* = \delta_{LL'} - \sqrt{E} \int dr' \sum_{L''} S_{L'L''}^*(r'; E) V_{L''L}(r') r j_l(\sqrt{E}r'). \quad (3-73)$$

Lastly, using the right and left solutions, the on-site Green function can be derived as,

Single site Green function

$$G_{LL'}^{\text{single}}(\mathbf{r}; \mathbf{r}'; E) = -i\sqrt{E} \sum_{L''} \begin{cases} R_{L''L}(r; E) S_{L''L'}^*(r'; E) & \text{if } r' > r \\ S_{L''L}(r; E) R_{L''L'}^*(r'; E) & \text{if } r > r' \end{cases}. \quad (3-74)$$

3.4.5. Multiple scattering theory

Besides the single site term, the structural component is the second pivotal element of the KKR Green function. This component not only accounts for all the multiple scattering processes but also incorporates the geometric specifics. Revisiting the concept of the free electron gas, we can elaborate the Green function between two distinct sites i and j as:

$$g(\mathbf{r} + \mathbf{R}_i; \mathbf{r}' + \mathbf{R}_j; E) = \sum_{LL'} Y_L(\hat{r}) j_l(\sqrt{E}r) g_{LL'}^{ij}(E) j_{l'}(\sqrt{E}r') Y_{L'}(\hat{r}'). \quad (3-75)$$

The coefficient $g_{LL'}^{ij}(E)$ finds its derivation from the transformation theorem of Hankel functions:

$$g_{LL'}^{ij}(E) = -(1 - \delta_{ij})4\pi i\sqrt{E} \sum_{L''} i^{l-l'+l''} C_{L''LL'} h_{l''}(\sqrt{E}|\mathbf{R}_i - \mathbf{R}_j|) Y_{L''} \frac{(\mathbf{R}_i - \mathbf{R}_j)}{|\mathbf{R}_i - \mathbf{R}_j|}. \quad (3-76)$$

Considering the case of a material with finite potentials, the entire Green function reads

$$G^{ij}(\mathbf{r}; \mathbf{r}'; E) = G_i^{single}(\mathbf{r}; \mathbf{r}'; E) \delta_{ij} + \sum_{LL'} R_L^i(\mathbf{r}; E) G_{LL'}^{ij}(E) R_{L'}^{*j}(\mathbf{r}'; E). \quad (3-77)$$

Thanks to the multiple scattering approach, the Dyson equation Eq. 3-34 is not solved for the full Green function but just for its structural component:

Structural Green function

$$G_{LL'}^{ij}(E) = g_{LL'}^{ij}(E) + \sum_m g_{LL''}^{im}(E) t_{L''L'''}^m(E) G_{L''L'''}^{mj}(E), \quad (3-78)$$

where:

$$t_{LL'}^m(E) = \int d\mathbf{r} r j_l(\sqrt{E}\mathbf{r}) V^m(\mathbf{r}) R_{L'}^m(\mathbf{r}; E), \quad (3-79)$$

which depicts the scattering aligned with site k 's potential. However, the structural Green functions of free electrons tend to decay slowly with distance, thereby increasing the size of the matrices required to solve Eq. 3-78. To address this, a new reference system with repulsive potentials is introduced, which facilitates the exponential decay of the Green function. This approach allows for quicker and smaller matrix inversions [108, 109].

3.4.6. Finite-temperature complex contour integration

In the Green function KKR method, to minimize computational costs, we perform energy integrations as in Eq. 3-48 by dividing the integration interval into two parts:

$$\int_{-\infty}^{E_F} dE = \sum_{\text{core states}} + \int_{E_B}^{E_F} dE. \quad (3-80)$$

Here, E_B is an energy level chosen to be higher than the energies of the core states but lower than those of the valence states. Additionally, we exploit the analytical continuity properties of the Green function by performing the integration via a contour in the complex plane, rather than restricting it to the real axis. This approach enhances the accuracy of the calculation, as the Green function tends to be smoother away from the real axis, and thus requires a moderate number of energy points to perform the integration.

3.4.7. Relativistic corrections

The classical Hamiltonian, as referenced in Eq. 3-2, omits relativistic effects. Contrary to the non-relativistic Schrödinger equation, the Dirac equation is employed to incorporate these effects. The significant distinction between these two equations is the four-dimensional nature of the wavefunction in the Dirac equation, which encompasses a minor and major component besides the two spin components. Through the application of perturbation theory to the non-relativistic limit at the first order, the Dirac equation leads to a modified Hamiltonian. This adjusted Hamiltonian can be utilized for treating relativistic effects within the conventional Schrödinger framework, as illustrated in standard textbooks (e.g., Ref. [110]) or Ref. [111]. Four novel terms emerge from this perturbation: a relativistic adjustment to the kinetic energy and the Darwin term—often grouped under the scalar relativistic approximation, an interaction with a temporal magnetic field (irrelevant for static scenarios), and the spin-orbit coupling (SOC). Notably, the SOC can be obtained from an expansion of the Dirac equation and retaining terms up to $\frac{v^2}{c^2}$, where v is the magnitude of the electron velocity and c is the speed of light:

$$H_{\text{SOI}} = -\frac{\alpha^2}{2} \boldsymbol{\sigma} \cdot (e\mathbf{E}(\mathbf{r}) \times \mathbf{p}). \quad (3-81)$$

$\alpha \sim \frac{1}{137}$ is the fine structure constant. Classically, the SOI can be viewed as an interaction between the electron spin and the magnetic field emerging in its rest frame as a result of its motion in an electric field $\mathbf{E}(\mathbf{r}) = -\frac{1}{e}\nabla V(\mathbf{r})$. For spherically symmetric potentials, Eq. 3-81 can be simplified even further to show explicitly the orbital momentum \mathbf{L} coupled to the spin:

$$H_{\text{SOI}} = \frac{\alpha^2}{2} \boldsymbol{\sigma} \cdot \left(\frac{1}{r} \frac{dV_i(r)}{dr} \mathbf{r} \times \mathbf{p} \right), \quad (3-82)$$

$$= \frac{\alpha^2}{2r} \frac{dV_i(r)}{dr} \boldsymbol{\sigma} \cdot (\mathbf{r} \times \mathbf{p}), \quad (3-83)$$

$$= \lambda(r) \mathbf{L} \cdot \boldsymbol{\sigma}, \quad (3-84)$$

where the prefactor $\lambda(r) = \frac{\alpha^2}{2r} \frac{dV_i(r)}{dr}$. For more details on how this term is implemented in kkr method see Ref. [69].

3.4.8. KKR self-consistent cycle

The flowchart in Figure. 3-2 outlines the steps involved in the KKR self-consistent cycle. The process begins with setting up Voronoi cells and selecting an initial potential. The single-site problem is then solved using Eq. 3-67 and Eq. 3-79, followed by establishing the reference system through Eq. 3-76. The Dyson equation (Eq. 3-78) is solved to obtain the Green function, which is then used to calculate the charge density. A new potential is determined by solving Poisson's equation and including the exchange-correlation potential.

The cycle checks for convergence by comparing the new and old potentials. If convergence is not achieved, the cycle iterates from solving the single-site problem.

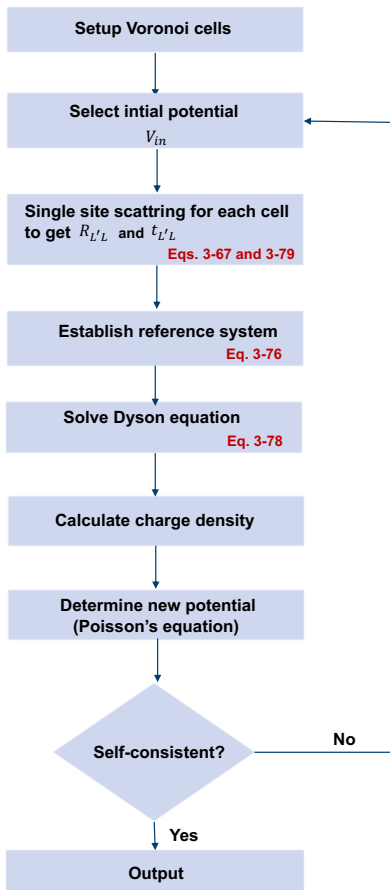


Figure 3-2.: Flowchart outlines the steps involved in the KKR self-consistent cycle.

3.4.9. KKR for extraction of the magnetic interactions

In this section, we introduce a method to derive parameters for the extended Heisenberg model from ab-initio calculations. These parameters reflect the variations in DFT total energy caused by rotating the magnetic moments and can be represented using a spin-dependent perturbative potential in a linear response framework. The KKR Green function approach is particularly suitable for this purpose because it provides direct access to the Green function. We will demonstrate how on-site perturbations quantified by a change δt

in the t -matrix alter the single particle energy. The foundational concept was originally proposed by Lichtenstein et al. [112], who developed a Green function-based formula to directly compute the Heisenberg exchange coupling constant. This was further expanded by Udvardi et al. [113] and Ebert et al. [114], to account for spin-orbit induced interactions such as the DMI.

The method is based on Andersen's magnetic force theorem [115, 116], which approximates the change in total energy upon rotation of the magnetic moments and simplifies it into the alteration of the one-particle energies:

$$\delta E = \int_{-\infty}^{E_F} (E - E_F) \delta n(E) dE = - \int_{-\infty}^{E_F} \delta \mathcal{N}(E) dE, \quad (3-85)$$

where $\mathcal{N}(E)$ is the number of electronic states (integrated density of states) with energy less than or equal to E , and $n(E) = \frac{d\mathcal{N}}{dE}$ is the density of states. $\delta n(E)$ and $\delta \mathcal{N}(E)$ represent the changes due to the rotation of magnetic moments from the reference collinear magnetic state.

Next, Lloyd's formula [117] is used to relate the single-particle energy E_s variation upon the rotation of magnetic moments to the system's T -matrix:

$$E_s = -\frac{1}{\pi} \int_{-\infty}^{E_F} \text{Im Tr} \ln T(E) dE, \quad (3-86)$$

where the inverse of T is given by

$$(\delta T^{-1})_{\alpha\sigma, \beta\sigma'}^{ij} = (\delta t^{-1})_{\alpha\sigma\sigma'}^i \delta_{ij} - G_{ij}^{\alpha\sigma\beta\sigma'}, \quad (3-87)$$

highlighting the connection to the Green function G and single-site t -matrix.

For an infinitesimal rotation of two magnetic moments at sites i and j , the change in energy with respect to an infinitesimal change in the t -matrix is expressed as:

$$\delta E_{ij} = -\frac{1}{\pi} \int \text{Im Tr} [\delta t_i G_{ij} \delta t_j G_{ji}] dE, \quad i \neq j, \quad (3-88)$$

where

$$\delta t_i = (\delta t_i^x, \delta t_i^y, \delta t_i^z) \cdot \delta \mathbf{S}_i. \quad (3-89)$$

Here, $t_i^\alpha(E)$ is the derivative of $t_i(E)$ with respect to \mathbf{S}_i^α ($t_i^\alpha(E) = \frac{\partial t_i(E)}{\partial S_i^\alpha}$) and $\alpha = (x, y, z)$.

Inserting Eq. 3-88 into Eq. 3-89 results in:

$$\delta E_{ij} = -(\delta S_i^x, \delta S_i^y, \delta S_i^z) \begin{pmatrix} \mathcal{J}_{ij}^{xx} & \mathcal{J}_{ij}^{xy} & \mathcal{J}_{ij}^{xz} \\ \mathcal{J}_{ij}^{yx} & \mathcal{J}_{ij}^{yy} & \mathcal{J}_{ij}^{yz} \\ \mathcal{J}_{ij}^{zx} & \mathcal{J}_{ij}^{zy} & \mathcal{J}_{ij}^{zz} \end{pmatrix} \begin{pmatrix} \delta S_j^x \\ \delta S_j^y \\ \delta S_j^z \end{pmatrix}, \quad (3-90)$$

where \mathbf{S}_i is the column unit vector, and the 3×3 matrix \mathcal{J}_{ij} is defined as:

$$(\mathcal{J}_{ij})^{\alpha\beta} = \frac{1}{\pi} \int \text{Im Tr} \left[\delta t_i^\alpha G_{ij} \delta t_j^\beta G_{ji} \right] dE . \quad (3-91)$$

A useful way to represent the Hamiltonian in Eq. 2-12 is through its matrix representation:

$$\mathcal{H} = -\frac{1}{2} \sum_{ij} \mathbf{S}_i^t \mathcal{J}_{ij} \mathbf{S}_j - \sum_i \mathbf{B} \cdot \mathbf{S}_i , \quad (3-92)$$

where the sums run over all atoms in the crystal. Note that the coupling matrix \mathcal{J} is divided into an isotropic, an anti-symmetric, and a traceless symmetric part:

$$\mathcal{J}_{ij} = J_{ij} \mathbb{I} + \mathcal{J}_{ij}^A + \mathcal{J}_{ij}^S , \quad (3-93)$$

where J_{ij} is a scalar determined by $\frac{1}{3} \text{Tr}(\mathcal{J}_{ij})$ and \mathbb{I} the identity matrix and the traceless symmetric part reads

$$\mathcal{J}_{ij}^S = \frac{1}{2} (\mathcal{J}_{ij} + \mathcal{J}_{ij}^T) - J_{ij} \mathbb{I} , \quad (3-94)$$

while the anti-symmetric part is given by

$$\mathcal{J}_{ij}^A = \frac{1}{2} (\mathcal{J}_{ij} - \mathcal{J}_{ij}^T) . \quad (3-95)$$

The anti-symmetric part is related to the Dzyaloshinskii-Moriya vector \mathbf{D}

$$\mathbf{D} = \begin{pmatrix} D_x \\ D_y \\ D_z \end{pmatrix} , \quad (3-96)$$

with

$$\mathcal{J}_{ij}^A = \begin{pmatrix} 0 & D_z & -D_y \\ -D_z & 0 & D_x \\ D_y & -D_x & 0 \end{pmatrix} . \quad (3-97)$$

As discussed before, the method of infinitesimal rotations is used to explore how the system's total energy responds to directional changes in the magnetic moments. The components of the \mathcal{J} tensor that are effectively evaluated or "accessible" through these rotations are those that correlate with changes in direction orthogonal to the original alignment of the magnetic moments. For example, if the magnetic moment points along x ($\mathbf{m} \parallel x$), then we can only access the yz -subblock

$$\mathcal{J} = \begin{pmatrix} ? & ? & ? \\ ? & \mathcal{J}_{ij}^{yy} & \mathcal{J}_{ij}^{yz} \\ ? & \mathcal{J}_{ij}^{zy} & \mathcal{J}_{ij}^{zz} \end{pmatrix} , \quad (3-98)$$

and if the magnetic moment is along y ($m \parallel y$), then we can only access the xz -subblock

$$\mathcal{J} = \begin{pmatrix} \mathcal{J}_{ij}^{xx} & ? & \mathcal{J}_{ij}^{xz} \\ ? & ? & ? \\ \mathcal{J}_{ij}^{zx} & ? & \mathcal{J}_{ij}^{zz} \end{pmatrix}. \quad (3-99)$$

Finally, if the magnetic moment is along z ($m \parallel z$), then we can only access the xy -subblock

$$\mathcal{J} = \begin{pmatrix} \mathcal{J}_{ij}^{xx} & \mathcal{J}_{ij}^{xy} & ? \\ \mathcal{J}_{ij}^{yx} & \mathcal{J}_{ij}^{yy} & ? \\ ? & ? & ? \end{pmatrix}. \quad (3-100)$$

As a final aspect, we address how the magnetic anisotropy energy is extracted from our ab-initio simulations. We provided in Sec. 2.1.3 an introduction to the magnetic anisotropy. Here, we give a general formulation of the magnetic anisotropy in second-order [105]:

$$\mathcal{H}_{\text{Anisotropy}} = \mathbf{S}^T \mathbf{K} \mathbf{S} \quad \text{with} \quad \mathbf{K} = \begin{pmatrix} K_{xx} & K_{xy} & K_{xz} \\ K_{xy} & K_{yy} & K_{yz} \\ K_{xz} & K_{yz} & K_{zz} \end{pmatrix}, \quad (3-101)$$

where \mathbf{K} is a symmetric traceless matrix that has five independent parameters (due to the traceless property). To determine the tensor elements that define the Magnetic Anisotropy Energy (MAE), one must calculate the energy for various orientations of magnetization and analyze the energy differences. For example, the energy difference when the magnetization is aligned along the x and z axes is expressed as:

$$E_x - E_z = K_{zz} - K_{xx}, \quad (3-102)$$

Similarly, aligning the magnetization along the x and y axes yields:

$$E_x - E_y = K_{yy} - K_{xx}. \quad (3-103)$$

If the anisotropy is isotropic in the xy -plane, the MAE matrix simplifies to a diagonal form with a single parameter, K_{zz} . The type of anisotropy—termed easy-axis if $K_{zz} > 0$ and easy-plane if $K_{zz} < 0$ —depends on the sign of K_{zz} as highlighted in Sec. 2.1.3. Thus, the MAE can be represented as:

$$\mathcal{E}_A = K_{zz} \cos^2 \theta, \quad (3-104)$$

where it is evident that K_{xx} and K_{yy} need not be specified.

3.4.10. JuKKR code

The multiple scattering approach described so far is implemented in the JuKKR [68, 69, 71, 118, 119] code developed in Jülich, which we utilized in the current thesis. The software is

capable of incorporating the spin-orbit interaction both within the atomic sphere approximation and the full potential method. The software accurately resolves the Lippmann-Schwinger equation by executing an inversion using Chebyshev polynomials [69]. For solving the single site problem, the code distributes tasks across energies and atoms (Eq. 3-74), which leads to a natural task parallelization. Moreover, it parallelly addresses the multiple scattering problem across energies and k-points (Eq. 3-77). This code uses several parallelization strategies including MPI, OpenMP, and hybrid schemes.

4. Atomistic spin model and machine learning concepts

As discussed in the previous chapter, DFT is a widely used quantum mechanical method for investigating the electronic and magnetic structures of many-body systems. It provides a robust framework for calculating the ground state properties of materials with reasonable accuracy. However, when dealing with large spin systems, such as those involving around a thousand of atoms, the computational cost of DFT becomes very high, making it challenging to determine the ground state properties. Given these limitations, it becomes essential to explore alternative methods for relaxing spin systems that can offer a more computationally feasible approach. One such alternative is the use of atomistic spin relaxation based on the Landau-Lifshitz-Gilbert (LLG) equations. In the previous chapter, we introduced a method to map from DFT the magnetic interactions of an extended Heisenberg model. This provides the key link for a multi-scale modeling approach, where magnetic parameters are obtained from ab-initio and injected into a Heisenberg model to solve the LLG equations. In this thesis, we used this method for different aspects related to the magnetism of two-dimensional vdW materials like spin relaxations to assess energy minima, visualization of the metastable states (skyrmions, merons), and study of the thermal stability of these topological states.

Another fundamental concept related to the magnetism of two-dimensional vdW materials is the spin excitations or magnons. Magnons are crucial in any writing process of magnetic bits and are building blocks of magnonics aiming at coming up with concepts for the storage and transport of information based on the dynamics of spin moments. These spin excitations are typically derived by measuring the dynamical structure factor, $S(q, \omega)$, through inelastic neutron or x-ray scattering techniques. These spectra are then analyzed by comparing the experimental outcomes with theoretical models such as linear spin wave theory in order to fit and identify the underlying magnetic interactions. The whole experimental and fitting procedures are complex and costly. In this context, we used machine learning techniques to approximate the real magnon spectrum and extract the magnetic interactions from noisy experimental spectra enabling significantly lower computational and experimental resources. Ultimately we compare the extracted parameters to those obtained from the KKR-Green function method. In this chapter, we first explore the theoretical foundations of the atomistic spin model. Next, we discuss the basics of the linear spin wave theory used to calculate the magnon spectrum. Finally, we cover the fundamentals of machine learning based on the Kalman Filter enhanced Adversarial Bayesian Optimization (KFABO) algorithm [120, 121].

4.1. Atomistic spin model

After deriving the magnetic interactions of the system from first principles and integrating them into the extended Heisenberg Hamiltonian (Eq. 2-12), the next step is to investigate the magnetic states that can be stabilized by these interactions. To achieve this, we employ a spin relaxation method based on the Landau-Lifshitz-Gilbert (LLG) equation of motion. This section introduces the LLG equation and the Geodesic Nudged Elastic Band (GNEB) method. Specifically, we use the LLG equation to explore metastable magnetic states in materials, while the GNEB method is employed to examine transition mechanisms and the properties of the thermal ensemble of our magnetic states.

4.1.1. Landau-Lifshitz-Gilbert equation

Originally the atomistic spin model proposed by Landau and Lifshitz in 1935 [122] and subsequently refined by Gilbert in 1955 [123], the equation introduces a precession term and a damping term [124] that stems from the quantum mechanical precession of spins and their alignment with an externally applied magnetic field. The atomistic LLG equation is expressed as:

Landau-Lifshitz-Gilbert Equation

$$\frac{d\mathbf{S}_i}{dt} = -\frac{\gamma}{(1+\alpha^2)\mathbf{m}_i}\mathbf{S}_i \times \mathbf{B}_i^{\text{eff}} - \frac{\gamma\alpha}{(1+\alpha^2)\mathbf{m}_i}\mathbf{S}_i \times (\mathbf{S}_i \times \mathbf{B}_i^{\text{eff}}), \quad (4-1)$$

where α represents the Gilbert damping constant, which controls the dissipation of angular momentum and energy from the magnetic subsystem, γ is the gyromagnetic ratio, and $\mathbf{B}_i^{\text{eff}}$ is the effective field related to the energy gradient:

$$\mathbf{B}_i^{\text{eff}} = -\frac{\partial\mathcal{H}}{\partial\mathbf{S}_i}. \quad (4-2)$$

The first term in Eq. 4-1, known as the precessional term, accounts for the moment's precession, which is directed perpendicular to both the direction of the moment and the effective field. This term causes the moment to process on a circular path, indicating that an effective field perpendicular to the spins sets them into precession. The second term, parameterized by α , is referred to as the damping term. It produces a vector that damps the precession of \mathbf{S}_i , ultimately causing it to realign with the effective magnetic field.

Atomistic spin Dynamics (ASD) methods consist of a starting point from the initial spin configuration, e.g., a random configuration, then use an energy minimization algorithm to evolve the spin in time at for example zero temperature until an equilibrium configuration is reached. Once identified, this equilibrium spin configuration is scrutinized. The underlying properties can then be explored by identifying responses to external stimuli, such as the presence of an external magnetic field or the reaction to spin-polarized currents.

4.1.2. Geodesic Nudged Elastic Band (GNEB)

The Geodesic Nudged Elastic Band (GNEB) method [72, 125, 126] is an extension of the traditional nudged elastic band approach, commonly utilized to determine the minimum energy pathway (MEP) between two or more magnetic states (typically local energy minima or metastable states). This is useful to quantify energy barriers between energy minima. In this method, the initial and final states of the system are connected by a path represented through a series of discrete system replicas, known as "images." These images provide a discretized representation of the path, which is initially interpolated between the initial and final states and subsequently refined to an MEP through an iterative optimization algorithm as shown in Fig. 4-1. The arrangement of the images, or the discretization points, is governed by a spring force that operates solely along the path and exclusively between neighboring images [127]. The total force on the i th image, \mathbf{F}_i , can be expressed as:

Force equation

$$\mathbf{F}_i = \mathbf{F}_{i,\text{eff}}^\perp + k(\tau_{i+1} - 2\tau_i + \tau_{i-1}), \quad (4-3)$$

where:

- $\mathbf{F}_{i,\text{eff}}^\perp$ is the component of the effective force on the i th image that is perpendicular to the path.
- k is the spring constant.
- τ_i is the tangent to the path at the i th image.

4.1.3. Spirit code

The Spirit code [72] is a computational tool designed to study and simulate spin dynamics based on the atomistic description of magnetic moments and their interactions. This software evolves a spin system, using for example the LLG equation, over time and drives it towards a minimum of the energy landscape, with various well-established numerical solvers. In our energy minimization simulations, we used the limited-memory Broyden-Fletcher-Goldfarb-Shanno (LBFGS) method, known for significantly accelerating convergence. Moreover, in this code, the aforementioned GNEB framework is utilized for calculating the energy barrier of the metastable state [125, 126].

4.2. Linear Spin Wave Theory

As we discussed in the previous section and Chapter 2, the magnetic ground state can be a collinear state such as FM, AFM, or a noncollinear state like a spiral structure. We also discussed that these spin configurations minimize the energy for systems with competing

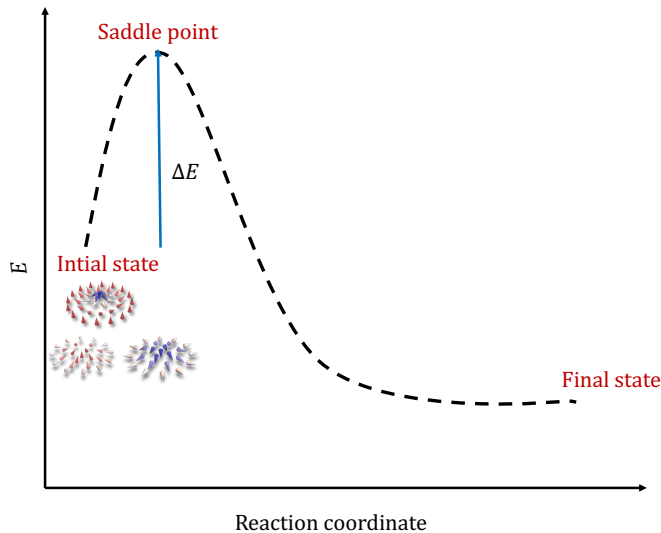


Figure 4-1.: **Minimum energy path of topological defect collapse.** The initial state is the topological state (skyrmion or meron), and the final state is the FM or AFM collinear state. At the saddle point, one can identify the energy barrier ΔE .

interactions, such as the Heisenberg exchange interactions and DMI. However, when we consider small deviations from this magnetic ground state, we introduce spin excitations or magnons. These spin excitations correspond to slight tilts or oscillations of the spins from their equilibrium positions in the ground state structure. Collective spin excitations in two-dimensional (2D) materials are a significant area of research in condensed matter physics, primarily due to their potential applications in quantum computing, spintronics, magnonics, and other advanced technologies. These excitations, commonly known as magnons or spin waves, consist of quantized spin oscillations that travel through a material [128, 129]. One theoretical framework that analyzes these spin excitations is the Linear Spin Wave Theory (LSWT) where the main concept of this theory starts with the Heisenberg Hamiltonian (Eq. 2-12) which describes the ground state. Then, the deviations are quantized using a transformation such as the Holstein-Primakoff transformation as will be discussed in the next section.

4.2.1. Holstein-Primakoff Transformation

The Holstein-Primakoff transformation [130] simplifies the treatment of spin deviations as quantized harmonic oscillators, which expresses spin operators in terms of bosonic creation

and annihilation operators. These operators satisfy the following equations:

$$a|n\rangle = \sqrt{n}|n-1\rangle, \quad (4-4)$$

$$a^+|n\rangle = \sqrt{n+1}|n+1\rangle, \quad (4-5)$$

where a^+ and a follow the bosonic commutation relations:

$$[a_i^+, a_i^+] = [a_i, a_i] = 0, \quad (4-6)$$

$$[a_i, a_j^+] = \delta_{ij}. \quad (4-7)$$

Here, we can treat the occupation number n_i as the spin-deviation operator given by the equation:

$$\hat{n}_i = S_i - S_i^z = a_i^+ a_i. \quad (4-8)$$

The local spin deviation n increases when lowering the spin projection. Note that the eigenvalues of n_i are bounded: $0 \leq n_i \leq 2S$. Thus, the action of S^- can be written as:

$$S^-|n\rangle = \sqrt{(2S-n)(1+n)}|n+1\rangle \quad (4-9)$$

$$= \sqrt{2S} \sqrt{1 - \frac{n}{2S}} \sqrt{1+n}|n+1\rangle. \quad (4-10)$$

The last equation reminds us of how the harmonic-oscillator creation operator acts:

$$a^\dagger|n\rangle = \sqrt{n+1}|n+1\rangle, \quad (4-11)$$

where n is the number of energy quanta in the state $|n\rangle$. Thus, we can relate the circular components of the spin operator to the harmonic-oscillator creation and annihilation operators:

$$S_i^- = \sqrt{2S} a_i^\dagger \hat{f}_i, \quad S_i^+ = \sqrt{2S} \hat{f}_i a_i, \quad S_i^z = S - \hat{n}_i, \quad (4-12)$$

where $\hat{n}_i = a_i^\dagger a_i$. This is the so-called Holstein-Primakoff transformation. \hat{f}_i is a nonlinear operator defined by:

$$\hat{f}_i = \sqrt{1 - \frac{\hat{n}_i}{2S}}, \quad (4-13)$$

which is only well-defined if $n_i \leq 2S$ implying that Eq. 4-12 is not truly compatible with the harmonic oscillator that has a bounded spectrum of \hat{n}_i . Nevertheless, we expect that at low temperatures very few spin deviations occur, such that the statistical average of \hat{n} is small and

$$\frac{\hat{n}}{2S} \ll 1. \quad (4-14)$$

In this case, we can assume $f = 1$, which linearizes Eq. 4-12.

4.2.2. Bogoliubov Transformation

To diagonalize the Hamiltonian, we first transform the bosonic operators into momentum space using a Fourier transformation:

$$\begin{aligned} a_i &= \frac{1}{\sqrt{N}} \sum_{\mathbf{q}} a_{\mathbf{q}} e^{-i\mathbf{q}\cdot\mathbf{r}_i}, \\ a_i^\dagger &= \frac{1}{\sqrt{N}} \sum_{\mathbf{q}} a_{\mathbf{q}}^\dagger e^{i\mathbf{q}\cdot\mathbf{r}_i}. \end{aligned} \quad (4-15)$$

Here, \mathbf{q} is the wavevector, and N is the number of lattice sites. However, the Hamiltonian in momentum space will generally contain terms like $a_{\mathbf{q}}^\dagger a_{\mathbf{q}}$, $a_{-\mathbf{q}} a_{\mathbf{q}}$, $a_{\mathbf{q}}^\dagger a_{-\mathbf{q}}^\dagger$, and $a_{\mathbf{q}} a_{\mathbf{q}}$. Then we use the Bogoliubov transformation [131]:

$$\begin{aligned} a_{\mathbf{q}} &= u_{\mathbf{q}} \alpha_{\mathbf{q}} + v_{\mathbf{q}} \alpha_{-\mathbf{q}}^\dagger, \\ a_{\mathbf{q}}^\dagger &= u_{\mathbf{q}} \alpha_{\mathbf{q}}^\dagger + v_{\mathbf{q}} \alpha_{-\mathbf{q}}, \end{aligned} \quad (4-16)$$

where $\alpha_{\mathbf{q}}$ and $\alpha_{\mathbf{q}}^\dagger$ are new bosonic operators, and the coefficients $u_{\mathbf{q}}$ and $v_{\mathbf{q}}$ are chosen to satisfy the commutation relations and to diagonalize the Hamiltonian. This yields the diagonal form:

$$\mathcal{H} = E_0 + \sum_{\mathbf{q}} \omega_{\mathbf{q}} \left(\alpha_{\mathbf{q}}^\dagger \alpha_{\mathbf{q}} + \frac{1}{2} \right), \quad (4-17)$$

The spin wave spectrum $\omega_{\mathbf{q}}$ provides crucial insights into the magnetic properties of the material. It determines the energy and momentum of the collective excitations (magnons) in the system. The shape of the dispersion relation $\omega_{\mathbf{q}}$ depends on the nature of the exchange interactions and the geometry of the lattice [132].

4.2.3. SpinW code

SpinW is a comprehensive computational package designed for studying spin waves in magnetic materials, it provides an extensive set of tools for modeling and simulating spin wave spectra [133]. The package is implemented in MATLAB, making it accessible to a wide range of users familiar with this platform. SpinW supports various magnetic structures, including ferromagnets, antiferromagnets, and complex magnetic lattices, making it versatile for numerous research applications. The software offers features for defining magnetic Hamiltonians, performing linear spin wave theory calculations, and visualizing results, including dispersion relations and magnon interactions.

4.3. Machine learning techniques

In the previous section, we mentioned that the magnon spectra can be extracted experimentally with Inelastic Neutron Scattering (INS) [134, 135]. The experimental procedure, which

also involves heavy data processing and analysis, is complex, tedious, time-consuming, and expensive. In this thesis, we introduce a machine learning algorithm that integrates active learning sampling with Linear spin wave theory leading to Kalman Filter enhanced Adversarial Bayesian optimization algorithm for approximating the real magnon spectrum using the minimum number of sampling points. In this section, we explain the fundamental concepts of our algorithm starting from the Bayesian Optimization (BO) scheme.

4.3.1. Bayesian optimization

Bayesian Optimization (BO) [136] is a highly effective method for optimizing complex, high-dimensional, and costly-to-evaluate functions. It uses probabilistic models to make smart decisions about where to sample next, significantly reducing the number of function evaluations needed compared to traditional methods. Central to this approach are surrogate models and acquisition functions, which work together to efficiently guide the optimization process.

4.3.1.1. Surrogate models

At the core of Bayesian optimization are surrogate models [137, 138], which approximate the true objective function that is often expensive or time-consuming to evaluate directly. These models predict the function's output and provide an estimate of uncertainty for these predictions, incorporating both predictions and associated uncertainties. This dual capability allows the model to balance exploration (sampling in areas with high uncertainty) and exploitation (sampling in areas expected to have the best values). Gaussian Processes (GPs) are the most widely used surrogate models due to their flexibility and ability to provide a full probabilistic description of the function. The main equation of a Gaussian Process for the predictive distribution of the function values f_* at new points \mathbf{x}_* given observations \mathbf{x} and \mathbf{y} is:

$$f_* | \mathbf{x}, \mathbf{y}, \mathbf{x}_* \sim \mathcal{N}(\mu_*, \Sigma_*), \quad (4-18)$$

where the mean μ_* and covariance Σ_* are given by [139]:

$$\mu_* = \mathbf{K}_*^T (\mathbf{K} + \sigma_n^2 \mathbf{I})^{-1} \mathbf{y}, \quad (4-19)$$

$$\Sigma_* = \mathbf{K}_{**} - \mathbf{K}_*^T (\mathbf{K} + \sigma_n^2 \mathbf{I})^{-1} \mathbf{K}_*. \quad (4-20)$$

Here:

- \mathbf{K} is the covariance matrix of the training points,
- \mathbf{K}_* is the covariance matrix between the training points and new points,
- \mathbf{K}_{**} is the covariance matrix of the new points,
- σ_n^2 is the noise variance.

4.3.1.2. Acquisition function

Another crucial part of Bayesian optimization is the acquisition function [140, 141], which guides the optimization process by determining the next point to sample based on the surrogate model's predictions. Common acquisition functions include:

- **Expected improvement:** This acquisition function aims to measure the expected improvement over the current best observation. It is defined as [142]:

$$\alpha_{\text{EI}}(x) = \mathbb{E}[\max(0, f(x) - f(x^+))], \quad (4-21)$$

where $f(x^+)$ is the current best observation. This can be further broken down into:

$$\alpha_{\text{EI}}(x) = (\mu(x) - f(x^+))\Phi(Z) + \sigma(x)\phi(Z), \quad (4-22)$$

with

$$Z = \frac{\mu(x) - f(x^+)}{\sigma(x)}, \quad (4-23)$$

where:

- $\mu(x)$ is the mean prediction at point x ,
 - $\sigma(x)$ is the standard deviation at point x ,
 - $\Phi(Z)$ is the cumulative distribution function of the standard normal distribution,
 - $\phi(Z)$ is the probability density function of the standard normal distribution.
- **Probability of improvement:** This acquisition function focuses on the probability that a given point x will improve upon the current best observation. It is defined as:

$$\alpha_{\text{PI}}(x) = \Phi\left(\frac{\mu(x) - f(x^+)}{\sigma(x)}\right), \quad (4-24)$$

where:

- $\mu(x)$ is the mean prediction at point x ,
 - $\sigma(x)$ is the standard deviation at point x ,
 - Φ is the cumulative distribution function of the standard normal distribution.
- **Upper Confidence Bound:** This acquisition function uses a balance between the mean prediction and the uncertainty (exploration term). It is defined as:

$$\alpha_{\text{UCB}}(x) = \mu(x) + \kappa\sigma(x), \quad (4-25)$$

where κ is a parameter that controls the trade-off between exploration and exploitation. A higher κ encourages more exploration, while a lower κ focuses on exploitation.

The choice of a surrogate model impacts the efficiency and accuracy of the optimization process, influencing how well the model approximates the true function and how it guides the selection of new points to sample. By iteratively updating the surrogate model with new data and optimizing the acquisition function, Bayesian Optimization efficiently finds the global optimum of the target function with a minimal number of evaluations.

4.3.2. Trust region Bayesian optimization

Although Bayesian optimization is highly effective for optimizing expensive functions, it has some notable drawbacks. One major limitation is its performance in high-dimensional spaces, where the surrogate model's predictions can become less accurate, leading to inefficient exploration and exploitation. Additionally, BO can struggle with highly non-stationary functions, where the function's characteristics change significantly across different regions of the input space. These challenges can result in slower convergence and suboptimal solutions. To address these issues, Trust Region Bayesian Optimization (TuRBO) has been developed [143–145]. TuRBO enhances the robustness and efficiency of BO by using a local probabilistic approach. It constrains the search space to local regions, known as trust regions, and adaptively manages these regions based on the optimization progress. The core idea of TuRBO is to maintain a collection of local models, each operating within its own trust region. The optimization process is guided by a multi-armed bandit strategy, which allocates samples to different local models based on their performance. Specifically, the trust region for each local model i is adjusted using:

$$\Delta_i = \min \left(\Delta_i, \frac{I_i}{\hat{I}_i} \right), \quad (4-26)$$

where Δ_i is the trust region size, I_i is the observed improvement, and \hat{I}_i is the predicted improvement. TuRBO uses Thompson Sampling to select the next point to sample within the trust regions. The strategy for updating the trust regions involves:

- Expanding the trust region if the improvement ratio is above a threshold:

$$\Delta_i \leftarrow \gamma_{\text{increase}} \Delta_i \quad \text{if} \quad \frac{I_i}{\hat{I}_i} > \tau_{\text{increase}}. \quad (4-27)$$

- Shrinking the trust region if the improvement ratio is below a threshold:

$$\Delta_i \leftarrow \gamma_{\text{decrease}} \Delta_i \quad \text{if} \quad \frac{I_i}{\hat{I}_i} < \tau_{\text{decrease}}. \quad (4-28)$$

This approach ensures more accurate surrogate model predictions and more reliable acquisition function optimization, ultimately leading to faster and more effective convergence to the global optimum. By focusing the optimization process within these trust regions, TuRBO

improves both the exploration and exploitation phases of BO, making it more effective in high-dimensional and non-stationary settings.

4.3.3. Adversarial Bayesian optimization with Kalman filter (KFABO)

In this section, we combine active learning sampling, and adaptive noise reduction to form the Kalman Filter enhanced Adversarial Bayesian Optimization Algorithm (KFABO). This algorithm integrates two coupled Bayesian Optimization (BO) algorithms with a Kalman filter. The first BO algorithm, termed fitting BO (fBO), employs trust region Bayesian optimization on our linear response model to search for optimal parameters, aiming to minimize the difference between theoretically predicted and real LSW function values of the measured sample points. The second algorithm, termed sampling BO (sBO), is a standard BO that selects sampling points with maximum information gain relative to the current state, specifically, those points that can better characterize the real LSW function given the current samples and the fitted LSW function. To enhance model fitting performance and mitigate errors due to experimental noise, a Kalman filter is incorporated. This filter infers the noise distribution across the sampling space based on the current state, which contains only partial and potentially unreliable information and reduces sample noise based on this distribution for the subsequent fBO fitting iteration. The mathematical form of KFABO is expressed as:

$$\max_{\text{sBO}} (\min_{\text{fBO}}, (f_{\text{LSW}}(x) - y')) \quad (4-29)$$

where $f_{\text{LSW}}(x)$ denotes the theoretically predicted spin wave intensity of all the measured points x obtained using the LSW function SpinW, and y' is the LSW intensity filtered from the real LSW intensity y of measured points x , where y is obtained either from theoretical simulations (with hidden parameters) or real experimental measurements. The fBO will predict the possible spin wave intensity μ_{LSW} and the relative uncertainties σ_{LSW} using Turbo and it can be expressed as:

$$\mu_{\text{LSW}}, \sigma_{\text{LSW}} = \text{Turbo}(f_{\text{LSW}}(x) - y'). \quad (4-30)$$

The sBO will select the next sampling points that are most likely to contain the most important information about the ground-truth spin waves, based on the current predictions from the fBO and the existing sampling conditions. The mathematical expression of sBO is:

$$x_s = \mathbf{Peak}(\mu_{\text{LSW}}(x) + \text{KI}_{\text{AL}} * \mu_{\text{AL}}), \quad (4-31)$$

where $\text{KI}_{\text{AL}} = \sigma_{\text{LSW}}(\sigma_{\text{AL}} + \sigma_{\text{LSW}})^{-1}$ is the Kalman improvement for AL process, $\mu_{\text{AL}}, \sigma_{\text{AL}} = \mathbb{G}_{\text{AL}}(x, y' - \mu_{\text{LSW}})$ are the mean and variance of the residual between y' and μ_{LSW} predicted by Gaussian \mathbb{G}_{AL} . The **Peak** function is a screening method that filters out the peaks with the highest intensity within a specified cutoff range and sorts the peaks by considering the sample densities within its range. The top 32 points are then selected as the final sample

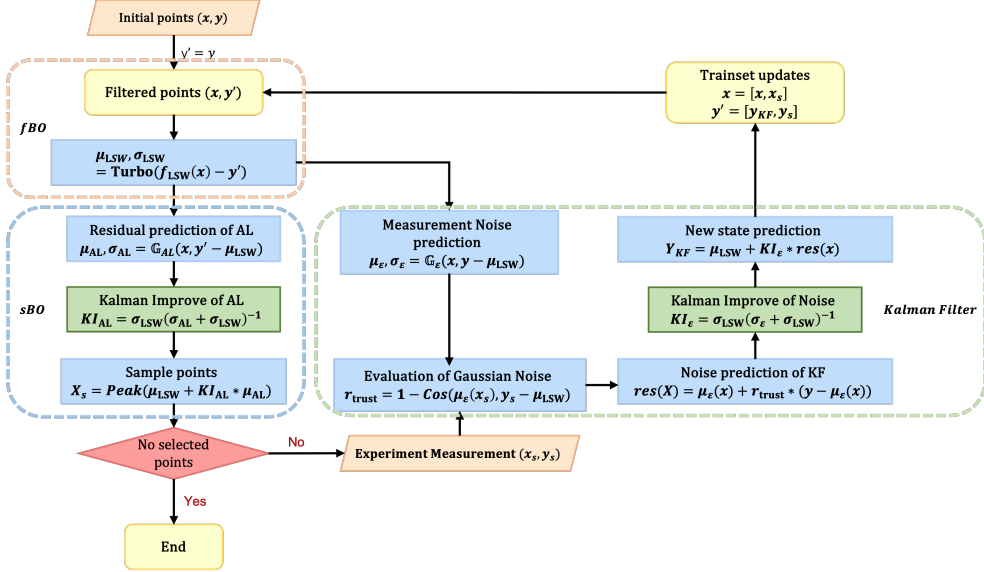


Figure 4-2.: **The KFABO workflow.** The fBO is used to search for optimal parameters of the physical model aiming to minimize the difference between theoretically predicted and measured sample points. The sBO is a standard BO that selects sampling points to better characterize the ground truth given the current samples and the fitted physical model. The Kalman filter infers the noise distribution across the sampling space based on the current state and reduces sample noise based on this distribution for the subsequent fBO fitting iteration.

points x_s . The training set $y' = [y_{KF}, y_s]$ consists of the filtered intensity y_{KF} related to the sample points x from the previous iteration and the newly measured intensity y_s of the newly selected samples x_s . The filtered y_{KF} is defined as:

$$\begin{aligned}
 y_{KF} &= \boldsymbol{\mu}_{LSW}(x) + \text{KI}_\epsilon * \text{res}(x), \\
 \text{KI}_\epsilon &= (\boldsymbol{\sigma}_{LSW}(\boldsymbol{\sigma}_\epsilon + \boldsymbol{\sigma}_{LSW}))^{-1}, \\
 \text{res}(x) &= \boldsymbol{\mu}_\epsilon(x) + r_{\text{trust}} * (y - \boldsymbol{\mu}_\epsilon(x)),
 \end{aligned} \tag{4-32}$$

where KI_ϵ and $\text{res}(x)$ are the Kalman improvement of the noise reduction process and residual used for the Kalman filtering process. Both variables are estimated using $\boldsymbol{\mu}_\epsilon, \boldsymbol{\sigma}_\epsilon = \mathbb{G}_\epsilon(x, y - \boldsymbol{\mu}_{LSW})$, which are the predicted mean and variance of residual between the measurement y and LSW model prediction $\boldsymbol{\mu}_{LSW}$. The $r_{\text{trust}} = 1 - \cos(\boldsymbol{\mu}_\epsilon(x_s), y_s - \boldsymbol{\mu}_{LSW}(x))$ is a ratio to evaluate the trustfulness of the Gaussian \mathbb{G}_ϵ . The KFABO workflow is shown in Fig. 4-2.

5. Magnetoelastic coupling in free-standing 2D CrTe₂ layer

In the realm of two-dimensional (2D) materials research, the identification and detailed examination of new monolayers with distinctive geometric and magnetic properties remain a huge area of study in modern condensed matter science. CrTe₂, particularly in its free-standing monolayer form, presents a compelling case within this context. In this chapter, based on a multiscale modelling approach that combines first-principles calculations and a Heisenberg model supplied with ab-initio parameters, we report a strong magnetoelastic coupling in a free-standing monolayer of CrTe₂. We demonstrate that different crystal structures of a single CrTe₂ layer give rise to non-collinear magnetism through magnetic frustration and the emergence of the Dzyaloshinskii-Moriya interaction. Also, utilizing atomistic spin relaxations, we perform a detailed investigation of the complex magnetic properties pertaining to this 2D material impacted by the presence of various types of charge density waves.

The results discussed in this chapter have been published in Ref. [146].

5.1. Computational details

5.1.1. First-principles calculations

Our simulations utilize first-principles calculations within the framework of density functional theory (DFT). Detailed descriptions of the concepts and methodologies can be found in Chapter 3. Initially, atomic relaxations as a function of various collinear magnetic states of CrTe₂ were obtained using the Quantum Espresso computational package [63–65] with projector augmented plane wave (PAW) pseudopotentials [61, 62] (see Sec.3.3 for more details). In our calculations, the generalized gradient approximation (GGA) of Perdew-Burke-Ernzerhof (PBE) [102] was used as the exchange and correlation functional. The plane-wave energy cut-off is 80 Ry, and the convergence criterion for the total energy is set to 0.1 μeV . We included a vacuum region of 20 \AA in the direction normal to the plane of the monolayer to minimize the interaction between the periodic images. The residual forces on the relaxed atomic positions were smaller than 0.01 eV \AA^{-1} , and the strain on the unit cell was smaller than 0.5 kbar. The self-consistent calculations were performed with a k-mesh of $24 \times 24 \times 1$ points for the unit cell of 1T-phase. The Brillouin zone summations used a Gaussian smearing of 0.01 Ry.

Once the geometries of the various collinear magnetic states were established, we explored in detail magnetic properties and interactions with the all-electron full-potential relativistic

Korringa-Kohn-Rostoker Green function (KKR-GF) method as implemented in the JuKKR computational package [68–71] (see Sec. 3.4 for more details). The angular momentum expansion of the Green function was truncated at $\ell_{\max} = 3$ with a k-mesh of $48 \times 48 \times 1$ points. The energy integrations were performed including a Fermi-Dirac smearing of 502.78 K. The Heisenberg exchange interactions and Dzyaloshinskii–Moriya (DM) vectors were extracted using the infinitesimal rotation method, as elaborated in Sec. 3.4.9, with a finer k-mesh of $200 \times 200 \times 1$. We explored the impact of correcting for strong electronic correlations utilizing the Hubbard parameter U in our DFT calculations. The details of this particular study can be found in Appendix Sec. B.1.

5.1.2. Magnetic interactions and atomistic spin relaxations

Utilizing the mapping scheme described in Sec. 3.4.9 we extract the magnetic interactions that are fed into the the classical Heisenberg Hamiltonian introduced Eq. 2-12 in Sec. 2.2. For convenience, we present once more the considered Hamiltonian:

$$\mathcal{H} = - \sum_i \mathbf{B} \cdot \mathbf{S}_i - \sum_i K_i (S_i^\alpha)^2 - \sum_{i,j} J_{ij} \mathbf{S}_i \cdot \mathbf{S}_j - \sum_{i,j} \mathbf{D}_{ij} \cdot (\mathbf{S}_i \times \mathbf{S}_j). \quad (5-1)$$

The magnetic properties pertaining to CrTe₂ were evaluated by analyzing the Fourier-transformed magnetic interactions, which in reciprocal space gives access to the magnetic ground state and the related dispersion of potential spin spirals (see Eq. 2-42). Furthermore, atomistic spin relaxation simulations using the Landau-Lifshitz-equation (LLG) as implemented in the Spirit code [125, 126] (see detailed description in Sec. 4.1) are performed to validate the predictions and to explore whether more complex magnetic states can arise. In particular, we used the simulated annealing method: we started from a random spin state at 1000 K which we let equilibrate, then cool the system in steps by reducing the temperature to half of its previous value and equilibrating again, until we reach a temperature below 10 K.

5.2. Geometric and magnetic properties

Fig. 5-1 (a-c) shows the three crystal structures (1T, 1T', and CDW) found for the ferromagnetic state of a CrTe₂ monolayer, which differ in the shortest bond arrangements between the Cr atoms. For the 1T phase, the primitive unit cell is a 120° rhombus, while the 1T' phase can be regarded as a distorted structure from the 1T phase, arising from a Peierls-like instability; this is a primary mechanism for the formation of the 1T' phase in transition metal dichalcogenides (TMDs) such as MoS₂ [147] and WTe₂ [148]. The primitive cell of 1T' is a rectangular unit cell, corresponding to a $1 \times \sqrt{3}$ supercell of the 1T phase. Compared to the latter one, two adjacent rows of Cr atoms in the vertical direction move toward each other. Similarly, the CDW structure can be regarded as an alternative distortion of the 1T phase, which was identified and traced to a phonon instability in Ref. [43]. The primitive

cell of CDW is a 30° rotated $\sqrt{3} \times \sqrt{3}$ hexagonal cell with respect to the 1T phase.

The bonds connecting a Cr atom to its neighbors are useful to distinguish between the unveiled structures, and so we define three distances, d_1 , d_2 and d_3 (see Fig. 5-1), which are equal in the 1T phase, two of them are equal in the CDW case ($d_1 = d_2 \neq d_3$), and all different for the 1T' phase. The shortest bonds can be used to visually distinguish the structures, and so are shown in blue in Fig. 5-1. The Cr magnetic moments are about $2.6 \mu_B$ and are listed along with the bond lengths in Table. 5-1.

When imposing an initial AFM state to either 1T or 1T' structures, the geometry changes substantially and we end up with a new phase that we coin 1T'', shown in Fig. 5-1 (d-f), where $d_1 \neq d_2 = d_3$. We also considered more complex AFM arrangements by expanding the 1T'' unit cell to build up the AABB structure where two rows of Cr magnetic moments align parallel (AA) followed by two rows which align anti-parallel to the first two rows (BB), or a zig-zag structure where the parallel magnetic moments are arranged in a zig-zag pattern which is followed by another zig-zag of anti-parallel magnetic moments. The AFM magnetic moments as listed in Table. 5-1 tend to be smaller than the FM ones. Overall, our findings highlight the strong magneto-elastic coupling characterizing the free-standing CrTe₂ monolayer. Imposing different magnetic states leads to large forces and stresses on the unit cell, from which emerge new crystal structures by energy minimization.

Table 5-1.: Lattice parameters, bond lengths, and spin moments of the different CrTe₂ monolayer structures hosting various FM and AFM phases.

Phase	Lattice parameters (Å)					m (μ_B)
	a	b	d_1	d_2	d_3	
1T	3.71	6.42	3.71	3.71	3.71	2.67
1T'	3.71	6.38	3.71	3.47	3.79	2.61
CDW	6.42	6.42	3.73	3.47	3.47	2.64
AABB	3.71	12.27	3.71	3.79	3.39	2.59
1T''	3.73	6.07	3.73	3.47	3.47	2.58
Zig-zag	7.20	6.24	3.60	3.51	3.69	2.56

5.3. Magnetic interactions

We now turn to the analysis of the magnetic properties using the all-electron KKR-GF method. The calculated magnetic interactions are long-ranged and display an oscillatory behavior as a function of distance, as expected on metals, which can lead to energetic competition between different magnetic states and to the stabilization of magnetic spirals (See

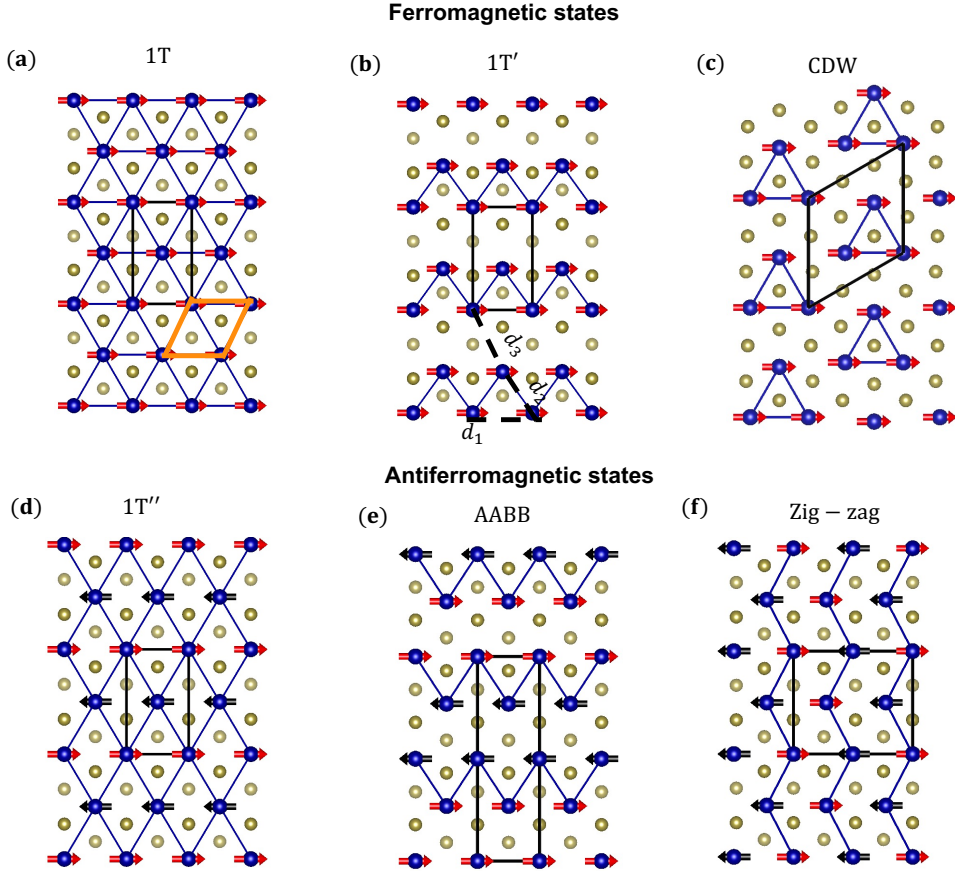


Figure 5-1.: Crystal structures of CrTe_2 monolayer for different assumed magnetic states. (a-c) Crystal structures of FM phases: 1T, 1T', and CDW. 1T' corresponds to a $1 \times \sqrt{3}$ and CDW to a $\sqrt{3} \times \sqrt{3}$ supercell of 1T, respectively. (d-f) Crystal structures of AFM phases: 1T'', AABB, and zig-zag. Cr and Te atoms are in blue and gold colors, respectively. The computational unit cells for the different structures are shown by the black rectangles or rhombi, while the primitive cell for the 1T structure is indicated by the orange rhombus. The different orientations of the magnetic moments are represented by red and black arrows. Blue lines indicate the shortest bonds between the Cr atoms, providing an easy way to visually differentiate the crystal structures.

Sec. 2.1.1). Numerically, we found that the identified ground state is robust once interactions up to a distance of 6 times the nearest-neighbor distance are incorporated in the

simulations. Taking the 1T-phase as an example, if we include only the interactions up to the fourth nearest-neighbor distance we find that the ground state is the non-collinear Néel-AFM state, while taking more interactions into account transforms the ground state into a spin spiral state. The set of Heisenberg exchange and DM interactions up to the fourth nearest neighbors and the magnetic anisotropy are collected in Table 5-2.

The magnetic anisotropy ranging from 1.2 meV to 1.4 meV favors an in-plane orientation of the magnetic moments in agreement with both experimental [40] and theoretical [43] works conducted on the 1T-phase. In all structures, the magnetic anisotropy is uniaxial, except for the 1T phase which has in-plane magnetic anisotropy, and the zig-zag phase which also has a small additional in-plane anisotropy around 0.3 meV. One can see that except for the 1T' and CDW phases, all structures have an AFM first nearest neighbors interaction ($J_1 < 0$) followed by an oscillatory behavior.

Table 5-2.: The Heisenberg exchange coupling (J), the magnitude of the Dzyaloshinskii-Moriya vector ($|\mathbf{D}|$), and magnetic anisotropy energy (K) for the different structures and magnetic phases of the CrTe₂ monolayer. For the DM interaction, — means that the interaction is zero due to inversion symmetry. The correspondence to the bonds in each structure is given in Fig. 5-3.

Phase	K (meV)	J (meV)				$ \mathbf{D} $ (meV)			
		J_1	J_2	J_3	J_4	$ \mathbf{D}_1 $	$ \mathbf{D}_2 $	$ \mathbf{D}_3 $	$ \mathbf{D}_4 $
1T	1.4	-5.4	4.0	2.0	-0.9	—	—	—	—
1T'	1.3	0.6	-2.8	4.4	2.9	—	0.7	0.0	0.2
CDW	1.3	5.7	2.7	-0.4	0.7	1.5	0.2	0.2	0.3
AABB	1.2	-13.6	-4.9	-2.4	5.1	—	0.1	—	0.5
1T''	1.2	-13.0	-0.6	1.2	1.7	—	—	—	—
Zig-zag	1.2	-13.4	-14.9	-7.6	2.1	—	0.2	—	0.3

In Fig. 5-2 we plot the eigenvalues of the Fourier-transformed Heisenberg exchange interactions as a function of reciprocal momentum vector $q = 2\pi/\lambda$ using Eq. 2-19, which serve as proxies for the energy of the magnetic state with the same periodicity. We see that the 1T phase is characterized by energy minima located near the K-point in the first Brillouin zone, which indicates that the ground state is a spiral state (See also Sec. 2.3.2) that can form along the M-K or K- Γ directions with a wavelength $\lambda \approx 3d_1$, where d_1 is the nearest-neighbor distance. Note that the K-point corresponds to the Néel state. The characteristics of this spin-spiraling state will be discussed in detail in the next chapter. The 1T' is ferromagnetic (energy minimum at Γ) while all the AFM structures (1T'', AABB, and zig-zag) host spiral states as ground states (with wavelengths of approximately $8d_1$, $5d_1$, and $8d_1$, respectively).

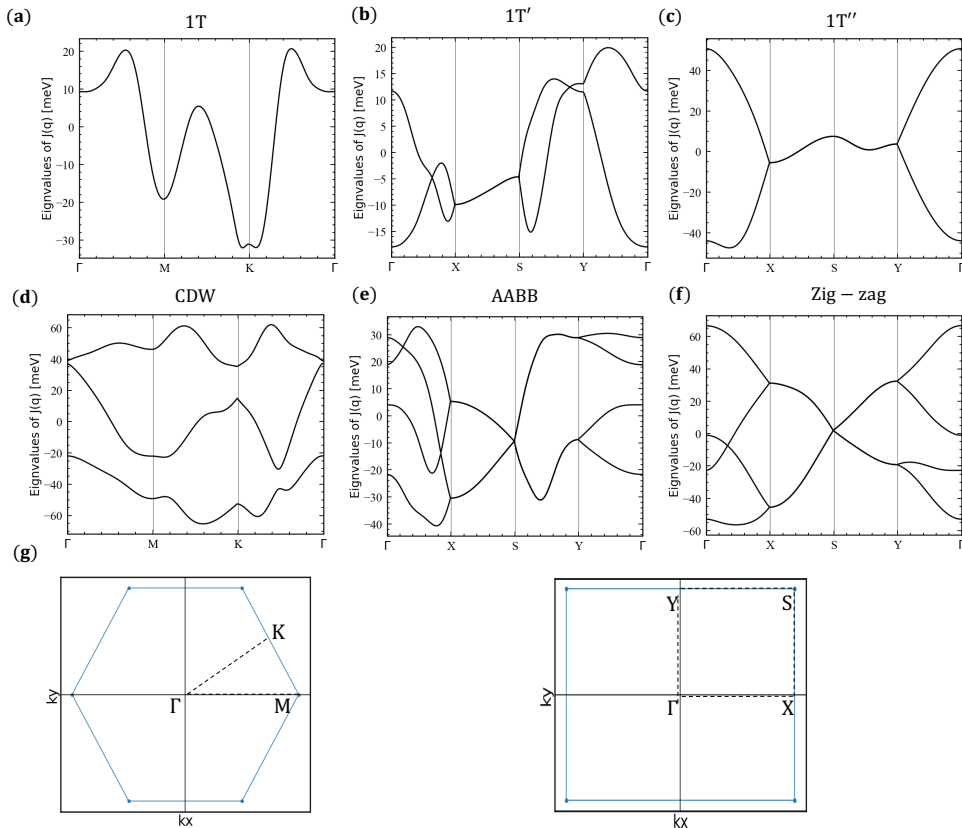


Figure 5-2.: Energetics of magnetic states for the different crystal structures of a CrTe₂ monolayer based on the computed exchange interactions. (a-f) Eigenvalues of the Fourier-transformed exchange interactions as a function of q . (g) The hexagonal first Brillouin zone (left) for the 1T and CDW structures, and the rectangular Brillouin zone (right) for the 1T', 1T'', AABB, zig-zag structures.

We now turn to the discussion of the DMI, which is induced by the combination of the spin-orbit interaction and lack of inversion symmetry (see Sec. 2.1.4 for a detailed introduction.). From our structures, those that lack inversion symmetry are the 1T', CDW, AABB, and zig-zag, with the magnitude of the DM vector for different pairs listed in Table 5-2. As explained in Sec. 2.1.4, the basic properties of the DM vectors follow from the Moriya symmetry rules [21]. As shown in Fig. 5-3, the 1T' structure has an inversion symmetry point between the pairs 0-1, and 0-3, so that the corresponding DM vector vanishes. This does not apply to the other two pairs, so $|\mathbf{D}_2|$ and $|\mathbf{D}_4|$ are finite. Following another of Moriya's symmetry

rules, since the mirror planes (m) are perpendicular to the middle of the bonds between 0-2 pairs, their respective DM vectors lie within the mirror planes. However, the same mirror planes pass through the bonds between 0-4 pairs, so the DMI vector for these pairs is perpendicular to the corresponding mirror plane. Regarding the CDW structure, the DMI is finite for all nearest neighbors. According to the previously mentioned Moriya's symmetry rules, the DMI vector for the first nearest neighbors lies in the mirror plane perpendicular to the middle of the 0-1 bond. The DMI emerging in the AABB structure follows the same rules as in 1T' with higher values for $|\mathbf{D}_2|$ and $|\mathbf{D}_4|$. In the zig-zag structure, the mirror planes are parallel to the middle of the bonds between 0-2 pairs, their respective DM vectors perpendicular to the mirror planes. However, the same mirror planes are perpendicular to the bonds between 0-4 pairs, so the DMI vector for these pairs passes through the mirror planes.

5.4. Atomistic spin relaxation and magnetic ground states

In the previous section, we predicted a spiral state in all structures of the monolayer except 1T' which has a collinear FM state as the ground state. This spiralization of the unveiled magnetic states is governed by the frustration of the Heisenberg exchange interactions. Next we perform atomistic spin relaxation to explicitly visualize the predicted magnetic states and to explore the effect of the two other interactions, the DMI and the magnetic anisotropy.

The results of these simulations are depicted in Fig. 5-4, which reveals that the ground states are qualitatively similar to what was anticipated based on the Heisenberg exchange interactions alone, with the same periodicity as found in the previous section. The impact of the DMI and magnetic anisotropy energy is as follows. As the magnetic anisotropy is of easy-plane type, so its inclusion in the simulations favors the spins to rotate in the plane of the monolayer. For the structures in which it is allowed, the DMI favors a specific sense of rotation of the magnetic moments in a plane perpendicular to the DM vectors. As this plane is typically different from the one favored by magnetic anisotropy, the two interactions compete against each other. For the 1T' structure, the DMI would stabilize a long-period spin spiral state with wavelength $\lambda \approx 100d_1$; however this is energetically unfavorable when the magnetic anisotropy is accounted for, and so the ferromagnetic state remains the ground state, with an in-plane orientation of the spin moments. The competition between the DMI and the magnetic anisotropy is exemplified for the case of the AABB structure. This causes the spins to tilt away from the xy -plane favored by the anisotropy, while leaving the periodicity of the spiral state derived from the isotropic exchange interactions essentially unchanged.

Finally, we compare the total energies of each structure to that of the 1T phase (see Table. 5-3). We consider two contributions: the total energy differences for collinear reference magnetic states, as calculated with the KKR-GF method (Sec. 3.4), and the additional energy lowering from each reference magnetic state to the lowest energy state found by

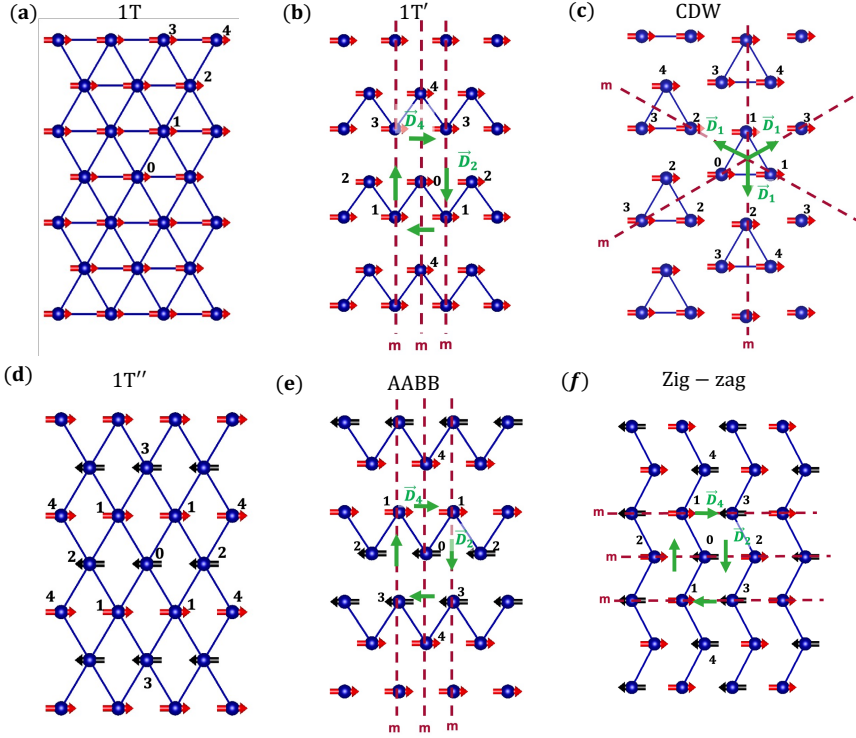


Figure 5-3.: **Dzyaloshinskii-Moriya interactions in CrTe₂.** (a,d) Centrosymmetric structures 1T and 1T'' for which the DMI vanishes. (b-c,e-f) Non-centrosymmetric structures 1T', CDW, AABB, and zig-zag for which the DMI is allowed. The DM vectors are represented by green arrows, and the mirror planes that enforce the corresponding Moriya symmetry rules by dashed lines. The numbers 1 to 4 represent the four nearest neighbors for the reference atom 0, according to increasing bond length.

atomistic spin dynamics using the Spirit code. Overall, the ground state is found to be the non-collinear AFM zig-zag structure.

5.5. Conclusions

In summary, using a combination of density functional theory calculations and atomistic spin dynamics we demonstrated that the monolayer of CrTe₂ can host various structural phases with a rich set of magnetic states. Interestingly, this 2D material hosts strong magneto-elastic coupling phenomena. Imposing various magnetic states drives structural transitions, from

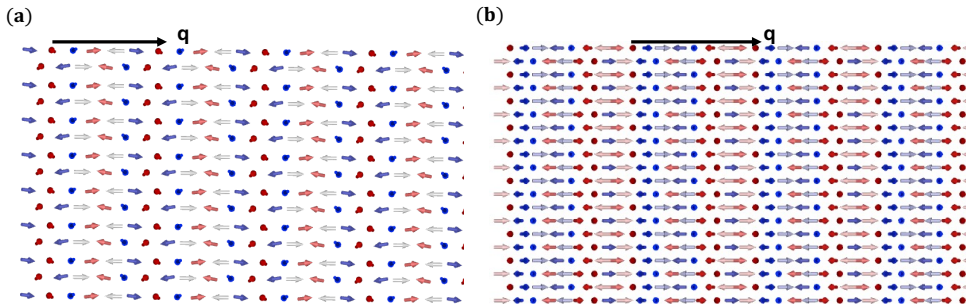


Figure 5-4.: **Spiral states in different structures of a CrTe₂ monolayer.** (a) AABB ($\lambda = 5d_1$); (d) Zig-zag ($\lambda = 8d_1$). The 1T'' case is similar to the AABB but with $\lambda = 8d_1$ and is not shown.

Table 5-3.: Combined magnetic energy lowering for each of the considered crystal structures. ΔE_{DFT} represents the DFT total energy differences between the collinear magnetic states, while ΔE_{Spirit} represents the additional energy lowering found for the non-collinear magnetic states as evaluated via Spirit (spin model). ΔE_{total} gives the combined energy difference ($\Delta E_{\text{DFT}} + \Delta E_{\text{spirit}}$).

Phase	ΔE_{DFT} (meV)	ΔE_{Spirit} (meV)	ΔE_{total} (meV)
1T	0	-45.7	0
1T'	-56.7	-1.3	-12.3
CDW	-61.2	-91.9	-107.4
AABB	-50.5	-58.3	-63.1
1T''	-230.4	-4.6	-189.3
Zig-zag	-241.7	-5.6	-201.3

which emerge new crystal structures with different atomic displacements and deformations of the unit cell. For each of the obtained phases, non-trivial non-collinear magnetic states are obtained, where the physics is driven by long-range competing exchange interactions. The DMI is present in some of the structures, which can drive chiral magnetism, and so we assessed its influence. When constraining our simulations to collinear magnetism, our results are consistent with the DFT calculations reported in Refs. [42, 44], which indicate that a CrTe₂ monolayer has a zig-zag AFM ground state. The CDW structure identified in Ref. [43] is also plausible when restricting the calculations to only ferromagnetic states, and could be stabilized under some experimental conditions. Notably, a noncollinear antiferromagnetic zig-zag order was experimentally detected in Ref. [42] using SP-STM. The external magnetic

field was proposed to cause a spin-flop-like deviation of the collinear zig-zag antiferromagnetic state, thus leading to the contrast change in the SP-STM measurements. However, the corresponding DFT simulations support only a small amount of canting, of the order of 5° for the magnetic field employed in the experiment. A different scenario emerges from our simulations: the noncollinearity is intrinsic and large, with canting angles of about 45° , which arises from the competition between different exchange interactions. We speculate that the observed SP-STM contrast difference when the field is applied can also be explained by the noncollinear zig-zag structure that we found, after accounting for expected differences due to the graphene bilayer and capping, which are not considered in our calculations.

Although the overall ground state is the AFM spin spiral hosted by the zig-zag structure, we found a signature of new topological magnetic objects discussed in the next chapter, also we foresee the rich potential tunability of both the crystal structure and the magnetic states depending on the substrate on which the single CrTe₂ layer is deposited, whether it is strained, or how it is integrated in van der Waals heterostructures or other types of multilayers. This motivates us to pursue the exploration of this intriguing 2D material in these different scenarios as will be discussed in the next chapter.

6. CrTe₂ as a 2D material for topological magnetism in complex heterobilayers

In the previous chapter, we found that the ground state of freestanding CrTe₂ is the zig-zag AFM spiral state. Meanwhile, the 1T phase displays structural instability, as indicated by the phonon dispersion. However, we can stabilize this phase by constructing heterostructures with Te-based layers incorporating other non-magnetic transition metal atoms. The phonon dispersion curves for CrTe₂/TiTe₂ and CrTe₂/NiTe₂ heterobilayers as shown in the phonon dispersion in Fig. 6-1 (c) provide valuable insight into their vibrational properties and stability. For both heterobilayers, the phonon dispersion plot exhibits well-defined acoustic branches starting at zero frequency, indicating good lattice dynamics stability at the interface of these two layers. The absence of negative frequencies along the high-symmetry paths in the Brillouin zone suggests that this heterobilayer is dynamically stable, with no tendency for spontaneous distortion under small perturbations.

In this chapter, we explore systematically heterostructures where we interface CrTe₂ with different Te-based layers incorporating various non-magnetic transition metal atoms. We demonstrate that it is possible to engineer 2D topological magnetism in the 1T phase of CrTe₂ 2D layers as shown in Fig. 6-1 (a,b). We unveil new topological antiferromagnetic (AFM) objects already arising as metastable states in the free-standing 1T phase of CrTe₂. These objects consist of multi-meronic particles emerging in a frustrated in-plane Néel magnetic environment. Such AFM topological states have long been sought in the context of skyrmions as ideal information carriers since they are expected to be unaffected by the skyrmion Hall effect [20, 46–50] responsible for the undesired deflection of conventional skyrmions from a straight trajectory upon application of a current. Their AFM nature should also lead to a weak sensitivity to external magnetic fields and potentially terahertz dynamics [51, 52], further motivating efforts towards their experimental realization. Once interfaced with various Te-based layers containing either heavy or light transition metal atoms, we demonstrate the ability to engineer the stability and nature of the underlying magnetic state. Surprisingly, with the right vdW heterostructure, the AFM merons can be converted to FM skyrmions, which opens unique opportunities for designing devices made of 2D materials to realize fundamental concepts for information technology based on topological magnetic bits.

The results discussed in this chapter, have been previously published in Ref. [149].

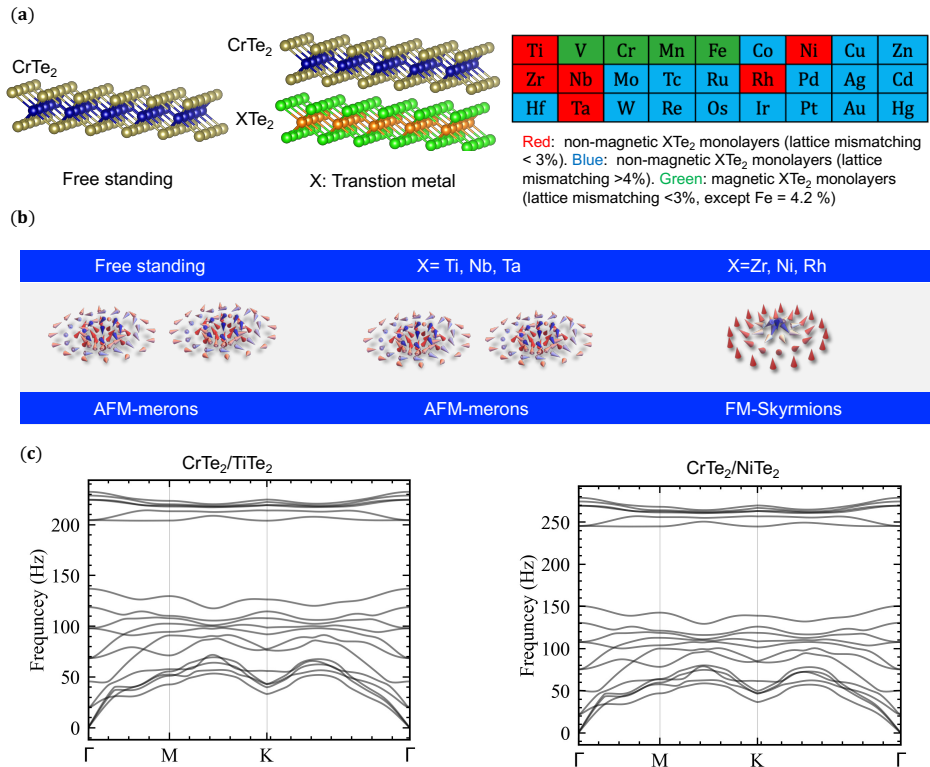


Figure 6-1.: **Overview of the heterostructures and magnetic states.** (a) CrTe₂/XTe₂ heterobilayer, where X is the transition metal from the right table. (b) The topological magnetic states are found in the CrTe₂/XTe₂ heterobilayer, with X being the transition metal in red color. The spin-textures of a meron, antimeron, and skyrmion are illustrated together with the wrapping of the surface of a unit sphere by the underlying magnetic moments, which gives rise to different topological charges. (c) Phonon dispersion curves for CrTe₂/TiTe₂ and CrTe₂/NiTe₂ heterobilayers.

6.1. Computational details

We follow the computational scheme detailed in the previous chapter. Initially, structural relaxations CrTe₂/XTe₂ heterobilayers were obtained using the Quantum Espresso computational package [63–65], with pseudopotentials (PAW), exchange and correlation functional (GGA), and threshold parameters for convergence like the free-standing case with increasing the vacuum to 30 Å. Then, we used the JuKKR computational package [68–71] to extract the magnetic interactions that fit the classical Heisenberg Hamiltonian (see Eq. 2-12) with

angular momentum expansion of the Green function, k-mesh, and Fermi-Dirac smearing like the case of the free-standing case. Finally, atomistic spin relaxation simulations using Spirit code [125, 126] are used to validate the predictions of complex magnetic states with the simulated annealing method.

6.2. New topological AFM magnetic state in monolayer CrTe₂

In the previous chapter, we found that the 1T phase of free-standing CrTe₂ monolayer is characterized by a magnetic moment of $2.67 \mu_B$. The magnetic interactions favor antiferromagnetism, which on a triangular lattice usually leads to the Néel phase in which neighboring magnetic moments have an angle of 120° . It can be partitioned into three FM sublattices named α , β , and γ as shown in Fig. 6-2 (a). However, the Heisenberg exchange interactions are long-ranged and introduce competing tendencies, resulting in a frustrated spin spiraling state with an energy minimum close to the Néel state (Fig. 5-2 (a)). Also, we found that the spin spiral is further modified by the magnetic anisotropy (1.4 meV), which favors an in-plane orientation for the magnetic moment. In the in-plane background magnetization merons discussed in Sec. 2.4.2 can form. What we found, however, is a new topological AFM state made of six merons, which we name hexamer emerging in a frustrated in-plane Néel state. In order to understand the origin of this magnetic phase, we show in Fig. 6-2 (b) that the multi-meronic state arises from various combinations of meronic textures coexisting as pairs (meron-meron, meron-antimeron, and antimeron-antimeron) in each of the three AFM sublattices.

As elaborated in Sec. 2.4.2, the topological charge (t) for a meron is determined by the product $pw/2$, where w is the winding number w , which describes the in-plane rotation of the magnetic moments with $w = +1$ (-1) for vortex (antivortex). The polarity p describes the out-of-plane core magnetization ($p = +1$ for up, and $p = -1$ for down). This leads to a value of $t = -1/2$ ($t = +1/2$) for a meron (antimeron). Various combinations of meronic states can emerge, leading to a rich set of the possible values of the total topological charge T illustrated in Fig. 6-2 (c). The first scenario shown in Fig. 6-2 (c) corresponds to a meronic hexamer with zero total topological charge ($T = 0$), which can arise either when each sublattice accommodates a meron-antimeron pair ($t = 0$), or when hosting pairs of meron-meron pair ($t = 1$), antimeron-antimeron ($t = -1$) and meron-antimeron ($t = 0$). The second and third scenarios have an opposite total topological charge of $+1$ and -1 . The state with $T = 1$ (-1) occurs either when two sublattices have meron-antimeron pairs carrying a charge $t = 0$ and the third sublattice contains an antimeron-antimeron pair of a charge $t = 1$ (meron-meron pair with $t = -1$), or when two sublattices have antimeron-antimeron pairs with $t = 1$ (meron-meron pairs with $t = -1$) while the remaining sublattice host a meron-meron pair of charge $t = -1$ (antimeron-antimeron with $t = 1$).

Having established the existence of AFM meronic objects, we investigate their stability

against thermal excitations utilizing a series of geodesic nudged elastic band (GNEB) simulations. Fig. 6-2 (d) displays the minimum energy path for the collapse of the topological AFM state (more details on the saddle point are shown in Appendix Fig. C-2(a)), which hosts an energy barrier of 7.9 meV. This shows that these magnetic objects are metastable and should exist over a broad range of temperatures.

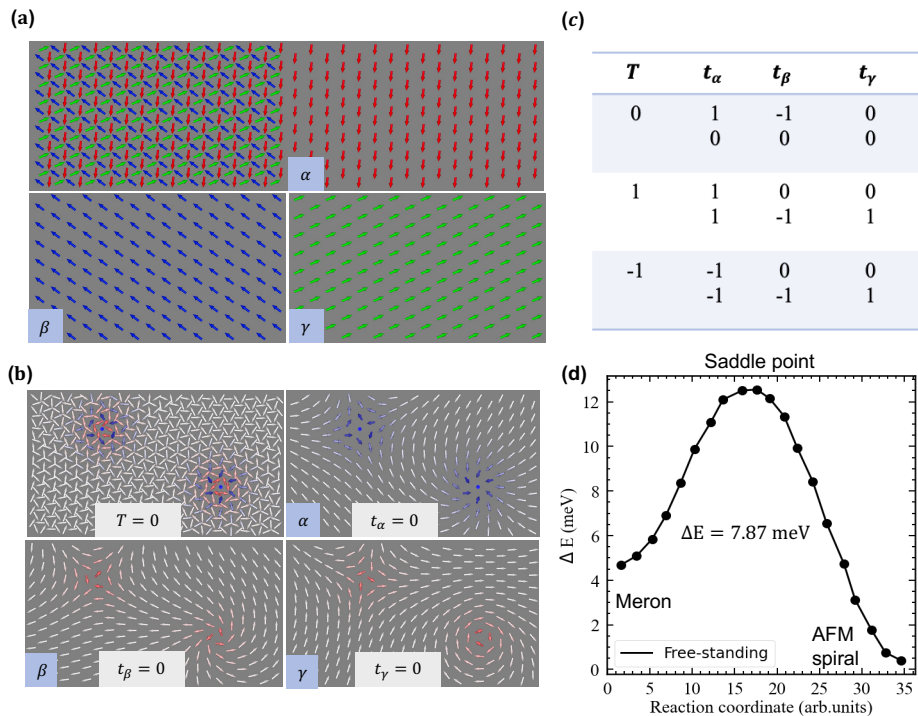


Figure 6-2.: **Magnetic state in the free standing CrTe₂.** (a) Decomposition of the Néel state into three ferromagnetic sublattices α , β , and γ carrying moments rotated by 120° . (b) Frustrated AFM multi-meronic spin-textures. The total topological charge T is decomposed into the three sublattices, each of which hosts a pair of merons with sublattice-dependent topological charges t_i ($i = \alpha, \beta, \gamma$). Here the magnetic background is the spin spiraling ground state, which is very close to the Néel state. (c) Total topological charge T and how it arises from various possible combinations of the topological charges from each sublattice. (d) Energy path for the collapse of the single pair of the AFM meronic state hosted by the free standing CrTe₂ layer.

6.3. Various stacking orders in $\text{CrTe}_2/\text{XTe}_2$ heterobilayers

Motivated by the intriguing magnetic behavior of the single CrTe_2 layer discussed in the previous section, we explore proximity-induced magnetic phases upon interfacing with various XTe_2 monolayers, X being a transition metal atom. Our systematic structural investigation of the different junctions enabled us to categorize them into three groups, as illustrated in Fig. 6-1 (a): The first group hosts non-magnetic XTe_2 layers with a small lattice mismatch (less than 3%) with CrTe_2 such as (Zr, Nb, Rh, Ni, Ti) Te_2 , and this is the group that we focus on our work. The second and third groups were disregarded since they have either a large lattice mismatch (more than 4%) or are magnetic, which would lead to more complex proximity-induced effects to be explored in future studies.

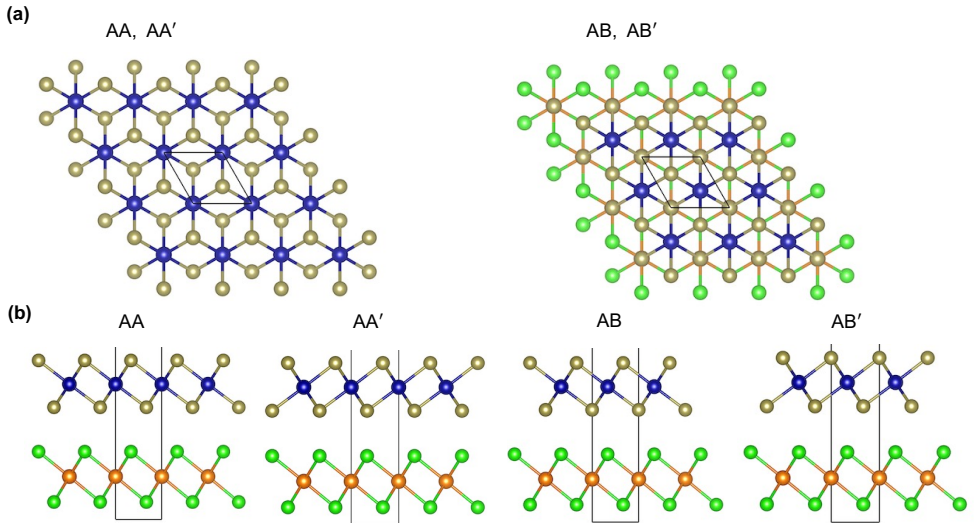


Figure 6-3.: The different AA, AA', AB, and AB' stacking arrangements for $\text{CrTe}_2/\text{XTe}_2$ heterobilayers. (a) Top and (b) side views.

The heterobilayers made of CrTe_2 and nonmagnetic XTe_2 were built assuming four different stacking (AA, AA', AB, and AB') as illustrated in Fig. 6-3. In the AA stacking, which is the ground state (see Table 6-1), Cr is vertically aligned with the transition metal X, and the Te layers forming the interface are shifted with respect to each other, while in the AA' arrangement, they are stacked on top of each other. In the AB and AB' structures, Cr and X are no longer vertically aligned, and the two structures are distinguished by the stacking arrangement of the Te layers at the interface. In the following, we focus our investigation on the AA stacking.

Table 6-2 shows the lattice parameters, including lattice constant and interlayer distance,

Table 6-1.: Total energy difference between various stacking orders and the ground state AA structure for all CrTe₂/XTe₂ heterobilayers. Energies in meV.

Stacking	CrTe ₂ on top of					
	TiTe ₂	NbTe ₂	TaTe ₂	NiTe ₂	ZrTe ₂	RhTe ₂
AA'	105.3	126.9	125.9	149.1	130.1	185.5
AB	30.3	27.3	26.4	103.6	60.5	120.8
AB'	9.9	4.6	8.2	4.8	23.7	61.6

for the AA stacking order. It is clear that these parameters vary significantly depending on the transition metal in the Te-based layers (See Appendix Fig. C-1 for the other stacking orders). The lattice constants can be grouped around two values: ~ 3.7 Å for CrTe₂/(Ti, Nb, Ta)Te₂ heterobilayer, which is close to the lattice constant of the free standing CrTe₂ monolayer, and ~ 3.8 Å in CrTe₂/(Zr, Ni, Rh)Te₂ heterobilayer, which is similar to the value of the bulk CrTe₂ lattice constant and results from the strain created at the interface.

Table 6-2.: Lattice constant a , interlayer distance h in the AA stacking. As a reference, the free-standing CrTe₂ has a lattice constant of 3.71 Å.

	CrTe ₂ on top of					
	TiTe ₂	NbTe ₂	TaTe ₂	NiTe ₂	ZrTe ₂	RhTe ₂
a (Å)	3.73	3.70	3.70	3.81	3.82	3.79
h (Å)	3.76	3.65	3.74	3.46	3.75	3.50

6.4. Topological magnetic states in CrTe₂/XTe₂ heterobilayers

Now we turn to the analysis of the magnetic properties of all heterobilayers in the AA stacking. In the first scenario, where the interfacing Te-based layer contains Ta, Nb, or Ti, the Heisenberg exchange interactions induce a frustrated spin spiraling state with an energy minimum close to the Néel state (Fig. 6-4 (a)). Once interactions induced by the spin-orbit interaction included, AFM multimeronic spin-textures emerge similar to the free-standing case (Fig. 6-4 (b)). Adding the substrate layer breaks the inversion symmetry of the CrTe₂ monolayer and introduces the DMI, where the z -component of the of the DM-vector for the first and second nearest neighbors favors in-plane rotations of the magnetic moments and so is compatible with the underlying in-plane magnetic anisotropy (Table 6-3). This enhances the stability of the AFM topological objects, as can be identified by the increased energy

Table **6-3**: Magnetic anisotropy energies (K) and Dzyaloshinskii-Moriya interaction (D) of the CrTe₂/XTe₂ heterobilayers in the AA stacking. As a reference, the free-standing CrTe₂ has a magnetic anisotropy of 1.40 meV and zero DMI.

CrTe ₂ on top of						
	TiTe ₂	NbTe ₂	TaTe ₂	NiTe ₂	ZrTe ₂	RhTe ₂
K (meV)	0.95	0.90	0.94	0.90	0.61	1.70
$ \mathbf{D}_1 $ (meV)	0.21	0.23	0.27	0.30	0.30	0.45
D_1^z (meV)	0.10	0.15	0.22	0.05	0.06	0.06
$ \mathbf{D}_2 $ (meV)	0.48	0.37	0.48	0.60	0.61	0.71
D_2^z (meV)	0.15	0.18	0.20	0.01	0.01	0.12
$ \mathbf{D}_3 $ (meV)	0.38	0.27	0.30	0.31	0.32	0.35
D_3^z (meV)	0.05	0.05	0.05	0.02	0.02	0.80

barrier illustrated in Fig. 6-4 (c). Therefore, the heterobilayer with the largest z -component of the DMI has the highest energy barrier. The energy barrier for the bilayers with TiTe₂, NbTe₂ and TaTe₂ is 0.2 meV, 0.4 meV and 2.2 meV higher than the one for free-standing CrTe₂, respectively, and the increased stability correlates with the increase in the magnitude of the DM interaction going from Ti to Nb to Ta, as listed in Table 6-3. We note that the MAE is roughly constant for all investigated interfaces (~ 0.9 meV). Interestingly, the radius r of each of the merons and the distance d between them (illustrated in Fig. 6-4 (b)) show opposite trends. The radius increases for the heterobilayers, with values of 2.6 nm (TiTe₂), 2.7 nm (NbTe₂) and 2.8 nm (TaTe₂) larger than the one for the free-standing CrTe₂ (2.4 nm), and follows the increase of the out-of-plane DMI. Conversely, the distance between the two merons is progressively reduced: $d = 34.8$ nm for free-standing CrTe₂ and 34.4, 34.3 and 34.0 nm once it is interfaced with TiTe₂, NbTe₂ and TaTe₂, respectively.

In the second scenario, CrTe₂ is interfaced with Te-based layers hosting either Zr, Ni or Rh. As mentioned before, these layers impose a lattice strain on CrTe₂ that switches the magnetic ground state from AFM to FM based on the Heisenberg exchange interactions (see energy minimum in Fig. 6-4 (f)). Once DMI and MAE are taken into account (see values in Table 6-3), Néel-type skyrmionic domains form in zero magnetic fields as shown in Fig. 6-4 (d). For the calculation of energy barriers, we select isolated skyrmions, resulting in the spin texture shown in Fig. 6-5 (a), revealing that they are metastable. A magnetic field larger than 6 T transforms the skyrmionic domain state to a triangular lattice of skyrmions, Fig. 6-4 (e), which is more stable than the FM state by 3.1, 2.8 and 2.2 meV for the Rh, Ni and Zr-based heterobilayers, respectively. Next, we explore the thermal stability of an isolated skyrmion in a FM background, for which GNEB simulations led to the energy barriers plotted in Fig. 6-5

(a) (more details on the saddle point are shown in Appendix Fig. C-2(b)). The barrier that has to be overcome to allow the skyrmion to relax to the FM state increases going from Ni (6 meV) to Zr (7 meV) to the Rh-based bilayer (8 meV), which decreases with increasing the magnetic field as shown in Fig 6-5(c). In this case the MAE depends more strongly on the nature of the heterobilayer (e.g., it is almost twice as large for Rh than for Ni), and hence has a stronger influence on the energy barrier and also on the skyrmion radius. A larger energy difference between the skyrmion and the FM state corresponds to a larger skyrmion radius, and as expected they all shrink in size when the magnitude of the applied magnetic field is increased (Fig. 6-5 (b)), disappearing above about 30 T. In contrast, applying an external magnetic field to the AFM merons found for the Ti, Nb, and Ta-based heterobilayers has no noticeable effect on their radius, but the underlying total topological charge changes at approximately 12 T from ± 1 to 0 (see Table 6-4 for more details).

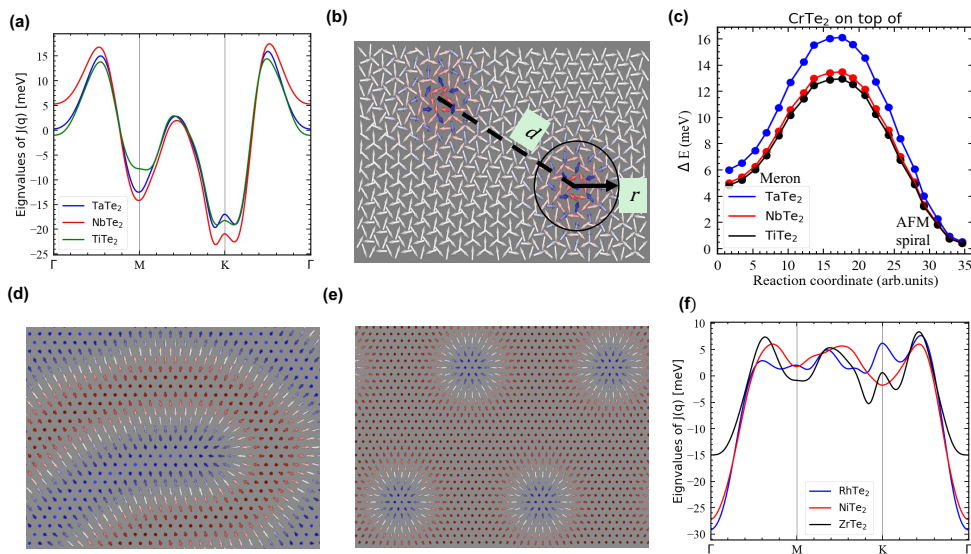


Figure 6-4: **Topological magnetic textures in heterobilayers.** In (a,b,c) and (d,e,f) results related respectively to CrTe₂/(Ti,Nb,Ta)Te₂ and CrTe₂/(Zr, Ni, Rh)Te₂ heterobilayers. (a,f) Eigenvalues of the Fourier-transformed exchange interactions as a function of q . (b) An example of an AFM meronic texture indicating the radius r of each meron and the distance d between the meronic partners. (c) Energy path for the collapse of a single pair of AFM merons in the heterobilayers. (d) Zero-field skyrmionic-like magnetic state in the heterobilayers. (e) Skyrmionic lattice formed upon application of a magnetic field of 6 T.

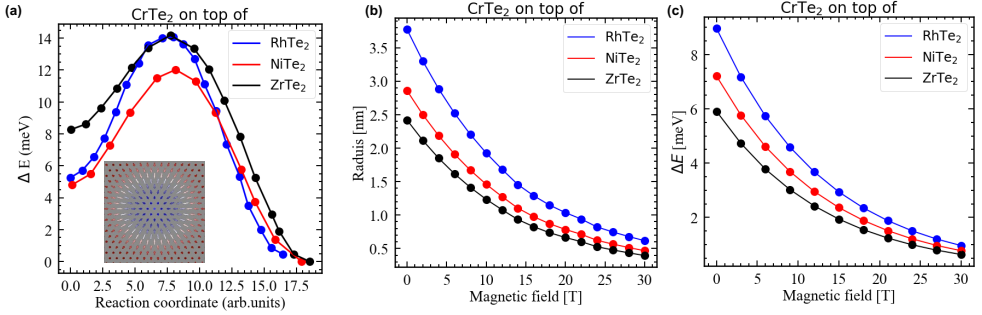


Figure 6-5.: **Single skyrmion in CrTe₂/(Zr, Ni, Rh)Te₂ heterobilayers.** (a) Energy path for the collapse of the single skyrmion. (b,c) The radius of a single skyrmion and energy barriers, obtained with GNEB simulations, as a function of the magnetic field.

Table 6-4.: Effect of the magnetic field on the topological charge of the AFM multi-meronic spin-texture. Shown are the total topological charge T and how it arises from the contributions of the individual sublattices t_i .

Topological charges T ($t_\alpha, t_\beta, t_\gamma$)	
$B = 0$ T	$B = 12$ T
0 [(0, 0, 0), (0, -1, 1)]	0 [(0, 0, 0), (0, -1, 1)]
1 [(1, 0, 0), (1, -1, 1)]	0 [(0, 0, 0), (0, -1, 1)]
-1 [(-1, 0, 0), (-1, -1, 1)]	0 [(0, 0, 0), (0, -1, 1)]

6.5. Conclusions

In summary, we demonstrated that the monolayer of CrTe₂ in the 1T phase can host various topological magnetic states once interfaced with non-magnetic Te-based layers hosting transition metals by using a combination of density functional theory calculations and atomistic spin dynamics. The scrutinized quantum materials were pre-selected to be within an acceptable range of lattice mismatching, which makes the considered atomic structures realistic and hence makes our predictions of the magnetic properties more reliable.

Our main finding is the emergence of a new type of antiferromagnetic topological state consisting of hexamer-meronic spin-texture in a magnetically frustrated environment characterizing the free-standing CrTe₂ as well as the CrTe₂/(Ta, Nb, Ti)Te₂ heterobilayers. This magnetic state forms in a rich set of pair combinations of merons and antimerons, with each pair living in one of the three antiferromagnetic sublattices. By constructing the vdW bilayers, inversion symmetry is broken, which gives rise to a z -component of the Dzyaloshinskii-

Moriya interaction that enhances the stability of these novel meronic textures.

Intriguingly, when CrTe₂ is instead proximitized with (Zr, Rh, Ni)Te₂ layers it displays ferromagnetic behavior, which is imposed by the interface-induced strain, hosting spin-spirals as well as ferromagnetic skyrmions which are both enabled by the DMI. These results provide a potential explanation for the anomalous Hall effect identified in the CrTe₂/ZrTe₂ heterostructures [150]. We note that a recent work predicts the formation of skyrmions in CrTe₂/WTe₂ bilayer [151], which is an interface that we disregarded because of the large lattice mismatch.

Overall, our work highlights CrTe₂ as a promising 2D layer for further exploration of proximity-induced topological magnetism enabled by its strong magneto-elastic coupling [146]. Our findings suggest the possibility of engineering the size and stability of the underlying topological spin-textures by modifying the nature of the interfacing 2D material. In the next chapter, we explore the potential for manipulating topological states using electric fields in (Ti, Rh)Te₂/CrTe₂ heterobilayers. These materials were selected due to their minimal lattice mismatches with CrTe₂ and the distinctive topological magnetic states they induce.

7. Electrical engineering of topological magnetism in 2D heterobilayers

In the previous chapter, our simulations suggest the potential presence of Néel-type frustrated AFM merons in both isolated CrTe_2 monolayers and $\text{CrTe}_2/(\text{Ti}, \text{Nb}, \text{Ta})\text{Te}_2$ heterobilayers, and FM skyrmions in $\text{CrTe}_2/(\text{Ni}, \text{Zr}, \text{Rh})\text{Te}_2$ heterobilayers. In this chapter, we use atomistic spin models in combination with first-principles calculations to uncover the non-trivial impact of an electric field on noncollinear magnetic structures in $\text{CrTe}_2/(\text{Rh}, \text{Ti})\text{Te}_2$ heterobilayers. TiTe_2 and RhTe_2 were chosen for their small lattice mismatches with CrTe_2 and the unique topological magnetic states they introduce as we discussed in the previous chapter. From the experimental point of view, the building-blocks of the heterobilayers, TiTe_2 , RhTe_2 , and CrTe_2 have been experimentally investigated [40–42, 56, 152]. While the possibility of manipulating such topological states through electric fields is recognized, the few experimental studies exploring electric-field-induced switching of skyrmions and skyrmion bubbles considered transition-metal multilayers [153–155] and multiferroic heterostructures [156]. On the theoretical side, research has focused on the alterations to either the magnetic anisotropy (MA) or the DMI [157, 158], whether influenced directly by the electric field or indirectly due to the strain that it induces. More recently, simulations indicated the possibility of stabilizing individual magnetic skyrmions in an ultrathin transition-metal film via external electric fields through the combined effect on the exchange interaction, the DMI, and the MA that dictates the characteristics of magnetic skyrmions [159]. A nonequilibrium approach was also suggested, with the DMI being generated by a femtosecond electric field pulse in an ultrathin metal film [160]. However, no predictions have so far been made on whether skyrmions can be transformed into other topological magnetic states.

In our simulations, for the $\text{CrTe}_2/\text{RhTe}_2$ bilayer sketched in Fig. 7-1 (a), we discover all-electrical switching between two topologically different magnetic structures, FM skyrmions and FM meron pairs (Fig. 7-1 (b)). The perpendicular electric field has a strong influence on the interlayer spacing between the 2D materials, which modifies several key magnetic interactions: the Heisenberg exchange interaction, the DMI and the MA. These electric-field-induced alterations enable the transition of skyrmions into meron structures and vice-versa. A very different scenario arises when interfacing CrTe_2 with TiTe_2 , sketched in Fig. 7-1 (c), which leads to the emergence of frustrated AFM merons (Fig. 7-1 (d)) whose stability and size can be tuned by the applied electric field. Our findings provide a foundation for further exploration in electrically tunable magnetic systems, offering innovative avenues for the design and control of novel spintronic functionalities.

The results discussed in this chapter have been previously published in Ref. [161].

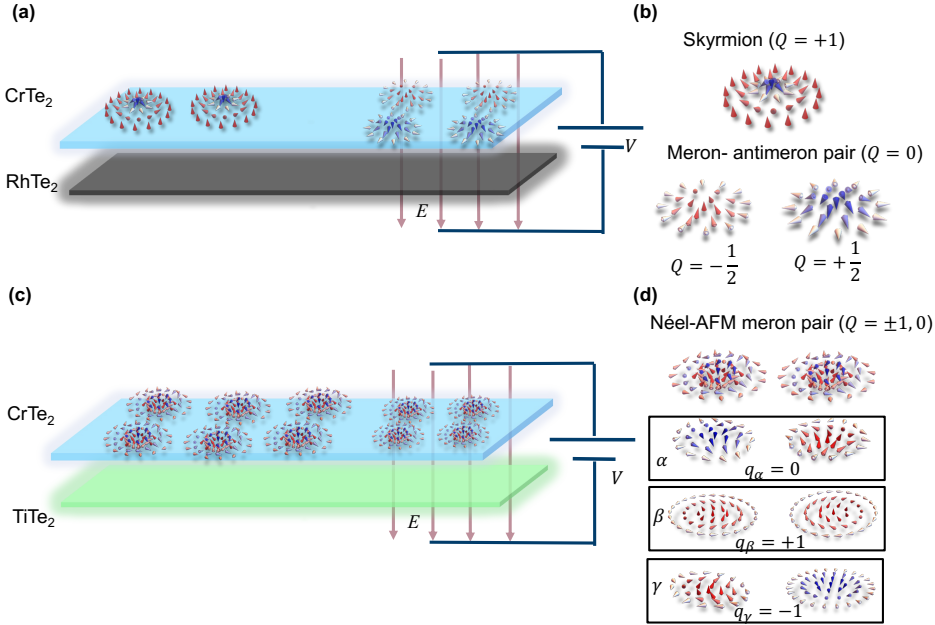


Figure 7-1.: **Overview of the magnetic topological states with and without an electric field in heterobilayers.** (a) CrTe₂/RhTe₂ heterobilayer, with (b) showing FM skyrmions and merons and their net topological charges (Q) which arise in this bilayer. (c) CrTe₂/TiTe₂ heterobilayer, with (d) showing Néel AFM merons which are composed of three FM merons and/or antimerons living in different sublattices (α , β , and γ), with distinct sublattice topological charges (q). For the shown example, the Néel AFM meron pair has $Q = 0$, while the sublattice topological charges are all different ($q_\alpha = 0$, $q_\beta = 1$, $q_\gamma = -1$).

7.1. Computational details

Initially, Atomic position relaxations with an electric field of CrTe₂/(Rh, Ti)Te₂ heterobilayers were assessed using the Quantum Espresso computational package [63–65], with pseudopotentials (PAW), exchange and correlation functional (GGA), and threshold parameters for convergence like the free-standing case with increasing the vacuum to 30 Å. To study the influence of an electric field on the CrTe₂ / (Rh, Ti)Te₂ heterobilayers, a homogeneous external electric field with values changing from 0.1 V/Å to 1.0 V/Å was applied perpendicular to the plane of the heterobilayers. Then, we used the JuKKR computational package [68–71] to extract the magnetic interactions that fit the classical Heisenberg Hamiltonian (see Eq. 2-12) with angular momentum expansion of the Green function, k-mesh, and Fermi-Dirac smearing like the case of the free-standing case. Finally, atomistic spin relax-

ation simulations using Spirit code [125, 126] are used to validate the predictions of complex magnetic states with the simulated annealing method.

7.2. Electric field modulation of the electronic properties in heterobilayers

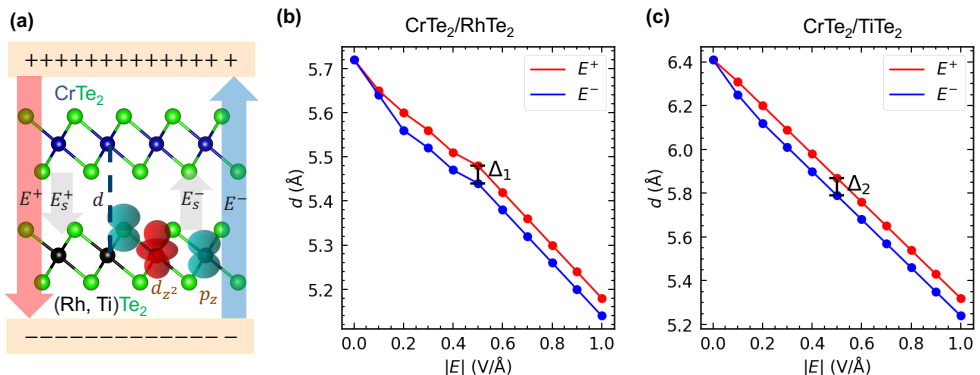


Figure 7-2.: **Impact of the perpendicular electric field on the interlayer distances.**

(a) CrTe₂/(Rh, Ti)Te₂ heterobilayers in a capacitive environment. E_s^+ (E_s^-) are the screened electric fields due to the positive (negative) applied fields. The interlayer distances d as a function of the magnitude of the applied electric field for (b) CrTe₂/RhTe₂ and (c) CrTe₂/TiTe₂ heterobilayers, respectively. Δ_1 and Δ_2 indicate the difference in the interlayer distance for applied fields of equal magnitude in opposite directions for the respective bilayers.

We first performed calculations to obtain the structural and electronic properties and how they respond to an applied electric field. Fig. 7-2 (a) illustrates the setup used to investigate the effects of perpendicular electric fields of both polarities on CrTe₂/(Rh, Ti)Te₂ heterobilayers. The application of an electric field does not alter the stacking configurations of the materials; rather, it influences the energy differences between these configurations. As shown in Appendix Table D-1, the application of an electric field, whether positive (E^+) or negative (E^-), results in a decrease in the energy levels for the stacking configurations of both TiTe₂ and RhTe₂. This implies that the electric field's influence is primarily on the stability of the stackings, reducing the energy thresholds without rearranging the stackings themselves. However, in both cases, we found that the effect of the applied electric field is to decrease the interlayer distance, as shown in as shown in Fig. 7-2 (b-c). For instance, when applying a field of +1.0 V/Å, the interlayer distance decreases from 5.72 Å to 5.18 Å in the CrTe₂/RhTe₂ heterobilayer, and from 6.41 Å to 5.32 Å in the CrTe₂/TiTe₂ heterobilayer. The most striking aspect is the asymmetrical behavior of the interlayer distance when sub-

jected to positive versus negative electric fields. In the given example of $E = +1.0 \text{ V}/\text{\AA}$, this asymmetry manifests as a difference between the respective interlayer distances of $\Delta_1 = 0.04 \text{ \AA}$ in the $\text{CrTe}_2/\text{RhTe}_2$ heterobilayer and $\Delta_2 = 0.07 \text{ \AA}$ in the $\text{CrTe}_2/\text{TiTe}_2$ heterobilayer. We note that such an asymmetry with respect to the polarity of the applied electric field was also found for the dielectric properties of a graphene/MoS2 van der Waals heterostructure [162]. This suggests that the electric field polarity plays a significant role in determining the behavior of these heterobilayers and warrants further investigation. The broad effect of the applied electric field on the heterobilayer can be explained as follows. The electric field polarizes each layer separately, and as the induced electric dipoles on each layer are parallel to each other this leads to an attraction between the two layers and to a reduction of the van der Waals gap between them. This explanation is supported by analyzing and decomposing the charge density obtained from our DFT calculations. The results, shown in Appendix Fig. **D-1**, are for field values of $\pm 0.5 \text{ V}/\text{\AA}$ and $\pm 1.0 \text{ V}/\text{\AA}$. Firstly, we found that the electric field does not transfer charge between the layers. Secondly, the charge transfer within a layer follows the direction of the applied electric field, as expected. The charge accumulating on one of the Te atoms comes both from the other Te atom and the transition metal atom, which shows that the induced electric polarization is not symmetric around the center of the layer (defined by the transition metal atom). We also determined that the charge is transferred to/from the p_z orbitals of the Te atoms and the d_{z^2} orbital of the transition metals as shown from the local density of state in Appendix Fig. **D-2**. Thirdly, we also found that the applied electric field is strongly screened within the van der Waals gap, which we indicate by E_s in Fig. **7-2**. The associated relative permittivity ($\epsilon_r = E/E_s$) is in the 6 to 8 range for $\text{CrTe}_2/\text{RhTe}_2$ and in the 4 to 5 range for $\text{CrTe}_2/\text{TiTe}_2$, respectively. Lastly, the magnitudes of the induced polarization of each layer and of the screened electric field are found to be asymmetric with respect to a change in polarity of the applied electric field. This arises naturally from the heterogeneous nature of the bilayer, with each bilayer having a different electric polarizability, so that the voltage does not drop in the same way across each layer and hence the order in which the layers are arranged with respect to the polarity of the applied electric field matters. The ensuing differences in the induced dipoles on each layer lead to a different attraction between the layers when the polarity is reversed, which explains the previously-found variation in the interlayer distance. The change in the interlayer distance driven by the applied electric field shows a strong electroelastic coupling, which also has strong consequences for the magnetic properties.

7.3. Electric field control of magnetism in CrTe₂/XTe₂ heterobilayers

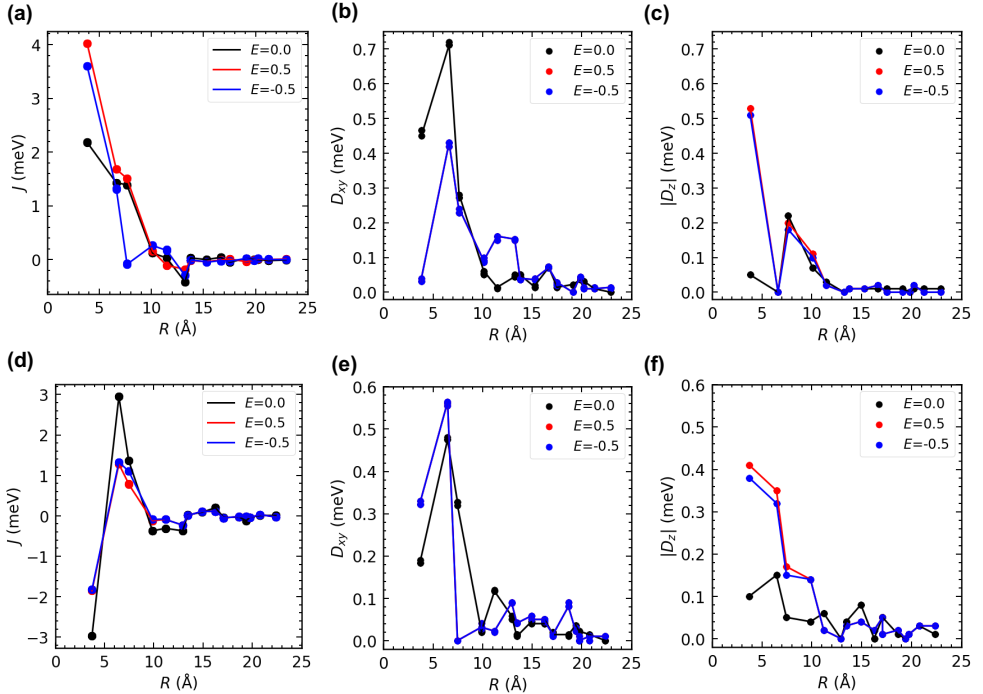


Figure 7-3.: **Magnetic interactions as a function of the distance for the heterobilayers.** (a-c) CrTe₂/RhTe₂. (d-f) CrTe₂/TiTe₂. The symbols denote the Heisenberg exchange (J), and the in-plane ($D_{xy} = \sqrt{D_x^2 + D_y^2}$) and out-of-plane ($|D_z|$) components of the Dzyaloshinskii-Moriya interaction. The distance between Cr atoms for a given pair is labelled R .

To investigate the impact of the electric field on the magnetic properties, we computed the magnetic anisotropy energy and extracted the tensor of magnetic interactions as a function of interatomic distances. We found strong changes in the magnetic interactions of the heterobilayers, evidencing a strong magneto-electric coupling.

We first recap the magnetic interactions without an applied electric field (data shown with black dots in Fig. 7-3). These results were presented in details in our previous chapter, but mainly the Heisenberg exchange interactions J for the CrTe₂/RhTe₂ heterobilayer are predominantly FM, while they have mixed AFM/FM character for CrTe₂/TiTe₂. The energetics

of spiralling magnetic states can be readily obtained from their lattice Fourier transform, and are shown in Appendix Fig. **D-3**. For $\text{CrTe}_2/\text{RhTe}_2$ the energy minimum is found at Γ , indicating the expected FM ground state, while for $\text{CrTe}_2/\text{TiTe}_2$ the energy minimum is shifted away from the K point, signifying a spiralling ground state that locally resembles the triangular Néel AFM state. The non-magnetic layer breaks the inversion symmetry of CrTe_2 and enables the DMI, which is found to be stronger in proximity to RhTe_2 than to TiTe_2 . The final ingredient is the in-plane MAE, $K = 1.70$ meV for $\text{CrTe}_2/\text{RhTe}_2$ and $K = 0.95$ meV for $\text{CrTe}_2/\text{TiTe}_2$. Performing atomistic spin dynamics using all the obtained magnetic interactions in zero magnetic field with the Spirit code, we find the appearance of Néel-type skyrmionic domains for $\text{CrTe}_2/\text{RhTe}_2$ and AFM meron pairs in a spiralling Néel AFM background for $\text{CrTe}_2/\text{TiTe}_2$. We now turn to the effect of the applied electric field on the magnetic interactions, discussing results for $|E| = 0.5$ V/Å for definiteness.

For $\text{CrTe}_2/\text{RhTe}_2$, we see from Fig. **7-3** (a) that the electric field doubles the magnitude of the first-neighbor J while it strongly suppresses the third-neighbor J for negative polarity while having little impact for positive polarity. The electric-field-induced modifications to the DMI are more long-ranged, as seen in Fig. **7-3** (b-c). The first-neighbor DMI vector is rotated from in-plane to out-of-plane, the magnitude of the second-neighbor DMI is suppressed by about 40% without rotation, and the magnitude of some further-neighbor DMIs is enhanced by the electric field. Lastly, the MAE is decreased to 1.08 meV for positive polarity and increased to 1.82 meV for negative polarity, which correspond to changes of -26% and by $+7\%$ with respect to zero applied field, respectively. Due to the combination of weakened in-plane components of the DMI together with strengthened FM Heisenberg exchange, the ground state becomes a more conventional in-plane FM which supports meron pairs. For $\text{CrTe}_2/\text{TiTe}_2$, Fig. **7-3** (d) shows that the electric field strongly weakens both first- (AFM) and second-neighbor (FM) Heisenberg exchange and suppresses longer-ranged AFM interactions, while it enhances and tilts out of the Cr plane the first- and second-neighbor DMI and suppresses the third-neighbor DMI, Fig. **7-3** (e-f). Similar to what was found for the RhTe_2 case, the MAE is reduced to 0.78 meV for positive polarity and enhanced to 1.22 meV for negative polarity, which are variations by -18% and by $+28\%$ of the zero field values, respectively. In both cases, we find that the MAE variation the most pronounced asymmetry with respect to changing the polarity of the electric field.

7.4. Electric field control properties of topological states in $\text{CrTe}_2/\text{XTe}_2$ heterobilayers

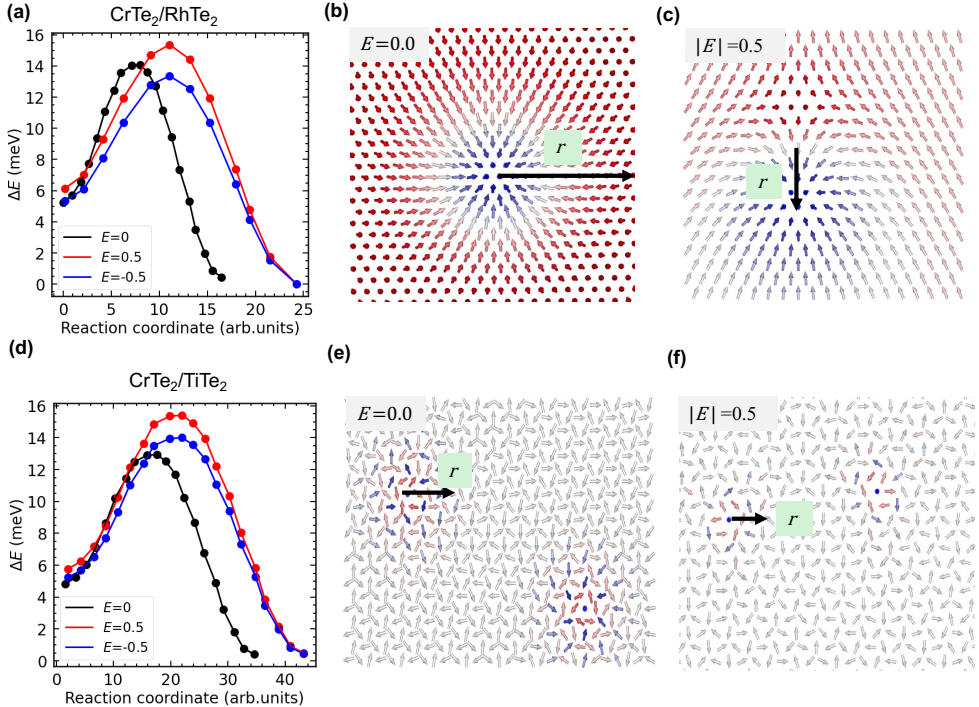


Figure 7-4.: **Topological magnetic textures in heterobilayers.** (a) Energy path for the collapse of isolated FM skyrmions ($E = 0$) or meron pairs ($|E| = 0.5$). (b) Isolated skyrmion selected to calculate energy barriers and explore its stability. (c) Isolated meron pair selected to calculate energy barriers and explore its stability. (d) Energy path for the collapse of isolated Néel AFM meron pairs. (e-f) Isolated Néel AFM meron selected to calculate energy barriers and explore its stability with and without electric field. (a-c) show results for $\text{CrTe}_2/\text{RhTe}_2$ and (d-f) for $\text{CrTe}_2/\text{TiTe}_2$, respectively.

As a final aspect, we explore whether the applied electric field can be considered for manipulation of isolated skyrmions and meron pairs in their respective magnetic backgrounds. To do so, we perform additional spin dynamics simulations for a series of geodesic nudged elastic band (GNEB) simulations [72], which give access to the characteristic size of these magnetic textures as well as the energy barrier that prevents their straightforward unwinding into the

respective magnetic background. We first address $\text{CrTe}_2/\text{RhTe}_2$, with the computed energy barriers reported in Fig. 7-4 (a) and the respective magnetic objects are illustrated in Fig. 7-4 (b-c). Although the electric field drastically modifies the ground state from a skyrmionic domain structure to a simpler in-plane FM, hence changing the nature of the topological defects from skyrmions to meron pairs (or in-plane skyrmions), the energy needed to create these objects from the ground state (origin of the reaction coordinate) and the respective energy barriers are quite similar. The energy barriers show a substantial dependence on the electric field polarity (\pm), varying around 8.6 ± 0.6 meV, which is a combined effect of the changes to the MAE and to the other magnetic interactions. The radius of the meron pairs varies around 2.4 ± 0.1 nm with the polarity, and they are smaller than the zero-field skyrmion which has a radius of about 3.7 nm. We next turn to $\text{CrTe}_2/\text{RhTe}_2$, which retains its spiralling triangular Néel AFM ground state when the electric field is applied. Here the topological defects are Néel AFM meron pairs, with the obtained energy barriers shown in Fig. 7-4 (d) and the respective magnetic structures depicted in Fig. 7-4 (e-f). The barrier heights are 9.3 ± 0.5 meV, which are significantly higher than the zero field value of 8.1 meV. This is accompanied by a field-induced miniaturization of the constituent merons, with their sizes shrinking to 1.9 ± 0.1 nm in comparison to the zero-field value of 2.7 nm. We attribute this shrinking to the combination of weakened Heisenberg exchange and enhanced DMI by the electric field, which enables larger angles between neighboring spin moments and so a full rotation over a smaller distance.

7.5. Conclusions

Our computational study on the electric field control of electronic and magnetic properties in $\text{CrTe}_2/\text{RhTe}_2$ and $\text{CrTe}_2/\text{TiTe}_2$ heterobilayers provides several insights into the intertwined nature of electronic, structural, and magnetic responses. These heterostructures are bonded by weak van der Waals interactions, against which the electric field can compete, leading to a strong dependence of the interlayer distances on the magnitude and polarity of the field. This modulation of the interlayer distance impacts the electronic properties, specifically the charge distribution, leading to pronounced variations in local densities of states and the emergence of a screened electric field in the van der Waals gap. It then follows that the magnetic properties are also strongly modified, evidencing a robust magneto-electric coupling. The Heisenberg exchange interactions, DMI values, and the magnetic ground states respond to the electric field in very distinct ways for the two heterobilayer systems, highlighting the uniqueness of each system's response. The most striking findings are the electric-field-driven transformation of the FM skyrmion into a FM meronic state for the $\text{CrTe}_2/\text{RhTe}_2$ heterobilayer, while $\text{CrTe}_2/\text{TiTe}_2$ retains its spiralling Néel AFM state but with the respective AFM merons being significantly miniaturized by the electric field.

We note that the identification of the unveiled FM and AFM topological spin-textures can be achieved by transport measurements, for example, via all-electrical means using spin-

mixing magnetoresistance [163–165], with its different possible modes [166] or via various Hall effects [167–169]. Other experimental schemes can be utilized such as those based on scattering approaches with electrons [170, 171], X-rays [172] and all-optical relaxometry magnetic microscopy [173].

8. Active learning for spin waves probed by inelastic neutron scattering

As discussed in Sec. 4.2, collective spin excitations in 2D materials have become a prominent research focus in condensed matter physics, largely due to their promising applications in quantum computing, spintronics, magnonics, and other advanced technologies [174, 175]. These excitations, often referred to as magnons or spin waves, are quantized oscillations of spins that propagate through the material [128, 129]. A primary goal in this field has been to characterize wide classes of these excitations, facilitated by advances in spectroscopic techniques such as neutron scattering. These methods assess the kinematics of scattered neutrons to elucidate the dispersion relations, lifetimes, and amplitudes of spin excitations. However, neutron scattering faces challenges due to limited neutron sources, lower neutron flux relative to other sources, and minimal neutron scattering cross-sections. Additionally, this experiment is expensive and time-consuming, demanding significant effort to extract the magnon spectra and the underlying complex magnetic interactions. The analysis of inelastic neutron scattering data typically requires sophisticated models that account for complex interactions within the studied systems. Theoretical frameworks such as linear spin wave theory [176, 177] (See Sec. 4.2), Ab-initio calculations [178, 179], and combined approaches like lattice dynamics and quantum Monte Carlo simulations [180, 181] are commonly used. However, these comprehensive modeling approaches require substantial computational resources and face significant challenges. For example, capturing realistically all relevant interactions is crucial for precise characterization, yet the complexity of these interactions makes developing accurate predictive models difficult. This complexity leads to discrepancies between model predictions and experimental data, necessitating iterative refinements that are resource-intensive and time-consuming.

To address the previous challenges in neutron scattering experiments and their related theoretical models, a promising approach involves incorporating machine learning techniques into the planning and prediction stages. Machine learning has already proven effective in other types of experiments by automating data processing, enhancing the accuracy of parameter predictions, and refining experiment design. For example, x-ray absorption spectroscopy (XAS) can be fitted with different algorithms such as Adversarial Bayesian optimization (ABO) [182], the Radial Basis Functions (RBF) [183] leading to significant improvements in the experimental and computational analysis. Also, various featurization techniques were explored to assess their impact on the performance of machine learning models for XAS analysis in both classification and regression tasks [184]. Moreover, techniques such as non-linear autoencoders streamline the handling of complex datasets, improving experimental setups' efficiency. For example, in studies involving complex systems like spin ice, machine learning enables tuning of Hamiltonian models under varying experimental conditions such

as pressure and temperature, leading to improved predictions of material behaviors and phase diagrams [185–187]. Recently, Convolutional Neural Networks (CNN), trained using linear spin wave simulations, have been employed in inelastic neutron scattering experiments to differentiate between two feasible magnetic exchange models [188]. The performance of CNNs heavily depends on the quality and the size of the training data. However, the data from neutron scattering experiments are noisy and costly to collect, which makes it very difficult to meet the criteria for such a database.

In this chapter, we introduce a machine learning algorithm that integrates active learning sampling with linear spin wave theory leading to Kalman Filter enhanced Adversarial Bayesian Optimization (KFABO) algorithm for approximating the magnon spectrum using a minimal number of both sampling points and iterations. With a minimal number of iterations, the algorithm is capable of addressing noisy neutron scattering data, providing reliable magnetic interactions that recover the experimental spectra and even unlocking hidden or weak interactions such as those induced by spin-orbit coupling.

To corroborate our findings, we explore the antiferromagnetic (AFM) two-dimensional CrSBr material investigated by neutron scattering experiments in Ref. [74]. CrSBr is particularly intriguing due to its unique magnetic properties such as a strong spin-orbit coupling imposing an in-plane magnetization and a large Néel temperature (T_N) of 132 K [57–59, 189], which promotes this material for advanced spintronic applications. In its bulk form, the individual layers are ferromagnetic (FM), while they couple among each other in an AFM fashion as shown in Fig. 8-1. The reported experimental spectra [74] are significantly noisy, which provides an ideal test case for our algorithm. Moreover, the same work provides a fit of the experimental spectra enabling the extraction of Heisenberg exchange interactions and Dzyaloshinskii-Moriya interactions but without resolving the interlayer interaction responsible for the AFM behavior of CrSBr. Noting that previous ab-initio simulations did not recover the associated large Néel temperature by predicting negligible interlayer coupling [188], our algorithm, however, maps from the same and rather noisy experimental data a significant AFM interlayer coupling, which incidentally is confirmed by our first-principles calculations.

”This chapter is the result of a collaborative work involving Yixuan Zhang, a PhD student from the Technical University Darmstadt working with Prof. Dr. Hongbin Zhang. With Yixuan we built up an interface between the KFABO algorithm and the physical model based on LSWT. We conducted the fitting simulations. I performed the associated ab-initio simulations. Overall, I strongly contributed to the assessments, analysis, and the writing-up of the results.”

The results discussed in this chapter have been submitted for publication Ref. [190].

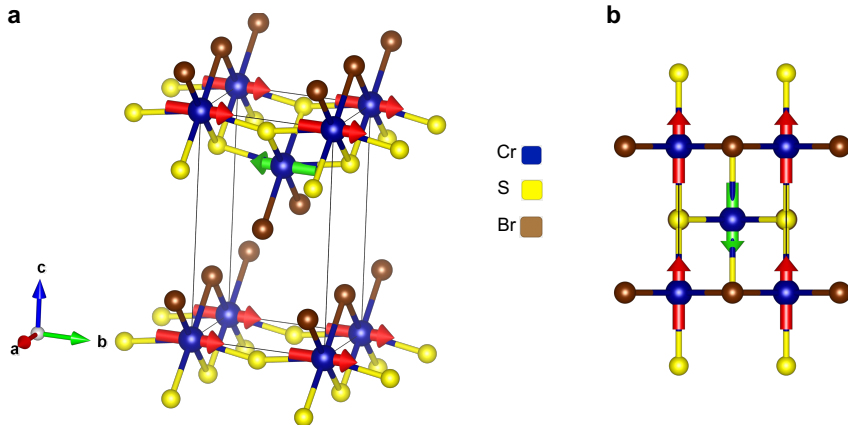


Figure 8-1.: **Illustration of bulk CrSBr crystal structure.** (a) The side view with Cr^{3+} magnetic order, which is ferromagnetic within the plane but layered in alternating directions to exhibit bulk antiferromagnetism. (b) The top view.

8.1. Computational details

In our simulation of fitting the magnon spectrum of CrSBr, we utilize the Kalman filter-enhanced adversarial Bayesian optimization algorithm. As shown in Sec. 4.3.3, this algorithm integrates linear spin wave theory, active learning sampling, and adaptive noise reduction techniques. KFABO consists of two coupled Bayesian optimization (fBO, sBO) algorithms and a Kalman filter. For more details see Sec. 4.3.3.

For our DFT simulations, we follow the computational scheme detailed in the previous chapters for the CrTe_2 (See Secs. 5.1, 6.1, 7.1). First, we relaxed the bulk crystal structure (See Sec. 3.3.1), determining the lattice constants as $a = 3.50 \text{ \AA}$, $b = 4.76 \text{ \AA}$, and $c = 7.96 \text{ \AA}$ using the Quantum espresso computational package [63–65], with pseudopotentials (PAW), exchange and correlation functional (GGA), and threshold parameters for convergence like the case of CrTe_2 with a k-mesh of $16 \times 12 \times 8$ points, plane-wave energy cut-off is 70 Ry, and without vacuum. Then, we used the JuKKR computational package [68–71] to extract the magnetic interactions that fit the classical Heisenberg Hamiltonian (see Eq. 2-12) with angular momentum expansion of the Green function, and Fermi-Dirac smearing like the case of the free-standing case of CrTe_2 , expt k-mesh of $32 \times 24 \times 16$ points. Moreover, we have calculated the spin wave curves along with linear spin wave theory (see Sec. 4.2) as implemented in the SpinW code [133], achieving a good agreement with those fitted by the KFABO algorithm as shown in the Appendix Fig. E-4 (d-f). Finally, the Néel temperature was calculated using the Monte Carlo simulation as implemented in Spirit code [72].

8.2. Algorithm benchmarking

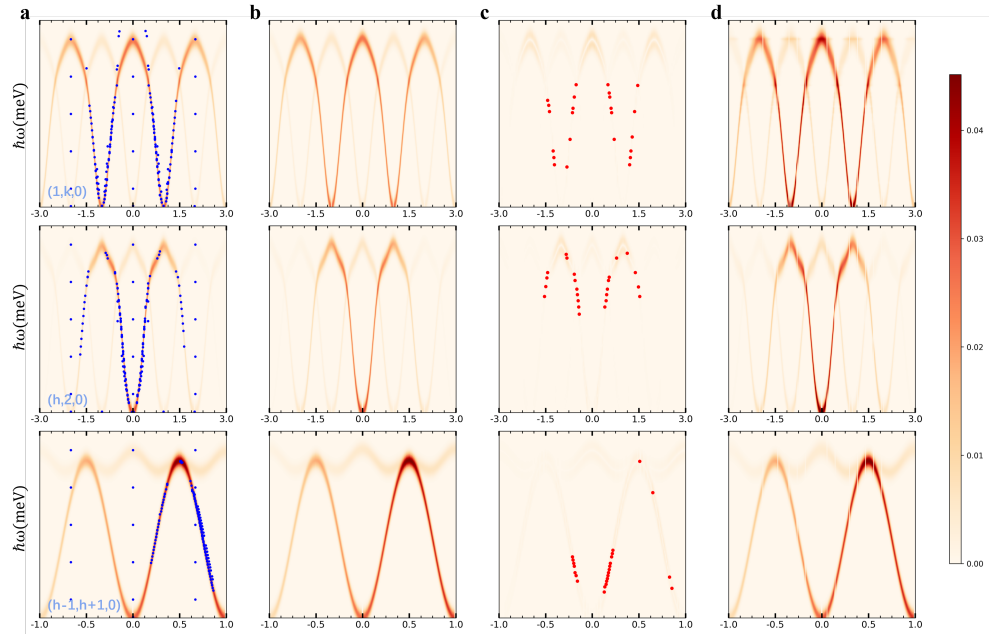


Figure 8-2.: Magnon spectrum for CrSBr with only J -values along three q -paths ($(1, k, 0)$, $(h, 2, 0)$, and $(h - 1, h + 1, 0)$). (a) The target magnon spectrum (orange curve) along the three q -paths using the Ref. [74] fitted parameters. The blue points are the active sampling points from previous iterations that were suggested by the sBO. (b) The fBO fitted the magnon spectrum among the three q -paths using only the information from blue sample points. (c) The absolute intensity deviation between the standard function and fBO's prediction, while the red points denote the sample points to be measured for the next round suggested by sBO. (d) The current state as perceived by the KFABO, which the model samples based on that state. The magnitudes of intensity are described by the color bar.

In this section, we combine the LSWT and active-learning sampling together, leading to a KFABO algorithm (see Sec. 4.3.3). The objective of this algorithm is to approximate the calculated magnon spectrum using the minimum number of sampling points necessary. We use a physical model of LSWT with 8 independent nearest neighboring Heisenberg exchange interactions J , feeding the Hamiltonian in Eq. 2-7. The interactions are injected as parameters in the fitting Bayesian optimization algorithm. A binning parameter (dE) [191] leads to a Gaussian broadening of spin wave spectra. This effective broadening is induced by both

experimental conditions, electronic and dissipation mechanisms, which limit the lifetime of the magnonic modes. The simulation of the latter requires complex theoretical frameworks, which incorporate time-dependent phenomena and many-body physics [192–199]. Both the magnetic interactions and the spectral broadening are automatically fitted by our algorithm during the active learning (AL) process.

As a starter, we use the Heisenberg magnetic exchange interactions (up to eight neighboring interactions) that were extracted from the fit of the experimental data published in Ref. [74] to obtain the target ground truth spin wave spectra along three wavevector paths - $(1, k, 0)$, $(h, 2, 0)$, and $(h - 1, h + 1, 0)$ - (see Appendix Fig. E-4 (c)). The necessity of fitting all paths together arises from the incompleteness of information provided by individual paths. The detailed analysis in Appendices Fig. E-2 and Table E-2 demonstrates the significant differences and potential inaccuracies when fewer paths are used. As aforementioned, since the AFM interlayer interaction was not resolved in the fit reported in Ref. [74], we consider it to be zero in the first part of our study devoted to the benchmarking of our algorithm. Regarding the broadening, we note that we assume a value of 3 meV for the energy binning parameter.

The algorithm quickly recovers the shape of the spectra in 3 iterations, using only 261 sample data points in total. It precisely predicts the Heisenberg exchange parameters in 8 iterations using 621 data points (cf. Fig. 8-2 and Supplementary image file "Theoretical_SPINW_woDMI.gif" in Supplementary-gifs [200]). The location of these points is depicted in Fig. 8-2 (a), together with the target magnon spectrum (orange curves). Fig. 8-2 (b) shows the calculated magnon spectrum (orange curves) based on the fBO fitted magnetic interaction parameters (cf. Table 8-1), with the pixel-by-pixel absolute deviation between the fitted spin wave and the target one are shown in Fig. 8-2 (c). The fitting is quite good, with an average deviation of 0.00013 and a maximum deviation smaller than 0.004 (compared with the normalized maximum peak intensity with a value of 1). The maximum deviation is primarily due to the energy-broadening parameter, which can be reduced by further sampling and fitting. This parameter quickly converges to a rough range at the very beginning of the algorithm, as it is crucial and important for determining the intensity dispersion during this period. Subsequently, the algorithm shifts its focus to refining the magnetic parameters rather than this parameter. However, perfectly fitting the broadening parameter requires more points on the fringes of the intensity peaks, which are less informative for refining the magnetic interaction parameters and the shape of the spin wave.

Fig. 8-2 (d) represents the current state as perceived by the algorithm. This state is identified as the optimal state to obtain the most effective information through further sampling, using the fBO fitting results and the latest sampling data. The sampling results indicate that most points are close to the peaks, except for four less effective sampling points, located near the top center of the q-path $(1, k, 0)$. These points were sampled during the fourth iteration and showed about a 10meV difference from the actual peaks. In fact, these points provide crucial information that helps improve the state quality and reduce uncertainty (cf. Supplementary

image file "Theoretical_SPINW_woDMI.gif", iteration 4, Fig. d in [Supplementary-gifs \[200\]](#)). From this GIF file, it is evident that the AL process converges after eight iterations, and then the information gain progressively diminishes. This convergence can be confirmed by tracking the state changes across iterations. This indicates that state tracking can serve as a powerful tool for determining the stopping criterion. For example, the refinement of the broadening parameter requires more sampling on the fringes of the peaks, which occurs after the state changes converged. Therefore, it would be more effective to stop after convergence. What is particularly interesting is that, even though the importance of the parameters (refers to how much each parameter contributes to a model's prediction) is not explicitly coded into our KFABO algorithm, it can still automatically make decisions as the AL iterations proceed, this confirms the adaptive nature of the model.

Table [8-1](#) illustrates the effectiveness of the fitting procedure by comparing our fitted Heisenberg exchange parameters with their corresponding target values while quantifying the disparities through absolute differences. In this case, all three paths are used in combination. The fitting shows consistent accuracy, with absolute differences below 0.05 meV for all J neighbors. For example, the interactions up to the third nearest neighbors J_1 , J_2 and J_3 show absolute differences of 0.0373 meV, 0.0306 meV and 0.0043 meV, respectively, indicating a strong correlation, and a good agreement with the ones reported in Ref. [\[74\]](#).

Besides the Heisenberg exchange interactions, a fit of the DMI (Eq. [2-11](#)) was extracted in Ref. [\[74\]](#). Starting from spin waves spectra generated by both interactions, Heisenberg and DMI, the KFABO algorithm recovers the shape of the associated magnon spectrum (cf. Appendix Fig. [E-3](#)) in the third iteration using 261 data points, and it converges in the ninth iteration using 693 data points (cf. Supplementary image file "Theoretical_SPINW_wDMI.gif" in [Supplementary-gifs \[200\]](#)) where the parametric accuracy of the final fBO fitted model is only slightly reduced (cf. Table [E-1](#)) compared to the case where DMI is excluded. Unlike the test without DMI, the sampling Bayesian optimization sampling is less stable and efficient, with more sampling points deviating from the actual peak positions. This slight reduction in accuracy can be attributed to the addition of DMI, which increases the difficulty in the magnon spectra predictions by fBO. By introducing an extra dimension of DMI into the Hilbert surface of this fitting problem, the complexity and non-convexity of the surface is increased. A detailed discussion on this matter can be found in Sec. [E.1](#).

8.3. Experimental spin wave spectrum fitting

In this part, we applied the KFABO algorithm to directly fit the experimental spin wave spectrum of CrSBr [\[74\]](#) along three q-paths ($(1, k, 0)$, $(h, 2, 0)$, and $(h - 1, h + 1, 0)$). As shown in Fig. [8-3](#) (a), experimental spin wave spectra often include random noise due to various sources such as instrumental limitations, environmental factors, or inherent variability in the material properties. The Kalman filter processes all available measurements to estimate the variables of interest with more accuracy than would be possible by using a

Table 8-1.: Comparison between the KFABO fitted and target Heisenberg exchange interactions up to eight nearest neighbors. The target interactions were reported in Ref. [74] after a fit of the experimental data. The table lists the absolute differences.

J neighbours	KFABO fitted J (meV)	Target J (meV)	Absolute difference (meV)
1	-1.9407	-1.9034	0.0373
2	-3.3426	-3.3792	0.0366
3	-1.6741	-1.6698	0.0043
4	-0.1112	-0.0933	0.0179
5	-0.0805	-0.0896	0.0091
6	0.0001	0.0000	0.0001
7	0.3960	0.3665	0.0295
8	-0.2881	-0.2932	0.0051

single measurement alone and reducing noise in data. Fig. 8-3 (a) depicts the experimental magnon spectra along three different q -paths. The intensity of the magnon excitations is shown using a color scale, where darker regions indicate higher intensity. The blue points superimposed on these spectra represent the sample points chosen by the KFABO algorithm during the fitting process. These points are critical as they guide the optimization process. Fig. 8-3 (b) shows the calculated magnon spectrum using the fitted magnetic interactions by our algorithm after the noise reduction. A high degree of agreement between the algorithm-fitted spectrum and the original experimental spectrum can be observed. Additionally, by examining the sampling distribution in Fig. 8-3 (a), it is evident that the algorithm samples very efficiently despite the strong noise in the experimental data. Most sampling points are concentrated near the peaks, and when sampling noisy regions, the algorithm requires only a small number of sample points to determine the noise level and avoid the associated regions in subsequent iterations (for example, the point around (2.2, 20) in q -path $(h, 2, 0)$). The algorithm recovers the shape of the spin wave in 3 iterations using 281 data points (cf. Supplementary file "Experimental.SPINW_wDMI.gif" in [Supplementary-gifs \[200\]](#)) and it converges after the seventh iteration with 481 data points, as evidenced by the algorithm-perceived state shown in Fig. 8-3 (c). The parameters fitted by the KFABO algorithm are in good agreement with the experimentally fitted parameters [74] with the exception of a small but finite AFM interlayer coupling (6th neighboring magnetic interaction) value of 0.25 meV, see Table 8-2. Previously, the latter was not resolved with a conventional fitting procedure [74] and was predicted to be negligible by first-principles simulations [201], which would not explain the large Néel temperature characterizing CrSBr.

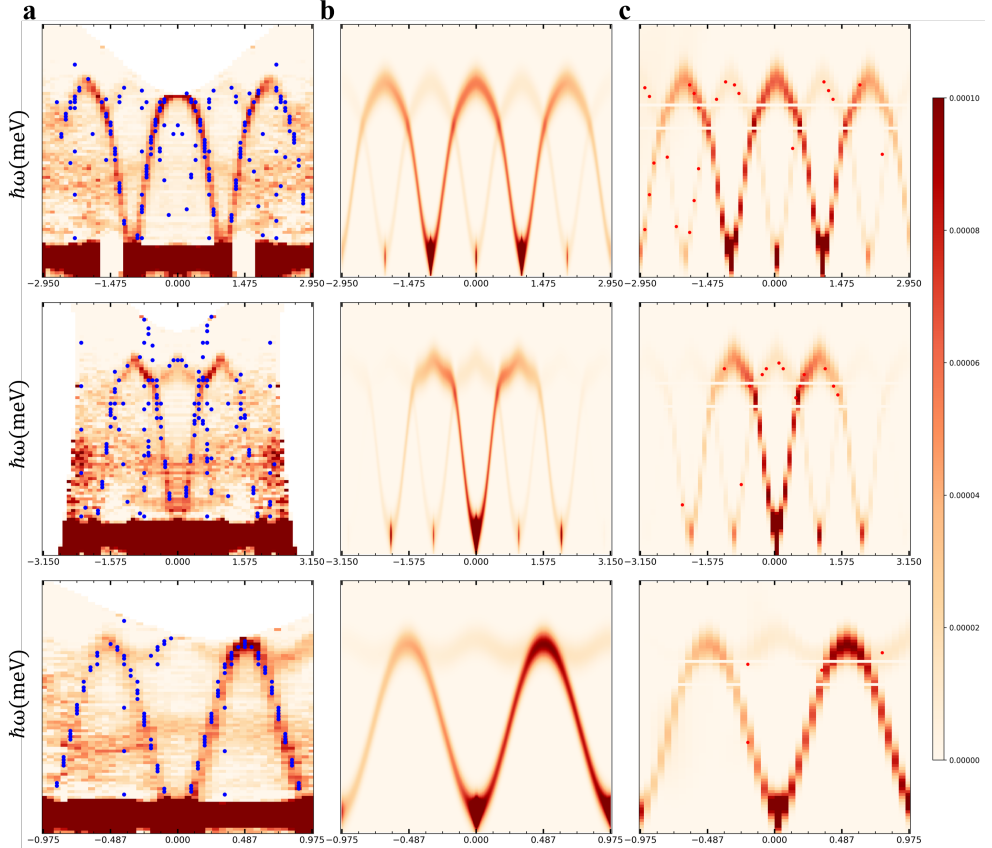


Figure 8-3.: **Experimental magnon spectrum for CrSBr along three q-paths** ($(1, k, 0)$, $(h, 2, 0)$, and $(h - 1, h + 1, 0)$). (a) Fitting the experimental magnon spectrum (orange curve) along the three q-paths, where the blue points are the sampling points that obtained using the KFABO algorithm. (b) The calculated spin wave curve along the three q-paths by considering the extracted magnetic parameters. (c) The current state as perceived by the KFABO which the model samples based on that state, and the red points denote the samples to be measured for the next round suggested by sBO.

Motivated by this finding, we proceeded to ab-initio simulations of the magnetic properties of CrSBr (see Method section). We extracted the distance-dependent magnetic interactions, presented in Table 8-2 and Appendix Fig. E-4 (a). We recover the intralayer FM coupling (cf. Appendix Fig. E-4 (b)) and predict an in-plane orientation of the magnetic moments due to a magnetic anisotropy energy of 0.15 meV. The algorithm fitted intralayer parameters

agree with those obtained from our ab-initio simulation as shown in Table 8-2. The smallest absolute differences between the ab-initio and the KFABO fitted Heisenberg exchange interactions are found for the fourth, fifth, seventh, and eighth nearest neighboring coupling. The rest of the intralayer interactions exhibit a slightly larger absolute differences and remain within an acceptable consistency range. It is worth mentioning that due to the complexity of the experimental procedure and the non-uniform distribution of experimental noises in the magnon spectra measurements, deviations from the independent first-principles results are expected. Given this context and the fact that the algorithm can only access the measured points, it is impressive that the algorithm achieves such comparable parameter estimates. More importantly, the first-principles simulations recover the interlayer AFM coupling of 0.21 meV, which leads to a Néel temperature of 130 K as verified by our Monté Carlo simulations. Moreover, we calculated the DMI and found a finite value of 0.31 meV only for the first nearest neighbors, which is in excellent agreement with the one extracted from the experimental data (0.35 meV). This highlights the precision that KFABO can achieve in assessing intricate spin-orbit coupling effects. Such precision is crucial for understanding asymmetric energy landscapes in magnetic materials, which in turn can influence domain wall dynamics and skyrmion stability [20, 84, 85, 202–205].

The significant agreement between the fitted parameters and the ab-initio ones, as well as between the excitation dispersion spectra demonstrate the effectiveness of the KFABO algorithm in extracting accurate magnetic parameters and capturing the fundamental features of the magnon spectrum from noisy experimental data. This capability is crucial for effectively reducing the number of experimental measurements and accelerating the associated complex processes.

8.4. Conclusion

In this chapter, we exposed our approach and results for fitting the spin wave spectra of CrSBr through the KFABO algorithm. First, by combining linear spin wave theory with active-learning sampling, we implemented the KFABO algorithm to approximate the target magnon spectra using minimal sampling points. Our initial fitting uses eight independent Heisenberg exchange parameters and the results, compared to LSWT-based fits reported in Ref. [74], show that the KFABO algorithm accurately reproduces the magnon spectrum across all q-paths. The sampling points that deviate from the peaks have proven to be the informative points, helping the algorithm to converge more quickly and greatly improve the sampling efficiency based on the algorithm’s perceived state change tracking. Also, the same level of efficiency for sampling can be observed when including the DMI.

Additionally, the analysis of fitting accuracy using different path configurations reveals that the information provided by some paths may be incomplete, necessitating careful selection of multiple paths to avoid introducing non-convexity (cf. Appendix Fig. E-2). To address this issue, we propose to determine the ground state of the material first, and then strategically

Table 8-2.: Comparison between the KFABO fitted and ab-initio Heisenberg exchange interactions up to eight nearest neighbors. The absolute differences are provided. The DMI interaction is significant for the nearest neighboring one and reaches a value of 0.35 meV, which agrees well with the one extracted from ab-initio (0.31 meV).

J neighbors	KFABO fitted J (meV)	Ab-initio J (meV)	Absolute differences (meV)
1	-2.29	-2.05	0.24
2	-3.23	-3.11	0.12
3	-1.47	-1.56	0.09
4	-0.16	-0.09	0.07
5	-0.14	-0.09	0.05
6	0.25	0.21	0.04
7	0.36	0.37	0.01
8	-0.24	-0.31	0.07

select q-paths close to this state for detailed analysis. This solution is predicated on the assumption that paths near the ground state provide a more complete and representative magnon spectrum. To validate the previous solution and demonstrate the wide reliability of our algorithm, we applied the algorithm to the complete magnon spectrum of another material with a well-understood ground state, La_2CuO_4 as shown in Fig. E-5. By focusing sampling points around the known minimum ground state, it is possible to enhance both the accuracy and comprehensiveness of the magnon spectrum analysis. This strategy not only minimizes the discrepancies in key parameters but also ensures a richer dataset for validating theoretical models.

Regarding the fit of the noisy experimental data, we apply the KFABO algorithm to automatically address and reduce noise in the data. This approach allows for more accurate parameter estimation and very effective sample points, as presented in the experimental magnon spectra along three q-paths. Crucially, the algorithm is capable of quantifying a finite AFM interlayer coupling of 0.25 meV, which was unresolved in the fitting procedure applied in Ref. [74]. Impressively, this value agrees with our ab-initio simulations, which together with the rest of distant-dependent magnetic interactions predict a Néel temperature of 130K that matches the experimental value [189].

Overall, the good performance of the proposed scheme, which combines machine learning with physical modeling, suggests a promising avenue for future research in material science, especially in areas with significant experimental limitations. The methods developed here have clear potential to efficiently reduce costs and time-consuming numerical and experimental processes, opening new vistas in addressing the physics of magnonics and spintronics.

9. Conclusions

In this thesis, a multiscale modeling approach was utilized to investigate the complex magnetism in two-dimensional van der Waals materials, addressing in particular CrTe₂-based heterostructures and CrSBr. Central to this approach was the integration of first-principles calculations based on density functional theory (DFT) with spin atomistic models (See Chapters 3, 4). DFT, a quantum mechanical modeling method, provided a detailed understanding of the electronic structure and magnetic interactions at the atomic level. The structural relaxation of the materials was performed using the plane wave method implemented in the Quantum ESPRESSO (QE) code [206], ensuring accurate atomic positions and lattice parameters for subsequent calculations. The relaxed structures were then used to compute magnetic interactions employing the Korringa-Kohn-Rostoker (KKR) Green function method with the JuKKR code [207]. This approach allowed for precise calculation of magnetic interactions (exchange interactions, magnetic anisotropy, and the Dzyaloshinskii-Moriya interaction) in complex systems by using the infinitesimal rotation technique (See Sec. 3.4.9). These parameters were then input into atomistic spin models using the Spirit code [208], facilitating the simulation of magnetic relaxation on a larger scale. This integration enabled the exploration of complex magnetic states, including non-collinear and chiral magnetic configurations (eg. skyrmions, merons). Additionally, the atomistic spin model based on the Geodesic Nudged Elastic Band simulations were utilized to quantify energy barriers between the initial (skyrmions, merons) and final states (FM, AFM).

First of all, this study revealed that the single layer of CrTe₂ exhibits a rich variety of structural phases, each associated with distinct magnetic configurations, including non-trivial non-collinear magnetic states driven by long-range competing exchange interactions. The presence of the Dzyaloshinskii-Moriya interaction in some of these structures promotes chiral magnetism, which we thoroughly evaluated. Our constrained simulations, focusing on collinear magnetism, align with previous density functional theory calculations reported in the literature [42, 44], confirming that a CrTe₂ monolayer favors a zig-zag antiferromagnetic ground state.

Then, we investigated various structural phases to explore the potential of engineering two-dimensional topological magnetism in CrTe₂ monolayers by constructing heterostructures with Te-based layers incorporating non-magnetic transition metals. Our findings unveiled the presence of novel topological antiferromagnetic objects, such as multi-meronic particles, in the free-standing 1T phase of CrTe₂. These particles, emerging in a frustrated in-plane Néel magnetic environment, hold significant promise for information technology applications due to their expected immunity to the skyrmion Hall effect, which typically causes the undesired deflection of conventional skyrmions upon application of a current. Furthermore, our research demonstrates the ability to manipulate the stability and nature of the underlying magnetic states by building various heterostructures. More importantly, we anticipate that besides

the fundamental importance of identifying the frustrated antiferromagnetic multi-meronic textures, patching the same 2D material such as CrTe_2 with distinct 2D layers such as those unveiled in this work, favoring either ferromagnetic skyrmions or antiferromagnetic merons, can be useful constituents of information technology devices. We envisage, for instance, their potential application for the ultimate control and transport of dissimilar topological objects to carry information in well-designed regions of multiple 2D vdW heterojunctions, as schematically depicted in Fig. 9-1.

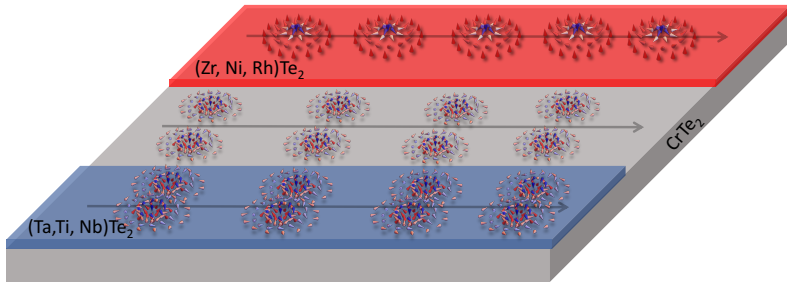


Figure 9-1.: **Potential technological device concept combining 2D CrTe_2 with other 2D layers, such as $(\text{Ta}, \text{Nb}, \text{Ti})\text{Te}_2$.** Which promote antiferromagnetic merons as topological magnetic defects, and $(\text{Zr}, \text{Rh}, \text{Ni})\text{Te}_2$ layers that promote ferromagnetic skyrmions. The various types of topological spin textures can then be injected from one device region to another, and driven using applied spin currents or thermal gradients, for instance.

Additionally, we uncovered the non-trivial impact of electric fields on noncollinear magnetic structures in $\text{CrTe}_2/\text{RhTe}_2$ and $\text{CrTe}_2/\text{TiTe}_2$ heterobilayers. For the $\text{CrTe}_2/\text{RhTe}_2$ bilayer, we discovered all-electrical switching between two topologically distinct magnetic structures: FM skyrmions and FM meron pairs. The perpendicular electric field strongly influences the interlayer spacing between the 2D materials, thereby modifying several key magnetic interactions, including the Heisenberg exchange interaction, the Dzyaloshinskii-Moriya interaction, and the magnetic anisotropy. These electric-field-induced alterations enable transitions between skyrmions and meron structures. In contrast, interfacing CrTe_2 with TiTe_2 results in the emergence of frustrated AFM merons, whose stability and size can be finely tuned by the applied electric field. Our findings lay a robust foundation for further exploration in electrically tunable magnetic systems, offering innovative avenues for the design and control of novel spintronic functionalities. These advances pave the way for the practical realization of new spintronic devices, where the manipulation of magnetic states by electric fields could lead to more efficient and versatile applications in data storage and processing. Fig. 9-2 shows some potential applications and implications of our findings. Firstly and as illustrated in Fig. 9-2 (a), we anticipate a 2D memory device using the $\text{CrTe}_2/\text{RhTe}_2$ heterobilayer, where merons and skyrmions in CrTe_2 define respectively the two magnetic bits '1' and '0'.

The bits are written owing to an underlying grid of gates that set the voltage pattern and induce locally a voltage that nucleates the skyrmions or merons. We note that the size of the device is not limited to 5×4 bits, as shown in Fig. 9-2 (a), but can be larger. In Fig. 9-2 (b-c) we introduce a compact racetrack memory device. In contrast to the conventional one based solely on skyrmions, bits are represented by having skyrmions ('1') and no-skyrmions ('0'). In such a case, it is non-trivial to control the size of the no-skyrmion region, which affects the whole concept of encoding information in a binary fashion. In our proposal, space is filled up with skyrmions and merons. Thus, the scheme does not hinge on controlling the size of the "empty" regions. Both topological objects (bits) can be moved along the track without relying on an in-plane current but by switching the voltage pattern appropriately as done in Fig. 9-2 (c), which enables for example to switch the positions of a meron and a skyrmion.

Overall, combining the functionalities of both FM skyrmions and AFM merons in one device could pave the way for multifunctional spintronic devices based on van der Waals hetero-bilayers, where data storage, transmission, logic operations, and signal processing could be integrated in a compact and efficient manner.

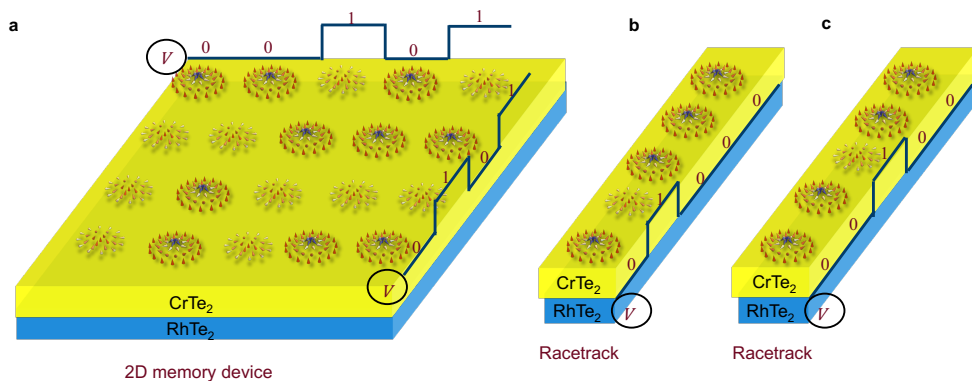


Figure 9-2.: (a) A representation of a 2D memory device with the generation of various bit sequences by an electric pulse (V). (b,c) A racetrack memory device that enables the movement of a magnetic bit (eg. meron) along the track.

Finally, we shifted our focus to using machine learning for another aspect of two-dimensional materials, specifically magnons in CrSBr. Spin waves or magnons have potential applications in quantum computing, spintronics, magnonics, and other advanced technologies. These magnons are characterized using traditional methods such as inelastic neutron scattering, which is typically time-consuming and requires extensive data processing due to limited neutron sources, and noisy resulting data. To address these challenges, we introduce a novel machine learning algorithm that combines linear spin wave theory, and adaptive noise reduc-

tion with active learning sampling, termed the Kalman Filter enhanced Adversarial Bayesian Optimization (KFABO). This algorithm significantly improves the process of restoring spin wave information from minimal inelastic neutron scattering point data, thereby enhancing the experiment efficiency and enabling accurate extraction of magnetic parameters. The robustness of our method is further demonstrated when applied to noisy CrSBr experimental data, where the KFABO algorithm effectively addresses and reduces noise during the active sampling process, leading to resolving magnetic interactions and accurately predicting Heisenberg exchange parameters as well as hidden or weak interactions, such as those induced by spin-orbit coupling. For example, we successfully identified a significant AFM interlayer coupling in CrSBr, which was previously unresolved using conventional methods and explains the measured large Néel temperature. This finding, supported by our first-principles calculations, highlights the capability of our algorithm to uncover critical interactions in magnetic materials.

Overall, our research provides a substantial contribution to the understanding and manipulation of magnetic properties in 2D materials. By uncovering the strong coupling between magnetism and crystal structure in CrTe₂ and demonstrating the potential for electric-field manipulation of magnetic states, we have laid the groundwork for future explorations and practical applications in spintronics. Additionally, our use of machine learning, particularly the KFABO algorithm, to fit the spin wave spectrum of CrSBr, highlights the powerful synergy between advanced computational techniques and material science. The KFABO algorithm not only accurately reproduced magnon spectra with minimal sampling points but also effectively addressed and reduced noise in the data, leading to precise parameter estimation. More importantly, it detected interactions, that were hidden or not identified with conventional fitting procedures. Looking forward, the integration of machine learning with physical modeling can be further enhanced. For instance, the development of neural networks that incorporate the symmetry properties of materials could significantly advance the prediction and analysis of magnon spectra. Such neural networks could automate and optimize the extraction of magnetic parameters from experimental data, streamlining the research process and enabling more efficient design of spintronic devices.

A. Appendix (Chapter 2)

A.1. Spin models on a Bravais lattice

In this section we want to calculate the contributions from each magnetic interaction to the total magnetic energy per site for any Bravais lattice, and to do this we rewrite Eq. 2-19 as:

$$\mathbf{S}_i = \sin \theta \left(\frac{e^{i\mathbf{q}\cdot\mathbf{R}_i} + e^{-i\mathbf{q}\cdot\mathbf{R}_i}}{2} \mathbf{n}_1 + \frac{e^{i\mathbf{q}\cdot\mathbf{R}_i} - e^{-i\mathbf{q}\cdot\mathbf{R}_i}}{2i} \mathbf{n}_2 \right) + \cos \theta \mathbf{n}_3. \quad (\text{A-1})$$

A.1.1. Exchange interactions

First, to calculate the contribution from the exchange interactions to total energy we calculate $\mathbf{S}_i \cdot \mathbf{S}_j$:

$$\begin{aligned} \mathbf{S}_i \cdot \mathbf{S}_j &= \sin^2 \theta \left(\frac{e^{i\mathbf{q}\cdot\mathbf{R}_i} + e^{-i\mathbf{q}\cdot\mathbf{R}_i}}{2} \frac{e^{i\mathbf{q}\cdot\mathbf{R}_j} + e^{-i\mathbf{q}\cdot\mathbf{R}_j}}{2} + \frac{e^{i\mathbf{q}\cdot\mathbf{R}_i} - e^{-i\mathbf{q}\cdot\mathbf{R}_i}}{2i} \frac{e^{i\mathbf{q}\cdot\mathbf{R}_j} - e^{-i\mathbf{q}\cdot\mathbf{R}_j}}{2i} \right) + \cos^2 \theta \\ &= \sin^2 \theta \left(\frac{1}{2} e^{i\mathbf{q}\cdot(\mathbf{R}_i - \mathbf{R}_j)} + \frac{1}{2} e^{-i\mathbf{q}\cdot(\mathbf{R}_i - \mathbf{R}_j)} \right) + \cos^2 \theta \\ &= \sin^2 \theta \cos \mathbf{q} \cdot (\mathbf{R}_i - \mathbf{R}_j) + \cos^2 \theta, \end{aligned}$$

then, we substitute the previous equation in Eq. 2-12:

$$\mathcal{E}_J = - \sum_{i,j} J_{ij} (\sin^2 \theta \cos \mathbf{q} \cdot (\mathbf{R}_i - \mathbf{R}_j) + \cos^2 \theta). \quad (\text{A-2})$$

We can re-write the previous equation when $R_i = 0$ as:

$$\mathcal{E}_J = - \sin^2 \theta [J(\mathbf{q}) - J(0)] - J(0), \quad (\text{A-3})$$

where:

$$J(\mathbf{q}) = \sum_j J_{0j} \cos(\mathbf{q} \cdot \mathbf{R}_j), \quad (\text{A-4})$$

and

$$J(0) = \sum_j J_{0j}. \quad (\text{A-5})$$

If we consider two or more atoms in the unit cell we can re-write the equation as:

$$J(\mathbf{q}) = \sum_{nij} J_{0i,nj} e^{-i\mathbf{q}\cdot(\mathbf{R}_{0n} + \mathbf{R}_{ij})}, \quad (\text{A-6})$$

where n is the unit cell hosting atom j .

A.1.2. Dzyaloshinskii-Moriya interaction

Next, to calculate the contribution to the energy from the DM interaction, we calculate $\mathbf{S}_i \times \mathbf{S}_j$

$$\begin{aligned} \mathbf{S}_i \times \mathbf{S}_j &= \sin \theta \cos \theta [\sin \mathbf{q} \cdot \mathbf{R}_i - \sin \mathbf{q} \cdot \mathbf{R}_j] \mathbf{n}_1 - \sin \theta \cos \theta [\cos \mathbf{q} \cdot \mathbf{R}_i - \cos \mathbf{q} \cdot \mathbf{R}_j] \mathbf{n}_2 \\ &\quad + \sin^2 \theta [\cos \mathbf{q} \cdot \mathbf{R}_i \sin \mathbf{q} \cdot \mathbf{R}_j - \sin \mathbf{q} \cdot \mathbf{R}_i \cos \mathbf{q} \cdot \mathbf{R}_j] \mathbf{n}_3, \end{aligned} \quad (\text{A-7})$$

then, we substitute Eq.A-7 in Eq. 2-12:

$$\begin{aligned} \mathcal{E}_D &= - \sum_{ij} \mathbf{D}_{ij} \cdot [\sin \theta \cos \theta (\sin \mathbf{q} \cdot \mathbf{R}_i - \sin \mathbf{q} \cdot \mathbf{R}_j) \mathbf{n}_1 - \sin \theta \cos \theta (\cos \mathbf{q} \cdot \mathbf{R}_i - \cos \mathbf{q} \cdot \mathbf{R}_j) \mathbf{n}_2 \\ &\quad + \sin^2 \theta (\cos \mathbf{q} \cdot \mathbf{R}_i \sin \mathbf{q} \cdot \mathbf{R}_j - \sin \mathbf{q} \cdot \mathbf{R}_i \cos \mathbf{q} \cdot \mathbf{R}_j) \mathbf{n}_3]. \end{aligned} \quad (\text{A-8})$$

If we re-write the $\cos(\mathbf{q} \cdot \mathbf{R}_j)$ and $\sin(\mathbf{q} \cdot \mathbf{R}_j)$ as an exponential, we see that the first two terms in the dot product are vanishing because $\sum_{i,j} \mathbf{D}_{ij} \cdot e^{i\mathbf{q} \cdot \mathbf{R}_i}$, and $\sum_{i,j} \mathbf{D}_{ij} \cdot e^{i\mathbf{q} \cdot \mathbf{R}_j}$ are equal to zero because $D_{ij} = -D_{ji}$. Finally, using $\sin(a-b) = \sin a \cos b - \cos a \sin b$ we get:

$$\mathcal{E}_D = \sin^2 \theta \sum_{i,j} (\mathbf{n}_3 \cdot \mathbf{D}_{ij}) \sin \mathbf{q} \cdot (\mathbf{R}_i - \mathbf{R}_j) \quad (\text{A-9})$$

If we put $R_i = 0$ then:

$$\mathcal{E}_D = - \sin^2 \theta \sum_j (\mathbf{n}_3 \cdot \mathbf{D}_{0j}) \sin \mathbf{q} \cdot \mathbf{R}_j. \quad (\text{A-10})$$

If we consider two or more atoms in the unit cell we can re-write the equation as:

$$\mathcal{E}_D = - \sin^2 \theta \sum_{nij} (\mathbf{n}_3 \cdot \mathbf{D}_{0i,nj}) \sin \mathbf{q} \cdot (\mathbf{R}_{0n} + \mathbf{R}_{ij}). \quad (\text{A-11})$$

A.1.3. Magnetic anisotropy

Finally, for the magnetic anisotropy, we find:

$$\begin{aligned} \mathcal{E}_A &= - \sum_i K_i [\sin^2 \theta \cos^2 (\mathbf{q} \cdot \mathbf{R}_i + \phi) (\mathbf{n}_1 \cdot \mathbf{z})^2 + \sin^2 \theta \sin^2 (\mathbf{q} \cdot \mathbf{R}_i + \phi) (\mathbf{n}_2 \cdot \mathbf{z})^2 + \cos^2 \theta (\mathbf{n}_3 \cdot \mathbf{z})^2 \\ &\quad + 2 \sin \theta \cos \theta \cos (\mathbf{q} \cdot \mathbf{R}_i + \phi) (\mathbf{n}_1 \cdot \mathbf{z}) (\mathbf{n}_3 \cdot \mathbf{z}) + 2 \sin \theta \cos \theta \sin (\mathbf{q} \cdot \mathbf{R}_i + \phi) (\mathbf{n}_2 \cdot \mathbf{z}) (\mathbf{n}_3 \cdot \mathbf{z}) \\ &\quad + 2 \sin^2 \theta \sin (\mathbf{q} \cdot \mathbf{R}_i + \phi) \cos (\mathbf{q} \cdot \mathbf{R}_i + \phi) (\mathbf{n}_1 \cdot \mathbf{z}) (\mathbf{n}_2 \cdot \mathbf{z})] \end{aligned} \quad (\text{A-12})$$

If we use $\cos^2 a = \frac{1+\cos 2a}{2}$, $\cos a = \frac{e^{ia}+e^{-ia}}{2}$, we got the sum for each term as (Consider $K_i = K$):

- $-\sum_i K_i \sin^2 \theta \cos^2(\mathbf{q} \cdot \mathbf{R}_i + \phi) (\mathbf{n}_1 \cdot \mathbf{z})^2 = -\sin^2 \theta (\mathbf{n}_1 \cdot \mathbf{z})^2 \sum_i K_i (\frac{1}{2} + \frac{1}{4}(e^{2i(\mathbf{q} \cdot \mathbf{R}_i + \phi)} + e^{-2i(\mathbf{q} \cdot \mathbf{R}_i + \phi)}))$
 $= -K (\mathbf{n}_1 \cdot \mathbf{z})^2 \sin^2 \theta (\frac{1}{2} + \frac{1}{2} \delta_{\mathbf{q}, \frac{\mathbf{q}}{2}} \cos 2\phi)$
- $-\sum_i K_i \sin^2 \theta \sin^2(\mathbf{q} \cdot \mathbf{R}_i + \phi) (\mathbf{n}_2 \cdot \mathbf{z})^2 = -\sin^2 \theta (\mathbf{n}_2 \cdot \mathbf{z})^2 \sum_i K_i (\frac{1}{2} - \frac{1}{4}(e^{2i(\mathbf{q} \cdot \mathbf{R}_i + \phi)} + e^{-2i(\mathbf{q} \cdot \mathbf{R}_i + \phi)}))$
 $= -K \sin^2 \theta (\mathbf{n}_2 \cdot \mathbf{z})^2 (\frac{1}{2} - \frac{1}{2} \delta_{\mathbf{q}, \frac{\mathbf{q}}{2}} \cos 2\phi)$
- $-\sum_i K_i \cos^2 \theta (\mathbf{n}_3 \cdot \mathbf{z})^2 = -K \cos^2 \theta (\mathbf{n}_3 \cdot \mathbf{z})^2$
- $-\sum_i 2K_i \sin \theta \cos \theta \cos(\mathbf{q} \cdot \mathbf{R}_i + \phi) (\mathbf{n}_1 \cdot \mathbf{z}) (\mathbf{n}_3 \cdot \mathbf{z}) = -2K \delta_{\mathbf{q}, \mathbf{0}} \sin \theta \cos \theta \cos \phi (\mathbf{n}_1 \cdot \mathbf{z}) (\mathbf{n}_3 \cdot \mathbf{z})$
- $-\sum_i 2K_i \sin \theta \cos \theta \sin(\mathbf{q} \cdot \mathbf{R}_i + \phi) (\mathbf{n}_2 \cdot \mathbf{z}) (\mathbf{n}_3 \cdot \mathbf{z}) = -2K \delta_{\mathbf{q}, \mathbf{0}} \sin \theta \cos \theta \sin \phi (\mathbf{n}_2 \cdot \mathbf{z}) (\mathbf{n}_3 \cdot \mathbf{z})$
- $-\sum_i 2K_i \sin^2 \theta \sin(\mathbf{q} \cdot \mathbf{R}_i + \phi) \cos(\mathbf{q} \cdot \mathbf{R}_i + \phi) (\mathbf{n}_1 \cdot \mathbf{z}) (\mathbf{n}_2 \cdot \mathbf{z}) = -(\mathbf{n}_1 \cdot \mathbf{z}) (\mathbf{n}_2 \cdot \mathbf{z}) \sin^2 \theta$
 $\sum_i 2K_i \sin 2(\mathbf{q} \cdot \mathbf{R}_i + \phi) = -2K \delta_{\mathbf{q}, \frac{\mathbf{q}}{2}} \sin^2 \theta \sin 2\phi (\mathbf{n}_1 \cdot \mathbf{z}) (\mathbf{n}_2 \cdot \mathbf{z})$

B. Appendix (Chapter 5)

B.1. Hubbard parameter U

We have calculated U via the linear response approach implemented in Quantum Espresso code and obtained a value of about 4 eV. However, calculations that incorporate this U value result in an incorrect prediction of an antiferromagnetic ground state for bulk CrTe_2 . This contradicts the ferromagnetic behavior observed in experiments, as reported in [38]. Previous DFT simulations by other groups [44] agree with our findings. For a broader picture of the impact of U on the magnetic interactions, we plot in Fig. B-1 the eigenvalues of $J(q)$ as a function of the reciprocal vector q for the two cases without and with $U = 4$ eV. Overall the two curves are quite similar, showing that the inclusion of U does not lead to large quantitative changes in the magnetic exchange interactions, except where it concerns the interlayer coupling (path $\Gamma - A$). The switching of the energy minimum from Γ to A indicates that the ground state switches from ferromagnetic for $U = 0$ to a layered antiferromagnetic ground state for $U = 4$ eV.

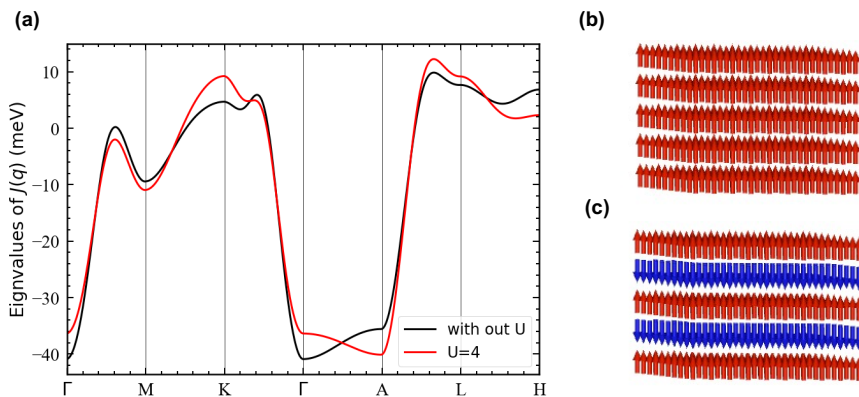


Figure B-1.: **Magnetic state in bulk CrTe_2 .** (a) Eigenvalues of the Fourier-transformed exchange interactions as a function of q at different values of the electric field in bulk CrTe_2 . (b) Magnetic ground state without U . (c) Magnetic ground state without $U=4$ eV.

C.Appendix (Chapter 6)

C.1. Electronic properties of the different stacking orders

The table presents values that correspond to lattice constants (a) and interlayer distances (h) for the different stacking of the CrTe_2 , and XTe_2 , where X represents transition metals: Titanium (Ti), Niobium (Nb), Nickel (Ni), Zirconium (Zr), and Rhodium (Rh). The lattice constant values for different elements range from 3.67 to 3.82 Å. These are typical values for metallic elements, indicating the size of the unit cell of the crystal structure. The smallest lattice constant is for Nb (3.67 Å) and the largest for Zr (3.82 Å). There is a small variation in lattice constants for each element with the different stacking orders. The interlayer distance values range from 3.46 to 4.08 Å. These values are larger than the lattice constants, which is common since interlayer distances are typically greater than distances within the same layer due to weaker bonding between layers. The smallest interlayer distance is for Ni (3.46 Å) and the largest is for Ti (4.08 Å). This significant range suggests different bonding characteristics and possibly different crystal structures or phases.

	Ti		Nb		Ni		Zr		Rh	
a	3.73	3.71	3.70	3.67	3.81	3.80	3.82	3.81	3.79	3.78
	3.71	3.72	3.67	3.68	3.77	3.80	3.79	3.81	3.76	3.78
h	3.76	3.98	3.65	4.00	3.46	3.67	3.75	3.83	3.50	3.69
	4.08	3.94	4.06	3.77	3.71	3.64	4.08	3.82	3.76	3.62
<i>a</i> : lattice constant in Å, <i>h</i> : interlayer distance in Å ΔE : difference in energy between differ stacking with respect to AA stacking in meV									AA	AA'
									AB	A'B

Figure C-1.: **Electronic properties of the different stacking orders.** The lattice constants (a) and interlayer distances (h) for the different stacking orders of the $\text{CrTe}_2/\text{XTe}_2$ heterobilayers.

C.2. Saddle points of the AFM merons, and FM skyrmions

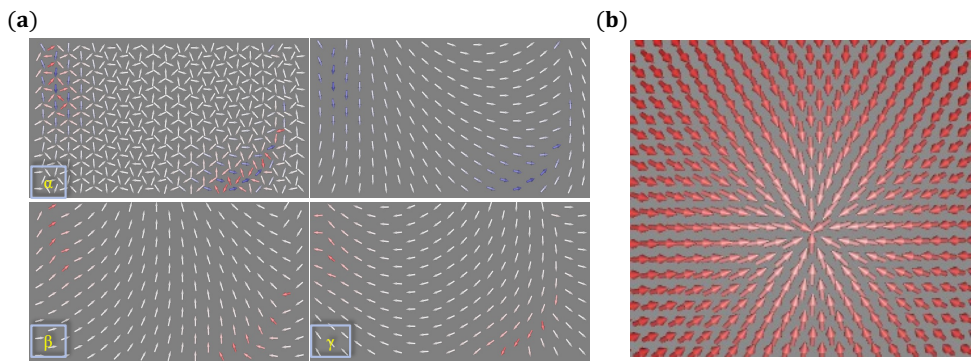


Figure C-2.: **The spin-texture associated with the saddle point.** (a) AFM merons
(b) FM skyrmions in the $\text{CrTe}_2/\text{XTe}_2$ heterobilayers.

D.Appendix (Chapter 7)

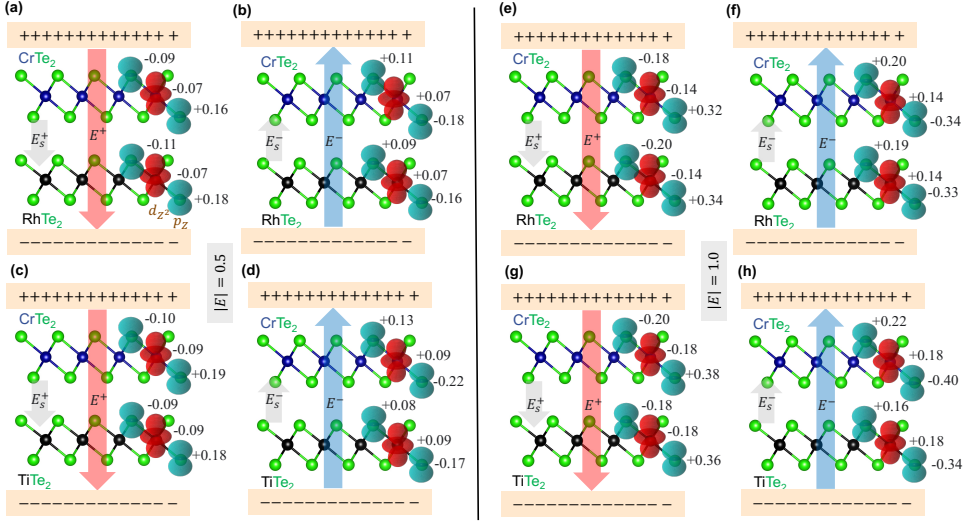


Figure D-1.: Charge accumulation with respect to the perpendicular (both positive and negative) electric field. $|E| = 0.5$ V/Å: (a-b) CrTe₂/RhTe₂ heterobilayer. (c-d) CrTe₂/TiTe₂ heterobilayer. $|E| = 1.0$ V/Å: (e-f) CrTe₂/RhTe₂ heterobilayer and (g-h) CrTe₂/TiTe₂ heterobilayer. E_s^+ (E_s^-) are the screened electric fields due to the positive (negative) external fields. The colored spheres represent the charge difference between the zero electric field case and the ± 0.5 V/Å and ± 1.0 V/Å.

Table D-1.: Energy differences in meV of various stacking with respect to AA for TiTe₂ and RhTe₂ under positive/negative electric field.

Stacking	$E = 0$		0.5 V/Å		-0.5 V/Å	
	TiTe ₂	RhTe ₂	TiTe ₂	RhTe ₂	TiTe ₂	RhTe ₂
AA'	105.3	185.5	96.9	170.7	96.7	170.3
AB	30.3	120.8	27.9	111.1	27.8	110.9
AB'	9.9	61.6	9.1	56.7	9.1	56.5

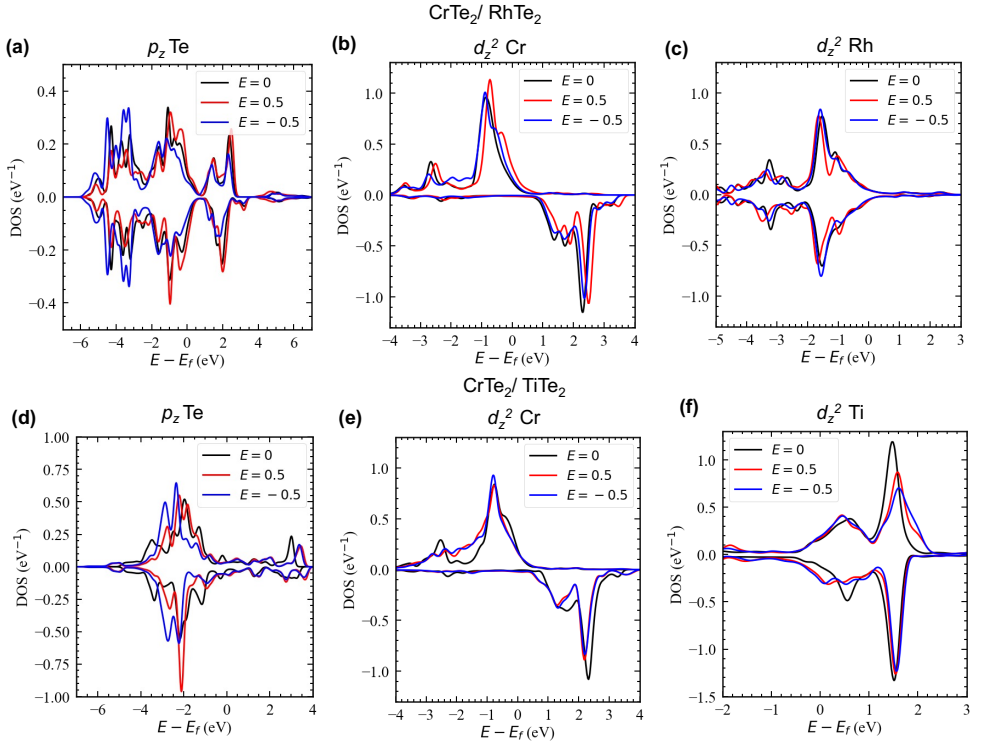


Figure D-2.: Selected orbital contributions to the local density of states. (a-c) CrTe₂/RhTe₂ heterobilayer. (d-f) CrTe₂/TiTe₂ heterobilayer. We plot the atom-projected contributions with p_z -orbital symmetry for Te, and with d_{z^2} -orbital symmetry for the transition metal atoms.

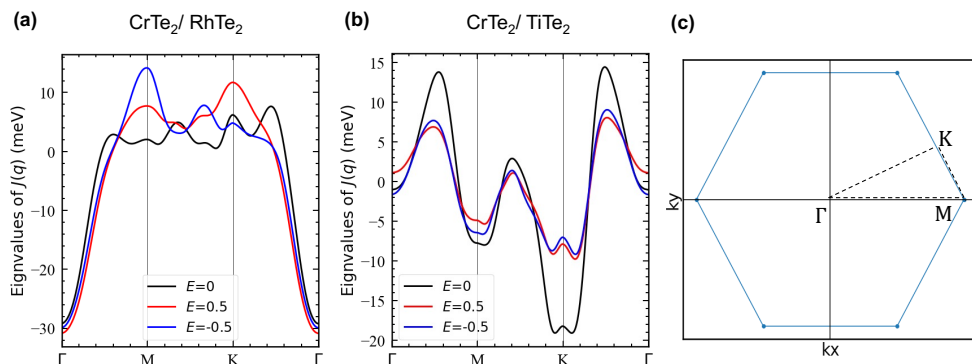


Figure D-3.: **Energetics of magnetic states for the heterobilayers based on the computed exchange interactions.** (a,b) Eigenvalues of the Fourier-transformed exchange interactions as a function of q at different values of the electric field in CrTe₂/RhTe₂ and CrTe₂/TiTe₂ heterobilayers, respectively. (c) The hexagonal first Brillouin zone.

E.Appendix (Chapter 8)

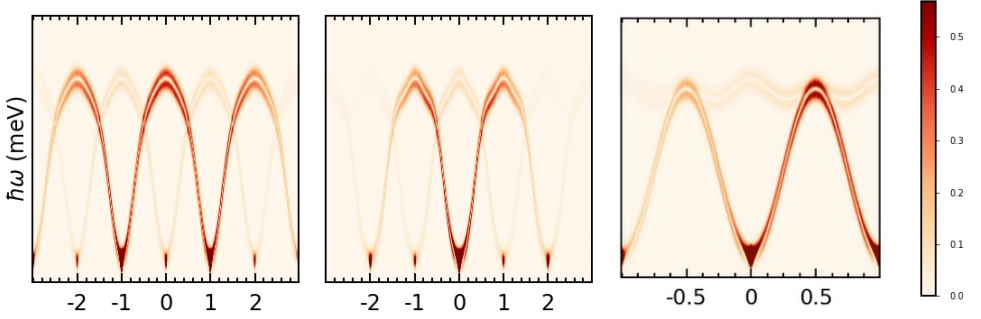


Figure E-1.: The pixel-by-pixel absolute differences plot of of bulk CrSBr between the spin wave with and without the interlayer AFM coupling (0.21 meV) for three different wavevector paths: $(1, k, 0)$, $(h, 2, 0)$, and $(h - 1, h + 1, 0)$. The intensity of two spin waves was normalized into the same scale. The darker the color indicates the larger the differences. The curve with a larger peak for the case of including interlayer AFM coupling.

E.1. Algorithm benchmarking with choosing specific q-path, and inclusion DMI

In this section, we depict first our fitting using the Heisenberg exchange parameters from Ref. [74] by choosing only a single path $(1, k, 0)$ as shown in the Fig. E-2. The KFABO spin wave function aligns reasonably well with the LSWT function, with the maximum and average losses of 0.001278 and 0.000027, respectively. While Fig. E-2 (b) compares the fitting accuracy when a second path $(h, 2, 0)$ is added with the maximum and average losses are 0.001407 and 0.000014. Comparatively, the magnetic interactions fitted as shown in Appendix Table. 1, where one path $-(1, k, 0)$ - and then two paths $-(1, k, 0), (h, 2, 0)$ - are used, the differences of both cases are much higher than the 3-path case, such as J_1 showing a significant difference of 0.2593 and 1.7789 in each case. This indicates that the information obtained from these two paths is only part of the information for this fitting problem. If we try to solve the parameter fitting problem by relying only on this incomplete information, there may be many local optimal solutions that are very close to the global optimal solution, which greatly increases the non-convexity of the problem and decreases the probability that we will find the true optimal solution.

Then we included the DMI to our fitting as shown in Fig. E-3 and Supplementary image

file "Theoretical_SPINW_wDMI.gif" in [Supplementary-gifs \[200\]](#). The KFABO algorithm recovers the shape of the magnon spectrum in the third iteration using 261 data points, and it converges in the ninth iteration using 693 data points where the parametric accuracy of the final fBO fitted model is only slightly reduced (cf. Table E-2) compared to the case where DMI is excluded. One can see that from Table E-2, the inclusion of the DMI in parameter fitting slightly diminishes the modeling precision of the KFABO algorithm. Notably, the first, fourth, sixth, and eighth nearest neighboring interactions $-J_1$, J_4 , J_6 , and J_8 (Fig. E-4 (a)) maintain the same level of accuracy compared to the case where DMI is excluded. While the other interactions still maintain reasonable accuracy but show slightly higher deviations. And unlike the test without DMI, the sampling Bayesian Optimization (sBO) sampling is less stable and efficient, with more sampling points deviating from the actual peak positions. This slight reduction in accuracy can be attributed to the addition of DMI, which increases the difficulty in the magnon spectra predictions by fBO. By introducing an extra dimension of DMI into the Hilbert surface of this fitting problem, the complexity and non-convexity of the surface are increased.

Table E-1.: Comparison between the KFABO fitted and target Heisenberg exchange interactions up to eight nearest neighbors. The absolute differences are provided. The DMI interaction is significant for the nearest neighboring one and reaches a value of 0.2850 meV, which agrees well with the target one (0.3100 meV).

J neighbors	KFABO fitted J (meV)	Target J (meV)	Absolute difference (meV)
1	-1.9155	-1.9034	0.0121
2	-3.3500	-3.3792	0.0292
3	-1.6677	-1.6698	0.0021
4	-0.0690	-0.0933	0.0243
5	-0.1515	-0.0896	0.0619
7	0.4216	0.3665	0.0551
8	-0.3041	-0.2932	0.0109

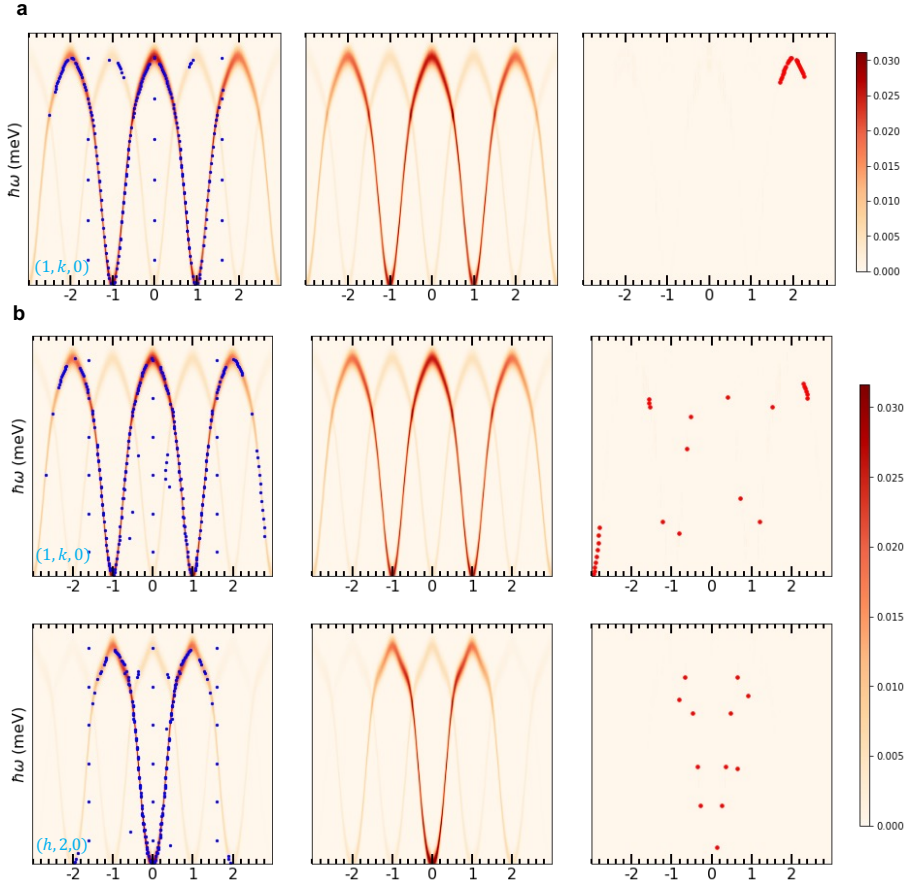


Figure E-2.: Magnon spectrum for CrSBr with only J -values for specific q -paths. (a) $(1, k, 0)$. (b) $(1, k, 0)$, and $(h, 2, 0)$. The left panel represents the target magnon spectrum (orange curve) using the Ref. [74] fitted parameters, where the blue points are the active sampling points from previous iterations that were suggested by the sBO. The middle panel represents the fBO fitted magnon spectrum using only the information from blue sample points. The last panel represents the absolute intensity deviation between the standard function and fBO's prediction, while the red points denote the samples to be measured for the next round suggested by sBO. The magnitudes of intensity are described by the color bar.

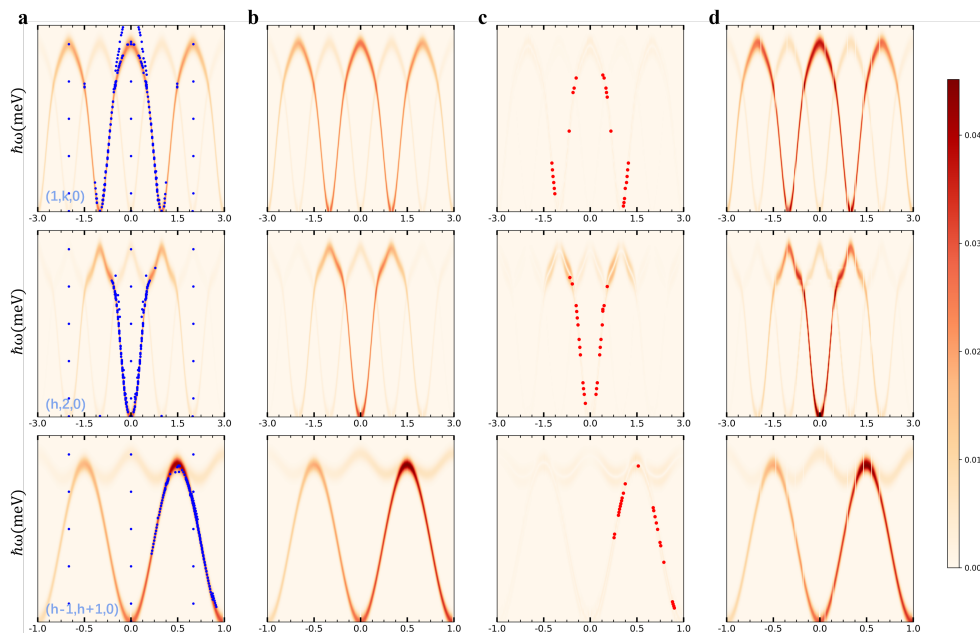


Figure E-3.: Magnon spectrum for CrSBr with including the DMI along three q -paths ($(1, k, 0)$, $(h, 2, 0)$, and $(h-1, h+1, 0)$). (a) The target magnon spectrum (orange curve) along the three q -paths using the Ref. [74] fitted parameters. The blue points are the active sampling points from previous iterations that were suggested by the sBO. (b) The fBO fitted the magnon spectrum among the three q -paths using only the information from blue sample points. (c) The absolute intensity deviation between the standard function and fBO's prediction, and the red points denote the samples to be measured for the next round suggested by sBO. (d) The current state as perceived by the KFABO, which the model samples based on that state. The magnitudes of intensity are described by the color bar.

Table **E-2.**: Comparison of KFABO fitted parameters versus target parameters using only one $(1, k, 0)$ path and two paths $(1, k, 0)$ with $(h, 2, 0)$. The target interactions were reported in Ref. [74] after a fit of the experimental data.

q-path	J neighbours	KFABO fitted J (meV)	Target J (meV)	Absolute difference (meV)
$(1, k, 0)$	1	-1.6441	-1.9034	0.259
	2	-3.3820	-3.3792	0.0028
	3	-1.4160	-1.6698	0.2538
	4	-0.2207	-0.0933	0.1274
	5	-0.0895	-0.0896	0.0001
	7	0.3627	0.3665	0.0038
	8	-0.2898	-0.2932	0.0034
	$(1, k, 0)$ and $(h, 2, 0)$	1	-0.1245	-1.9034
2		-3.0738	-3.3792	0.3054
3		-1.5114	-1.6698	0.1584
4		-0.1752	-0.0933	0.0819
5		-0.3913	-0.0896	0.3017
7		0.1541	0.3665	0.2124
8		-0.2920	-0.2932	0.0012

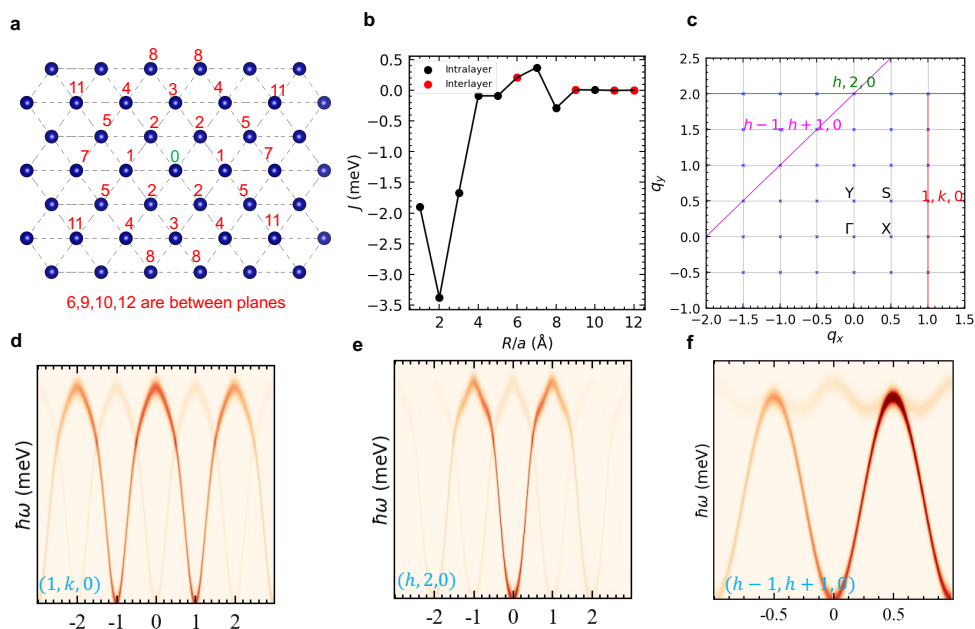


Figure E-4.: **Illustration of magnetic properties of bulk CrSBr.** (a) The top view of bulk CrSBr up to 11th neighbors (6,9,10,12 are between planes). (b) The values of Heisenberg exchange interaction up to the 12th nearest neighbors where red points are associated to neighbors 6, 9, 10, and 12, which are situated in the adjacent plane to atom 0. (c) Top view of the first Brillouin zone of bulk CrSBr. (d-f) Spin-wave dispersion curves along three different wavevector paths: $(1, k, 0)$, $(h, 2, 0)$, and $(h - 1, h + 1, 0)$.

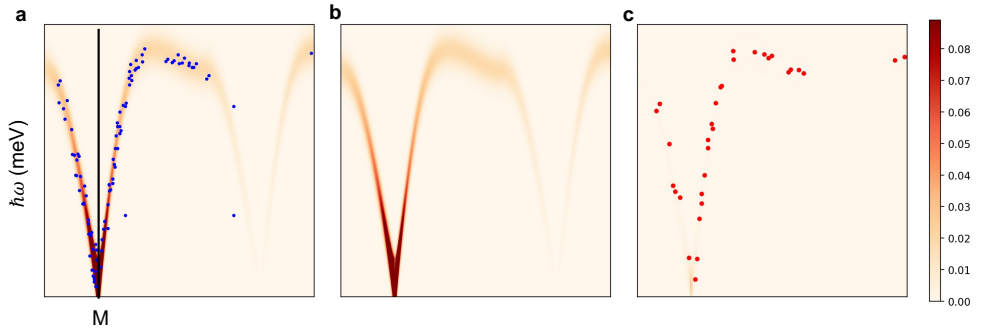


Figure E-5.: Magnon spectrum fitting in La_2CuO_4 if we have portion information around the high symmetry point M. (a) The target magnon spectrum (orange curve) among the three q-paths using the DFT calculated parameters. The blue points are the active sampling points from previous iterations that were suggested by the sBO. (b) The fBO fitted the magnon spectrum among the three q-paths using only the information from blue sample points. (c) The absolute intensity deviation between the standard function and fBO's prediction, and the red points denote the samples to be measured for the next round suggested by sBO. The magnitudes of intensity are described in the color bar.

Bibliography

- [1] K. S. Novoselov, A. K. Geim, S. V. Morozov, D. Jiang, Y. Zhang, S. V. Dubonos, I. V. Grigorieva, and A. A. Firsov, “Electric field effect in atomically thin carbon films,” *Science*, vol. 306, no. 5696, pp. 666–669, 2004.
- [2] A. K. Geim and I. V. Grigorieva, “Van der waals heterostructures,” *Nature*, vol. 499, no. 7459, pp. 419–425, 2013.
- [3] K. S. Novoselov, A. Mishchenko, A. Carvalho, and A. H. C. Neto, “2d materials and van der waals heterostructures,” *Science*, vol. 353, no. 6298, p. aac9439, 2016.
- [4] S. Z. Butler, S. M. Hollen, L. Cao, Y. Cui, J. A. Gupta, H. R. Gutiérrez, T. F. Heinz, S. S. Hong, J. Huang, A. F. Ismach, E. Johnston-Halperin, M. Kuno, V. V. Plashnitsa, J. A. Robinson, R. S. Ruoff, S. Salahuddin, J. Shan, L. Shi, M. G. Spencer, M. Terrones, W. Windl, and J. E. Goldberger, “Progress, challenges, and opportunities in two-dimensional materials beyond graphene,” *ACS Nano*, vol. 7, no. 4, pp. 2898–2926, 2013.
- [5] C. Lee, X. Wei, J. W. Kysar, and J. Hone, “Measurement of the elastic properties and intrinsic strength of monolayer graphene,” *Science*, vol. 321, no. 5887, pp. 385–388, 2008.
- [6] A. Castro Neto, F. Guinea, N. Peres, K. Novoselov, and A. Geim, “The electronic properties of graphene,” *Reviews of Modern Physics*, vol. 81, no. 1, p. 109, 2009.
- [7] J. Y. Lim, M. Kim, Y. Jeong, K. R. Ko, S. Yu, H. G. Shin, J. Y. Moon, Y. J. Choi, Y. Yi, T. Kim, and S. Im, “Van der waals junction field effect transistors with both n- and p-channel transition metal dichalcogenides,” *npj 2D Materials and Applications*, vol. 2, no. 1, p. 37, 2018.
- [8] B. Rawat, V. M. M., and R. Paily, “Transition metal dichalcogenide-based field-effect transistors for analog/mixed- signal applications,” *IEEE Transactions on Electron Devices*, vol. 66, no. 5, pp. 2424–2430, 2019.
- [9] H. Wu, A. Chen, P. Zhang, H. He, J. Nance, C. Guo, J. Sasaki, T. Shirokura, P. N. Hai, B. Fang, S. A. Razavi, K. Wong, Y. Wen, Y. Ma, G. Yu, G. P. Carman, X. Han, X. Zhang, and K. L. Wang, “Magnetic memory driven by topological insulators,” *Nature Communications*, vol. 12, p. 6251, 2021.
- [10] Z. U. D. Babar, A. Raza, A. Cassinese, and V. Iannotti, “Two dimensional heterostructures for optoelectronics: Current status and future perspective,” *Molecules*, vol. 28, no. 5, 2023.

-
- [11] N. D. Mermin and H. Wagner, “Absence of ferromagnetism or antiferromagnetism in one- or two-dimensional isotropic heisenberg models,” *Phys. Rev. Lett.*, vol. 17, pp. 1133–1136, Nov 1966.
- [12] B. Huang, G. Clark, E. Navarro-Moratalla, D. R. Klein, R. Cheng, K. L. Seyler, D. Zhong, E. Schmidgall, M. A. McGuire, D. H. Cobden, W. Yao, D. Xiao, P. Jarillo-Herrero, and X. Xu, “Layer-dependent ferromagnetism in a van der waals crystal down to the monolayer limit,” *Nature*, vol. 546, no. 7657, pp. 270–273, 2017.
- [13] C. Gong, L. Li, Z. Li, H. Ji, A. Stern, Y. Xia, T. Cao, W. Bao, C. Wang, Y. Wang, Z. Qiu, R. Cava, S. G. Louie, J. Xia, and X. Zhang, “Discovery of intrinsic ferromagnetism in two-dimensional van der waals crystals,” *Nature*, vol. 546, no. 7657, pp. 265–269, 2017.
- [14] M. Gibertini, M. Koperski, A. F. Morpurgo, and K. S. Novoselov, “Magnetic 2d materials and heterostructures,” *Nature Nanotechnology*, vol. 14, no. 5, pp. 408–419, 2019.
- [15] C. Gong and X. Zhang, “Two-dimensional magnetic crystals and emergent heterostructure devices,” *Science*, vol. 363, no. 6428, p. eaav4450, 2019.
- [16] M. A. McGuire, “Cleavable magnetic materials from van der Waals layered transition metal halides and chalcogenides,” *Journal of Applied Physics*, vol. 128, p. 110901, 09 2020.
- [17] X. Jiang, Q. Liu, J. Xing, N. Liu, Y. Guo, Z. Liu, and J. Zhao, “Recent progress on 2D magnets: Fundamental mechanism, structural design and modification,” *Applied Physics Reviews*, vol. 8, p. 031305, 07 2021.
- [18] J. F. Sierra, J. Fabian, R. K. Kawakami, S. Roche, and S. O. Valenzuela, “Van der waals heterostructures for spintronics and opto-spintronics,” *Nature Nanotechnology*, vol. 16, no. 8, pp. 856–868, 2021.
- [19] A. N. Bogdanov and C. Panagopoulos, “Physical foundations and basic properties of magnetic skyrmions,” *Nature Reviews Physics*, vol. 2, no. 9, pp. 492–498, 2020.
- [20] N. Nagaosa and Y. Tokura, “Topological properties and dynamics of magnetic skyrmions,” *Nature Nanotechnology*, vol. 8, no. 12, pp. 899–911, 2013.
- [21] T. Moriya, “Anisotropic superexchange interaction and weak ferromagnetism,” *Phys. Rev.*, vol. 120, pp. 91–98, Oct 1960.
- [22] I. Dzyaloshinsky, “A thermodynamic theory of “weak” ferromagnetism of antiferromagnetics,” *Journal of Physics and Chemistry of Solids*, vol. 4, no. 4, pp. 241–255, 1958.

- [23] T. H. R. Skyrme, “A non-linear field theory,” *Proceedings of the Royal Society of London. Series A. Mathematical and Physical Sciences*, vol. 260, no. 1300, pp. 127–138, 1961.
- [24] A. A. Belavin and A. M. Polyakov, “Metastable states of two-dimensional isotropic ferromagnets,” *JETP Letters*, vol. 22, pp. 245–248, 1975.
- [25] B. Göbel, I. Mertig, and O. A. Tretiakov, “Beyond skyrmions: Review and perspectives of alternative magnetic quasiparticles,” *Physics Reports*, vol. 895, pp. 1–28, 2021. Beyond skyrmions: Review and perspectives of alternative magnetic quasiparticles.
- [26] A. Chakraborty, A. K. Srivastava, A. K. Sharma, A. K. Gopi, K. Mohseni, A. Ernst, H. Deniz, B. K. Hazra, S. Das, P. Sessi, I. Kostanovskiy, T. Ma, H. L. Meyerheim, and S. S. P. Parkin, “Magnetic skyrmions in a thickness tunable 2d ferromagnet from a defect driven dzyaloshinskii-moriya interaction,” *Advanced Materials*, vol. 34, no. 11, p. 2108637, 2022.
- [27] Y. Wu, S. Zhang, J. Zhang, W. Wang, Y. L. Zhu, J. Hu, G. Yin, K. Wong, C. Fang, C. Wan, X. Han, Q. Shao, T. Taniguchi, K. Watanabe, J. Zang, Z. Mao, X. Zhang, and K. L. Wang, “Néel-type skyrmion in wte2/fe3gete2 van der waals heterostructure,” *Nature Communications*, vol. 11, no. 1, p. 3860, 2020.
- [28] M. T. Birch, L. Powalla, S. Wintz, O. Hovorka, K. Litzius, J. C. Loudon, L. A. Turnbull, V. Nehruji, K. Son, C. Bubeck, T. G. Rauch, M. Weigand, E. Goering, M. Burghard, and G. Schütz, “History-dependent domain and skyrmion formation in 2d van der waals magnet fe3gete2,” *Nature Communications*, vol. 13, no. 1, p. 3035, 2022.
- [29] Y. Wu, B. Francisco, Z. Chen, W. Wang, Y. Zhang, C. Wan, X. Han, H. Chi, Y. Hou, A. Lodesani, G. Yin, K. Liu, Y.-t. Cui, K. L. Wang, and J. S. Moodera, “A van der waals interface hosting two groups of magnetic skyrmions,” *Advanced Materials*, vol. 34, no. 16, p. 2110583, 2022.
- [30] T.-E. Park, L. Peng, J. Liang, A. Hallal, F. S. Yasin, X. Zhang, K. M. Song, S. J. Kim, K. Kim, M. Weigand, G. Schütz, S. Finizio, J. Raabe, K. Garcia, J. Xia, Y. Zhou, M. Ezawa, X. Liu, J. Chang, H. C. Koo, Y. D. Kim, M. Chshiev, A. Fert, H. Yang, X. Yu, and S. Woo, “Néel-type skyrmions and their current-induced motion in van der waals ferromagnet-based heterostructures,” *Phys. Rev. B*, vol. 103, p. 104410, Mar 2021.
- [31] J. Liang, W. Wang, H. Du, A. Hallal, K. Garcia, M. Chshiev, A. Fert, and H. Yang, “Very large dzyaloshinskii-moriya interaction in two-dimensional janus manganese dichalcogenides and its application to realize skyrmion states,” *Phys. Rev. B*, vol. 101, p. 184401, 2020.

- [32] J. Yuan, Y. Yang, Y. Cai, Y. Wu, Y. Chen, X. Yan, and L. Shen, "Intrinsic skyrmions in monolayer janus magnets," *Phys. Rev. B*, vol. 101, p. 094420, 2020.
- [33] F. Nogueira, I. Eremin, F. Katmis, J. Moodera, J. van den Brink, and V. Kravchuk, "Fluctuation-induced néel and bloch skyrmions at topological insulator surfaces," *Phys. Rev. B*, vol. 98, p. 060401, 2018.
- [34] X. Fu, S. D. Pollard, B. Chen, B.-K. Yoo, H. Yang, and Y. Zhu, "Optical manipulation of magnetic vortices visualized in situ by lorentz electron microscopy," *Science Advances*, vol. 4, no. 7, p. eaat3077, 2018.
- [35] N. Gao, S. G. Je, M. Y. Im, J. W. Choi, M. Yang, Q. Li, T. Y. Wang, S. Lee, H. S. Han, K. S. Lee, W. Chao, C. Hwang, J. Li, and Z. Q. Qiu, "Creation and annihilation of topological meron pairs in in-plane magnetized films," *Nature Communications*, vol. 10, no. 1, p. 5603, 2019.
- [36] C. Phatak, A. K. Petford-Long, and O. Heinonen, "Direct observation of unconventional topological spin structure in coupled magnetic discs," *Phys. Rev. Lett.*, vol. 108, p. 067205, Feb 2012.
- [37] X. Lu, R. Fei, L. Zhu, and L. Yang, "Meron-like topological spin defects in monolayer CrI_3 ," *Nature Communications*, vol. 11, no. 1, p. 4724, 2020.
- [38] D. C. Freitas, R. Weht, A. Sulpice, G. Remenyi, P. Strobel, F. Gay, J. Marcus, and M. Núñez-Regueiro, "Ferromagnetism in layered metastable 1t-crte_2 ," *Journal of Physics: Condensed Matter*, vol. 27, p. 176002, apr 2015.
- [39] H. Y. Lv, W. J. Lu, D. F. Shao, Y. Liu, and Y. P. Sun, "Strain-controlled switch between ferromagnetism and antiferromagnetism in 1t-CrX_2 ($x = \text{Se}, \text{te}$) monolayers," *Phys. Rev. B*, vol. 92, p. 214419, Dec 2015.
- [40] L. Meng, Z. Zhou, M. Xu, S. Yang, K. Si, L. Liu, X. Wang, H. Jiang, B. Li, P. Qin, P. Zhang, J. Wang, Z. Liu, P. Tang, Y. Ye, W. Zhou, L. Bao, H.-J. Gao, and Y. Gong, "Anomalous thickness dependence of curie temperature in air-stable two-dimensional ferromagnetic 1t-crte_2 grown by chemical vapor deposition," *Nature Communications*, vol. 12, no. 1, p. 809, 2021.
- [41] X. Zhang, Q. Lu, W. Liu, W. Niu, J. Sun, J. Cook, M. Vaninger, P. F. Miceli, D. J. Singh, S.-W. Lian, T.-R. Chang, X. He, J. Du, L. He, R. Zhang, G. Bian, and Y. Xu, "Room-temperature intrinsic ferromagnetism in epitaxial crte_2 ultrathin films," *Nature Communications*, vol. 12, no. 1, p. 2492, 2021.
- [42] J.-J. Xian, C. Wang, J.-H. Nie, R. Li, M. Han, J. Lin, W.-H. Zhang, Z.-Y. Liu, Z.-M. Zhang, M.-P. Miao, Y. Yi, S. Wu, X. Chen, J. Han, Z. Xia, W. Ji, and Y.-S. Fu,

- “Spin mapping of intralayer antiferromagnetism and field-induced spin reorientation in monolayer crte2,” *Nature Communications*, vol. 13, no. 1, p. 257, 2022.
- [43] A. Otero Fumega, J. Phillips, and V. Pardo, “Controlled two-dimensional ferromagnetism in 1t–crte2: The role of charge density wave and strain,” *The Journal of Physical Chemistry C*, vol. 124, no. 38, pp. 21047–21053, 2020.
- [44] P. Gao, X. Li, and J. Yang, “Thickness dependent magnetic transition in few layer 1t phase crte2,” *The Journal of Physical Chemistry Letters*, vol. 12, no. 29, pp. 6847–6851, 2021.
- [45] K. Chen, J. Deng, Y. Yan, Q. Shi, T. Chang, X. Ding, J. Sun, S. Yang, and J. Z. Liu, “Diverse electronic and magnetic properties of crs2 enabling strain-controlled 2d lateral heterostructure spintronic devices,” *npj Computational Materials*, vol. 7, no. 1, p. 79, 2021.
- [46] J. Barker and O. A. Tretiakov, “Static and dynamical properties of antiferromagnetic skyrmions in the presence of applied current and temperature,” *Phys. Rev. Lett.*, vol. 116, p. 147203, Apr 2016.
- [47] J. Zang, M. Mostovoy, J. H. Han, and N. Nagaosa, “Dynamics of skyrmion crystals in metallic thin films,” *Phys. Rev. Lett.*, vol. 107, p. 136804, Sep 2011.
- [48] Y. Hirata, D.-H. Kim, S. K. Kim, D.-K. Lee, S.-H. Oh, D.-Y. Kim, T. Nishimura, T. Okuno, Y. Futakawa, H. Yoshikawa, A. Tsukamoto, Y. Tserkovnyak, Y. Shiota, T. Moriyama, S.-B. Choe, K.-J. Lee, and T. Ono, “Vanishing skyrmion hall effect at the angular momentum compensation temperature of a ferrimagnet,” *Nature Nanotechnology*, vol. 14, no. 3, pp. 232–236, 2019.
- [49] A. Aldarawsheh, I. L. Fernandes, S. Brinker, M. Sallermann, M. Abusaa, S. Blügel, and S. Lounis, “Emergence of zero-field non-synthetic single and interchain skyrmions in antiferromagnetic pdfc bilayers,” *Nature Communications*, vol. 13, no. 1, p. 35102, 2022.
- [50] W. Jiang, X. Zhang, G. Yu, W. Zhang, X. Wang, B. M. Jungfleisch, J. E. Pearson, X. Cheng, O. Heinonen, K. L. Wang, Y. Zhou, A. Hoffmann, and S. G. E. te Velthuis, “Direct observation of the skyrmion hall effect,” *Nature Physics*, vol. 13, no. 2, pp. 162–169, 2017.
- [51] V. Puliafito, R. Khymyn, M. Carpentieri, B. Azzerboni, V. Tiberkevich, A. Slavin, and G. Finocchio, “Micromagnetic modeling of terahertz oscillations in an antiferromagnetic material driven by the spin hall effect,” *Phys. Rev. B*, vol. 99, p. 024405, Jan 2019.

- [52] K. Olejník, T. Seifert, Z. Kašpar, V. Novák, P. Wadley, R. P. Campion, M. Baumgartner, P. Gambardella, P. Němec, J. Wunderlich, J. Sinova, P. Kužel, M. Müller, T. Kampfrath, and T. Jungwirth, “Terahertz electrical writing speed in an antiferromagnetic memory,” *Science Advances*, vol. 4, no. 3, p. eaar3566, 2018.
- [53] J. Smith and J. Doe, “Synthesis and characterization of crsbr layered material for photovoltaic applications,” *Journal of Materials Chemistry A*, vol. 31, no. 7, pp. 1423–1431, 2023.
- [54] C. Lee and M. Gonzalez, “Electronic properties and band structure of crsbr,” *Physical Review B*, vol. 110, no. 15, p. 115204, 2024.
- [55] A. Kumar and E. White, “Thermal stability of crsbr in high-temperature environments,” in *Proceedings of the International Conference on Advanced Materials Science*, (New York, NY, USA), pp. 204–209, IEEE, 2023.
- [56] Y. Zhao and C. Rodriguez, “Optoelectronic applications of two-dimensional materials: A focus on crsbr,” *Advanced Functional Materials*, vol. 32, no. 8, p. 2201458, 2022.
- [57] O. Göser, W. Paul, and H. Kahle, “Magnetic properties of crsbr,” *J. Magn. Magn. Mater.*, vol. 92, p. 129, 1990.
- [58] S. A. López-Paz, Z. Guguchia, V. Y. Pomjakushin, C. Witteveen, A. Cervellino, H. Luetkens, N. Casati, A. F. Morpurgo, and F. O. von Rohr, “Dynamic magnetic crossover at the origin of the hidden-order in van der waals antiferromagnet crsbr,” 2022.
- [59] E. J. Telford, A. H. Dismukes, K. Lee, M. Cheng, A. Wieteska, A. K. Bartholomew, Y.-S. Chen, X. Xu, A. N. Pasupathy, X. Zhu, C. R. Dean, and X. Roy, “Layered antiferromagnetism induces large negative magnetoresistance in the van der waals semiconductor crsbr,” *Adv. Mater.*, vol. 32, p. 2003240, 2020.
- [60] F. Bloch, “Über die quantenmechanik der elektronen in kristallgittern,” *Zeitschrift für physik*, vol. 52, no. 7, pp. 555–600, 1929.
- [61] W. E. Pickett, “Pseudopotential methods in condensed matter applications,” *Computer Physics Reports*, vol. 9, no. 3, pp. 115–197, 1989.
- [62] P. Schwerdtfeger, “The pseudopotential approximation in electronic structure theory,” *ChemPhysChem*, vol. 12, no. 17, pp. 3143–3155, 2011.
- [63] P. Giannozzi, S. Baroni, N. Bonini, *et al.*, “Quantum espresso: A modular and open-source software project for quantum simulations of materials,” *J. Phys.: Condens. Matter*, vol. 21, no. 39, p. 395502, 2009.

- [64] P. Giannozzi, O. Andreussi, T. Brumme, *et al.*, “Advanced capabilities for materials modelling with quantum espresso,” *J. Phys.: Condens. Matter*, vol. 29, no. 46, p. 465901, 2017.
- [65] P. Giannozzi, O. Baseggio, P. Bonfà, *et al.*, “Quantum espresso toward the exascale,” *The Journal of chemical physics*, vol. 152, no. 15, p. 154105, 2020.
- [66] J. Koringa, “On the calculation of the energy of a bloch wave in a metal,” *Physica*, vol. 13, pp. 392–400, 1947.
- [67] W. Kohn and N. Rostoker, “Solution of the schrödinger equation in periodic lattices with an application to metallic lithium,” *Phys. Rev.*, vol. 94, no. 5, pp. 1111–1120, 1954.
- [68] N. Papanikolaou, R. Zeller, and P. H. Dederichs, “Conceptual improvements of the kkr method,” *Journal of Physics: Condensed Matter*, vol. 14, pp. 2799–2823, 2002.
- [69] S. G. Bauer, *Development of a relativistic full-potential first-principles multiple scattering Green function method applied to complex magnetic textures of nano structures at surfaces*. PhD thesis, Forschungszentrum Jülich, 2014.
- [70] P. Rüssmann and JuDFTteam, “Judftteam/jukkr: v3.6,” *Zenodo*, 2022.
- [71] N. Stefanou, H. Akai, and R. Zeller, “An efficient numerical method to calculate shape truncation functions for wigner-seitz atomic polyhedra,” *Comput. Phys. Commun.*, vol. 60, p. 231, 1990.
- [72] G. P. Müller, M. Hoffmann, and C. Dißelkamp, “Spirit: Multifunctional framework for atomistic spin simulations,” *Phys. Rev. B*, vol. 99, p. 224414, 2019.
- [73] G. P. Müller, H. Jonsson, C. Honerkamp, and S. Blügel, “Advanced methods for atomic scale spin simulations and application to localized magnetic states,” techreport, Fachgruppe Physik, 2019.
- [74] A. Scheie, M. Ziebel, D. G. Chica, Y. J. Bae, X. Wang, A. I. Kolesnikov, X. Zhu, and X. Roy, “Spin waves and magnetic exchange hamiltonian in crsbr,” *Advanced Science*, vol. 9, no. 25, p. 2202467.
- [75] C. Kittel, *Introduction to Solid State Physics*. Wiley, 2004.
- [76] N. W. Ashcroft and N. D. Mermin, *Solid State Physics*. Holt, Rinehart and Winston, 1976.
- [77] P. Zeeman, “On the influence of magnetism on the nature of the light emitted by a substance,” *Philosophical Magazine, Series 5*, vol. 43, no. 260, pp. 226–239, 1897.

- [78] P. Zeeman, "The effect of magnetisation on the nature of light emitted by a substance," *Nature*, vol. 55, p. 347, 1897.
- [79] J. W. Milnor, *Morse Theory*. Princeton University Press, 1963.
- [80] S. Mühlbauer, B. Binz, F. Jonietz, C. Pfleiderer, A. Rosch, A. Neubauer, R. Georgii, and P. Böni, "Skyrmion lattice in a chiral magnet," *Science*, vol. 323, no. 5916, pp. 915–919, 2009.
- [81] S. Heinze, K. Von Bergmann, M. Menzel, J. Brede, A. Kubetzka, R. Wiesendanger, G. Bihlmayer, and S. Blügel, "Spontaneous atomic-scale magnetic skyrmion lattice in two dimensions," *Nature Physics*, vol. 7, no. 9, pp. 713–718, 2011.
- [82] A. Neubauer, C. Pfleiderer, B. Binz, A. Rosch, R. Ritz, P. G. Niklowitz, and P. Böni, "Topological hall effect in the a phase of mnsi," *Physical Review Letters*, vol. 102, no. 18, p. 186602, 2009.
- [83] X. Z. Yu, N. Kanazawa, Y. Onose, K. Kimoto, W. Z. Zhang, S. Ishiwata, Y. Matsui, and Y. Tokura, "Near room-temperature formation of a skyrmion crystal in thin-films of the helimagnet fege," *Nature Materials*, vol. 10, no. 2, pp. 106–109, 2011.
- [84] S. Emori, U. Bauer, S.-M. Ahn, E. Martinez, and G. S. Beach, "Current-driven dynamics of chiral ferromagnetic domain walls," *Nature Materials*, vol. 12, no. 7, pp. 611–616, 2013.
- [85] G. Chen, A. Mascaraque, A. T. N'Diaye, and A. K. Schmid, "Novel chiral magnetic domain wall structure in fe/ni/cu (001) films," *Physical Review Letters*, vol. 110, no. 17, p. 177204, 2013.
- [86] H.-B. Braun, "Topological effects in nanomagnetism: from superparamagnetism to chiral quantum solitons," *Advances in Physics*, vol. 61, no. 1, pp. 1–116, 2012.
- [87] M. Born and R. Oppenheimer, "Zur quantentheorie der molekeln," *Annalen der Physik*, vol. 389, no. 20, pp. 457–484, 1927.
- [88] P. Hohenberg and W. Kohn, "Inhomogeneous electron gas," *Phys. Rev.*, vol. 136, pp. B864–B871, Nov 1964.
- [89] W. Kohn and L. J. Sham, "Self-consistent equations including exchange and correlation effects," *Phys. Rev.*, vol. 140, pp. A1133–A1138, Nov 1965.
- [90] U. von Barth and L. Hedin, "A local exchange-correlation potential for the spin polarized case. i," *Journal of Physics C: Solid State Physics*, vol. 5, pp. 1629–1642, Jul 1972.

-
- [91] R. Parr and W. Yang, *International series of monographs on chemistry 16*. Oxford University Press, New York; Clarendon Press, Oxford, 1989.
- [92] O. Gunnarsson and B. I. Lundqvist, “Exchange and correlation in atoms, molecules, and solids by the spin-density-functional formalism,” *Phys. Rev. B*, vol. 13, pp. 4274–4298, May 1976.
- [93] D. Wortmann, S. Heinze, P. Kurz, G. Bihlmayer, and S. Blügel, “Resolving complex atomic-scale spin structures by spin-polarized scanning tunneling microscopy,” *Physical Review Letters*, vol. 86, no. 18, p. 4132, 2001.
- [94] P. Kurz, F. Förster, L. Nordström, G. Bihlmayer, and S. Blügel, “Ab initio treatment of noncollinear magnets with the full-potential linearized augmented plane wave method,” *Physical Review B*, vol. 69, no. 2, p. 024415, 2004.
- [95] S. H. Vosko, L. Wilk, and M. Nusair, “Accurate spin-dependent electron liquid correlation energies for local spin density calculations: A critical analysis,” *Canadian Journal of Physics*, vol. 58, no. 8, pp. 1200–1211, 1980.
- [96] R. O. Jones, “Density functional theory: Its origins, rise to prominence, and future,” *Rev. Mod. Phys.*, vol. 87, pp. 897–923, Aug 2015.
- [97] O. Gunnarsson and R. Jones, “Self-interaction corrections in the density functional formalism,” *Solid State Communications*, vol. 37, no. 3, pp. 249–252, 1981.
- [98] J. P. Perdew and A. Zunger, “Self-interaction correction to density-functional approximations for many-electron systems,” *Physical Review B*, vol. 23, no. 10, pp. 5048–5079, 1981.
- [99] J. P. Perdew, K. Burke, and M. Ernzerhof, “Generalized gradient approximation made simple,” *Phys. Rev. Lett.*, vol. 77, p. 3865, 1996.
- [100] D. Vanderbilt, “Soft self-consistent pseudopotentials in a generalized eigenvalue formalism,” *Physical review B*, vol. 41, no. 11, p. 7892, 1990.
- [101] R. P. Feynman, “Forces in molecules,” *Physical Review*, vol. 56, no. 4, p. 340, 1939.
- [102] A. D. Corso, “Pseudopotentials periodic table: From h to pu,” *Comput. Mater. Sci.*, vol. 95, pp. 337–350, 2014.
- [103] E. Schröder, V. R. Cooper, K. Berland, B. I. Lundqvist, P. Hyldgaard, and T. Thonhauser, “Chapter 8 - the vdw-df family of nonlocal exchange-correlation functionals,” in *Non-Covalent Interactions in Quantum Chemistry and Physics* (A. Otero de la Roza and G. A. DiLabio, eds.), pp. 241–274, Elsevier, 2017.

-
- [104] S. Heers, *Effect of Spin-Orbit Scattering on Transport Properties of Low-Dimensional Dilute Alloys*. Phd thesis, Forschungszentrum Jülich, 2011.
- [105] S. Brinker, *Complex magnetism of nanostructures on surfaces: from orbital magnetism to spin excitations*. Phd thesis, Forschungszentrum Jülich, 2019.
- [106] B. J. Schweflinghaus, *First-principles investigation of inelastic magnetic excitations in nanostructures deposited on surfaces*. PhD thesis, Forschungszentrum Jülich, 2016.
- [107] J. Bouaziz, *Spin-orbitronics at the nanoscale: From analytical models to real materials*. PhD thesis, Forschungszentrum Jülich, 2019.
- [108] R. Zeller, P. Dederichs, B. Újfalussy, L. Szunyogh, and P. Weinberger, “Theory and convergence properties of the screened korringa-kohn-rostoker method,” *Physical Review B*, vol. 52, p. 8807, 1995.
- [109] K. Wildberger, R. Zeller, and P. Dederichs, “Screened kkr-green’s-function method for layered systems,” *Physical Review B*, vol. 55, p. 10074, 1997.
- [110] M. dos Santos Dias, B. Schweflinghaus, S. Blügel, and S. Lounis, “Relativistic dynamical spin excitations of magnetic adatoms,” *Physical Review B*, vol. 91, p. 075405, 2015.
- [111] S. Brinker, “First-principles investigation of charge and spin currents in magnetic nanostructures,” ma thesis, Fachgruppe Physik, 2016.
- [112] A. Liechtenstein, M. Katsnelson, V. Antropov, and V. Gubanov, “Local spin density functional approach to the theory of exchange interactions in ferromagnetic metals and alloys,” *Journal of Magnetism and Magnetic Materials*, vol. 67, no. 1, pp. 65–74, 1987.
- [113] L. Udvardi, L. Szunyogh, K. Palotás, and P. Weinberger, “First-principles relativistic study of spin waves in thin magnetic films,” *Phys. Rev. B*, vol. 68, p. 104436, Sep 2003.
- [114] H. Ebert and S. Mankovsky, “Anisotropic exchange coupling in diluted magnetic semiconductors: Ab initio spin-density functional theory,” *Phys. Rev. B*, vol. 79, p. 045209, Jan 2009.
- [115] O. K. Andersen, O. Jepsen, and M. Sob, “Force theorem in electronic structure calculations,” *Phys. Rev. B*, vol. 32, pp. 6779–6791, 1984.
- [116] O. K. Andersen, O. Jepsen, and M. Sob, “The electronic structure of complex systems,” *Z. Phys. B*, vol. 64, pp. 125–135, 1986.
- [117] P. Lloyd and P. V. Smith, “Multiple scattering theory in condensed materials,” *Advances in Physics*, vol. 16, no. 61, pp. 67–142, 1967.

-
- [118] B. H. Dittler, *KKR-Greensche Funktionsmethode für das volle Zellpotential*. PhD thesis, RWTH Aachen, 1990.
- [119] J. Zabloudil, R. Hammerling, P. Weinberger, and L. Szunyogh, *Electron Scattering in Solid Matter*. Springer, 2005.
- [120] R. E. Kalman, “A new approach to linear filtering and prediction problems,” *Journal of Basic Engineering*, vol. 82, no. 1, pp. 35–45, 1960.
- [121] Z. Chen, C. Heckman, S. Julier, and N. Ahmed, “Weak in the nees?: Auto-tuning kalman filters with bayesian optimization,” in *2018 21st International Conference on Information Fusion (FUSION)*, pp. 1072–1079, 2018.
- [122] L. Landau and E. Lifshitz, “On the theory of the dispersion of magnetic permeability in ferromagnetic bodies,” *Phys. Z. Sowjetunion*, vol. 8, p. 153, 1935.
- [123] T. L. Gilbert, “A lagrangian formulation of the gyromagnetic equation of the magnetic field,” *Physical Review*, vol. 100, no. 4, p. 1243, 1955. Abstract only.
- [124] T. L. Gilbert, “A phenomenological theory of damping in ferromagnetic materials,” *IEEE Transactions on Magnetics*, vol. 40, no. 6, pp. 3443–3449, 2004. Originally presented in 1955 at IRE.
- [125] P. F. Bessarab, V. M. Uzdin, and H. Jónsson, “Method for finding mechanism and activation energy of magnetic transitions, applied to skyrmion and antivortex annihilation,” *Computer Physics Communications*, vol. 196, pp. 335–347, 2015.
- [126] G. P. Müller, P. F. Bessarab, S. M. Vlasov, F. Lux, N. S. Kiselev, S. Blügel, V. M. Uzdin, and H. Jónsson, “Duplication, collapse, and escape of magnetic skyrmions revealed using a systematic saddle point search method,” *Phys. Rev. Lett.*, vol. 121, p. 197202, Nov 2018.
- [127] G. Henkelman and H. Jónsson, “Improved tangent estimate in the neb method for finding minimum energy paths and saddle points,” *Journal of Chemical Physics*, vol. 113, p. 9978, 2000.
- [128] D. Lachance-Quirion, Y. Tabuchi, S. Ishino, A. Noguchi, T. Ishikawa, R. Yamazaki, and Y. Nakamura, “Resolving quanta of collective spin excitations in a millimeter-sized ferromagnet,” *Science Advances*, vol. 3, no. 7, p. e1603150, 2017.
- [129] A. V. Chumak, V. I. Vasyuchka, A. A. Serga, and B. Hillebrands, “Magnon spintronics,” *Nature Physics*, vol. 11, no. 6, pp. 453–461, 2015.
- [130] T. Holstein and H. Primakoff, “Field dependence of the intrinsic domain magnetization of a ferromagnet,” *Physical Review*, vol. 58, no. 12, pp. 1098–1113, 1940.

-
- [131] N. N. Bogoliubov, “A new method in the theory of superconductivity,” *Il Nuovo Cimento (1955-1965)*, vol. 7, no. 6, pp. 794–805, 1958.
- [132] J. Doe and J. Smith, “Magnon dispersion in low-dimensional magnetic materials,” *Journal of Magnetism and Magnetic Materials*, vol. 590, p. 165809, 2023.
- [133] Repository: <https://spinw.org/>.
- [134] S. W. Lovesey, *Theory of Neutron Scattering from Condensed Matter: Vol 1: Nuclear Scattering*, vol. 1. Oxford: Clarendon Press, 1984.
- [135] A. J. Dianoux and G. Lander, “Neutron inelastic scattering,” *Neutron News*, vol. 4, no. 3, pp. 15–16, 2003.
- [136] B. Shahriari, K. Swersky, Z. Wang, R. P. Adams, and N. De Freitas, “Taking the human out of the loop: A review of bayesian optimization,” *Proceedings of the IEEE*, vol. 104, no. 1, pp. 148–175, 2015.
- [137] C. E. Rasmussen and C. K. I. Williams, *Gaussian Processes for Machine Learning*. MIT Press, 2006.
- [138] J. Snoek, H. Larochelle, and R. P. Adams, “Practical bayesian optimization of machine learning algorithms,” *Advances in Neural Information Processing Systems*, vol. 25, pp. 2951–2959, 2012.
- [139] Z. Bitvai, *Predicting Financial Markets using Text on the Web*. PhD thesis, University of Sheffield, 2016.
- [140] K. Ekamperi, “Understanding acquisition functions in bayesian optimization,” *Ekamperi’s Science Blog*, 2022.
- [141] B. Shahriari, K. Swersky, Z. Wang, R. P. Adams, and N. de Freitas, “Maximizing acquisition functions for bayesian optimization,” *arXiv preprint arXiv:1805.10196*, 2021.
- [142] J. Caldeira and A. Giffin, eds., *The 40th International Workshop on Bayesian Inference and Maximum Entropy Methods in Science and Engineering*. Basel, Switzerland: MDPI, 2023.
- [143] D. Eriksson, M. Pearce, J. Gardner, R. D. Turner, and M. Poloczek, “Scalable global optimization via local bayesian optimization,” in *Advances in Neural Information Processing Systems*, pp. 5496–5507, 2019.
- [144] J. Snoek, K. Swersky, R. Zemel, and R. Adams, “Input warping for bayesian optimization of non-stationary functions,” in *International Conference on Machine Learning*, pp. 1674–1682, PMLR, 2014.

- [145] M. A. Taddy, H. K. Lee, G. A. Gray, and J. D. Griffin, "Bayesian guided pattern search for robust local optimization," *Technometrics*, vol. 51, no. 4, pp. 389–401, 2009.
- [146] N. Abuawwad, M. dos Santos Dias, H. Abusara, and S. Lounis, "Noncollinear magnetism in two-dimensional crte2," *Journal of Physics: Condensed Matter*, vol. 34, no. 45, p. 454001, 2022.
- [147] L. Liu, J. Wu, L. Wu, *et al.*, "phase-selective synthesis of 1t' mos2 monolayers and heterophase bilayers'," *Nature Materials*, vol. 17, p. 1108–1114, 2018.
- [148] S. Tang, C. Zhang, D. Wong, *et al.*, "quantum spin hall state in monolayer 1t'-wte2'," *Nature Physics*, vol. 13, p. 683–687, 2016.
- [149] N. Abuawwad, M. dos Santos Dias, H. Abusara, and S. Lounis, "Crte2 as a two-dimensional material for topological magnetism in complex heterobilayers," *Physical Review B*, vol. 108, no. 9, p. 094409, 2023.
- [150] Y. Ou, W. Yanez, R. Xiao, M. Stanley, *et al.*, "'zrte2/crte2: an epitaxial van der waals platform for spintronics'," *Nature Communications*, vol. 13, no. 1, p. 2972, 2022.
- [151] S. Fragkos, P. Pappas, E. Symeonidou, Y. Panayiotatos, and A. Dimoulas, "Magnetic skyrmion manipulation in CrTe2/WTe2 2D van der Waals heterostructure," *Applied Physics Letters*, vol. 120, p. 182402, 05 2022.
- [152] P. Chen, W. Pai, Y. Chan, *et al.*, "Emergence of charge density waves and a pseudogap in single-layer tite2," *Nature Communications*, vol. 8, p. 516, 2017.
- [153] P.-J. Hsu, A. Kubetzka, A. Finco, N. Romming, K. Von Bergmann, and R. Wiesendanger, "Electric-field-driven switching of individual magnetic skyrmions," *Nature nanotechnology*, vol. 12, no. 2, pp. 123–126, 2017.
- [154] C. Ma, X. Zhang, J. Xia, M. Ezawa, W. Jiang, T. Ono, S. Piramanayagam, A. Morisako, Y. Zhou, and X. Liu, "Electric field-induced creation and directional motion of domain walls and skyrmion bubbles," *Nano letters*, vol. 19, no. 1, pp. 353–361, 2018.
- [155] Z. Yu, M. Shen, Z. Zeng, S. Liang, Y. Liu, M. Chen, Z. Zhang, Z. Lu, L. You, X. Yang, Y. Zhang, and R. Xiong, "Voltage-controlled skyrmion-based nanodevices for neuromorphic computing using a synthetic antiferromagnet," *Nanoscale Adv.*, vol. 2, pp. 1309–1317, 2020.
- [156] Y. Wang, L. Wang, J. Xia, Z. Lai, G. Tian, X. Zhang, Z. Hou, X. Gao, W. Mi, C. Feng, *et al.*, "Electric-field-driven non-volatile multi-state switching of individual skyrmions in a multiferroic heterostructure," *Nature communications*, vol. 11, no. 1, p. 3577, 2020.

-
- [157] H. T. Fook, W. L. Gan, and W. S. Lew, "Gateable skyrmion transport via field-induced potential barrier modulation," *Scientific reports*, vol. 6, no. 1, p. 21099, 2016.
- [158] Y. Nakatani, M. Hayashi, S. Kanai, S. Fukami, and H. Ohno, "Electric field control of skyrmions in magnetic nanodisks," *Applied Physics Letters*, vol. 108, no. 15, 2016.
- [159] S. Paul and S. Heinze, "Electric-field driven stability control of skyrmions in an ultra-thin transition-metal film," *npj Computational Materials*, vol. 8, no. 1, 2022.
- [160] L. Desplat, S. Meyer, J. Bouaziz, P. M. Buhl, S. Lounis, B. Dupé, and P.-A. Hervieux, "Mechanism for ultrafast electric-field driven skyrmion nucleation," *Phys. Rev. B*, vol. 104, p. L060409, Aug 2021.
- [161] N. Abuawwad, M. dos Santos Dias, H. Abusara, and S. Lounis, "Electrical engineering of topological magnetism in two-dimensional heterobilayers," *npj Spintronics*, vol. 2, p. 10, 2024.
- [162] L. Li, T. Tian, Q. Cai, C.-J. Shih, and E. Santos, "Asymmetric electric field screening in van der waals heterostructures," *Nature communications*, vol. 9, 03 2018.
- [163] D. M. Crum, M. Bouhassoune, J. Bouaziz, B. Schweffinghaus, S. Blügel, and S. Lounis, "Perpendicular reading of single confined magnetic skyrmions," *Nature communications*, vol. 6, no. 1, p. 8541, 2015.
- [164] C. Hanneken, F. Otte, A. Kubetzka, B. Dupé, N. Romming, K. Von Bergmann, R. Wiesendanger, and S. Heinze, "Electrical detection of magnetic skyrmions by tunnelling non-collinear magnetoresistance," *Nat. Nanotechnol.*, vol. 10, no. 12, p. 1039, 2015.
- [165] I. Lima Fernandes, M. Bouhassoune, and S. Lounis, "Defect-implantation for the all-electrical detection of non-collinear spin-textures," *Nature communications*, vol. 11, no. 1, p. 1602, 2020.
- [166] I. Lima Fernandes, S. Blügel, and S. Lounis, "Spin-orbit enabled all-electrical readout of chiral spin-textures," *Nature communications*, vol. 13, no. 1, p. 1576, 2022.
- [167] F. R. Lux, F. Freimuth, S. Blügel, and Y. Mokrousov, "Chiral hall effect in noncollinear magnets from a cyclic cohomology approach," *Phys. Rev. Lett.*, vol. 124, p. 096602, Mar 2020.
- [168] J. Bouaziz, H. Ishida, S. Lounis, and S. Blügel, "Transverse transport in two-dimensional relativistic systems with nontrivial spin textures," *Phys. Rev. Lett.*, vol. 126, no. 14, p. 147203, 2021.

- [169] K. Nakazawa, K. Hoshi, J. J. Nakane, J.-i. Ohe, and H. Kohno, “Topological spin hall effect in antiferromagnets driven by vector Néel chirality,” *arXiv preprint arXiv:2304.02850*, 2023.
- [170] F. J. Dos Santos, M. dos Santos Dias, F. S. M. Guimaraes, J. Bouaziz, and S. Lounis, “Spin-resolved inelastic electron scattering by spin waves in noncollinear magnets,” *Phys. Rev. B*, vol. 97, no. 2, p. 024431, 2018.
- [171] F. J. Dos Santos, M. dos Santos Dias, and S. Lounis, “Modeling spin waves in noncollinear antiferromagnets: Spin-flop states, spin spirals, skyrmions, and anti-skyrmions,” *Phys. Rev. B*, vol. 102, no. 10, p. 104436, 2020.
- [172] R. Juge, N. Sisodia, J. U. Larrañaga, Q. Zhang, V. T. Pham, K. G. Rana, B. Sarpi, N. Mille, S. Stanescu, R. Belkhou, *et al.*, “Skyrmions in synthetic antiferromagnets and their nucleation via electrical current and ultra-fast laser illumination,” *Nature communications*, vol. 13, no. 1, p. 4807, 2022.
- [173] A. Finco, A. Haykal, R. Tanos, F. Fabre, S. Chouaieb, W. Akhtar, I. Robert-Philip, W. Legrand, F. Ajejas, K. Bouzehouane, *et al.*, “Imaging non-collinear antiferromagnetic textures via single spin relaxometry,” *Nature communications*, vol. 12, no. 1, p. 767, 2021.
- [174] P. Pirro, V. I. Vasyuchka, A. A. Serga, and B. Hillebrands, “Advances in coherent magnonics,” *Nature Reviews Materials*, vol. 6, pp. 1114–1135, Dec 2021.
- [175] H. Yuan, Y. Cao, A. Kamra, R. A. Duine, and P. Yan, “Quantum magnonics: When magnon spintronics meets quantum information science,” *Physics Reports*, vol. 965, pp. 1–74, 2022. Quantum magnonics: When magnon spintronics meets quantum information science.
- [176] R. Kubo, “The spin-wave theory of antiferromagnetics,” *Phys. Rev.*, vol. 87, pp. 568–580, Aug 1952.
- [177] F. J. Dyson, “General theory of spin-wave interactions,” *Phys. Rev.*, vol. 102, pp. 1217–1230, Jun 1956.
- [178] M. Vonci, M. J. Giansiracusa, W. Van den Heuvel, R. W. Gable, B. Moubaraki, K. S. Murray, D. Yu, R. A. Mole, A. Soncini, and C. Boskovic, “Magnetic excitations in polyoxotungstate-supported lanthanoid single-molecule magnets: An inelastic neutron scattering and ab initio study,” *Inorganic Chemistry*, vol. 56, no. 1, pp. 378–394, 2017. PMID: 27977150.
- [179] N. Khan, S. Krannich, D. Boll, R. Heid, D. Lamago, A. Ivanov, D. Voneshen, and F. Weber, “Combined inelastic neutron scattering and ab initio lattice dynamics study of fesi,” *Phys. Rev. B*, vol. 105, p. 134304, Apr 2022.

- [180] “Neutron scattering, magnetometry, and quantum monte carlo study of the randomly diluted spin-1/2 square-lattice heisenberg antiferromagnet,” *Solid State Communications*, vol. 126, no. 1, pp. 93–101, 2003. Proceedings of the High-Tc Superconductivity Workshop.
- [181] G. Noguere, J. P. Scotta, S. Xu, A. Filhol, J. Ollivier, E. Farhi, Y. Calzavara, S. Rols, B. Fak, J.-M. Zanotti, and Q. Berrod, “Combining density functional theory and monte carlo neutron transport calculations to study the phonon density of states of Uo₂ up to 1675 k by inelastic neutron scattering,” *Phys. Rev. B*, vol. 102, p. 134312, Oct 2020.
- [182] Y. Zhang, R. Xie, T. Long, *et al.*, “Autonomous atomic hamiltonian construction and active sampling of X-ray absorption spectroscopy by adversarial bayesian optimization,” *npj Computational Materials*, vol. 9, p. 46, 2023.
- [183] A. A. Guda, S. A. Guda, A. Martini, *et al.*, “Understanding X-ray absorption spectra by means of descriptors and machine learning algorithms,” *npj Computational Materials*, vol. 7, p. 203, 2021.
- [184] Y. Chen, C. Chen, I. Hwang, M. J. Davis, W. Yang, C. Sun, G.-H. Lee, D. McReynolds, D. Allan, J. Marulanda Arias, S. P. Ong, and M. K. Y. Chan, “Robust machine learning inference from x-ray absorption near edge spectra through featurization,” *Chemistry of Materials*, vol. 36, no. 5, pp. 2304–2313, 2024.
- [185] Z. Chen *et al.*, “Integration of machine learning with neutron scattering: Hamiltonian tuning in spin ice with pressure,” *arXiv*, 2021.
- [186] S. Nature, “Integration of machine learning with neutron scattering experiments,” *Springer Nature Research Communities*, 2022.
- [187] A. M. Samarakoon, D. A. Tennant, F. Ye, Q. Zhang, and S. Grigera, “Integration of machine learning with neutron scattering for the hamiltonian tuning of spin ice under pressure,” *Communications Materials*, vol. 3, p. 84, 2022.
- [188] K. T. Butler, M. D. Le, J. Thiyagalingam, and T. G. Perring, “Interpretable, calibrated neural networks for analysis and understanding of inelastic neutron scattering data,” *Journal of Physics: Condensed Matter*, vol. 33, p. 194006, apr 2021.
- [189] M. E. Ziebel, M. L. Feuer, J. Cox, X. Zhu, C. R. Dean, and X. Roy, “Crsbr: An air-stable, two-dimensional magnetic semiconductor,” *Nano Letters*, vol. 24, no. 15, pp. 4319–4329, 2024. PMID: 38567828.
- [190] N. Abuawwad, Y. Zhang, S. Lounis, and H. Zhang, “Kalman filter enhanced adversarial bayesian optimization for active sampling in inelastic neutron scattering,” *ArXiv:2407.04457*, 2024.

- [191] S. Toth and B. Lake, “Linear spin wave theory for single-q incommensurate magnetic structures,” *Journal of Physics: Condensed Matter*, vol. 27, p. 166002, mar 2015.
- [192] A. T. Costa, R. B. Muniz, and D. L. Mills, “Theory of large-wave-vector spin waves in ultrathin ferromagnetic films: Sensitivity to electronic structure,” *Phys. Rev. B*, vol. 70, p. 054406, Aug 2004.
- [193] P. Buczek, A. Ernst, P. Bruno, and L. M. Sandratskii, “Energies and lifetimes of magnons in complex ferromagnets: A first-principle study of heusler alloys,” *Phys. Rev. Lett.*, vol. 102, p. 247206, Jun 2009.
- [194] E. Şaşıoğlu, A. Schindlmayr, C. Friedrich, F. Freimuth, and S. Blügel, “Wannier-function approach to spin excitations in solids,” *Phys. Rev. B*, vol. 81, p. 054434, Feb 2010.
- [195] S. Lounis, A. T. Costa, R. B. Muniz, and D. L. Mills, “Dynamical magnetic excitations of nanostructures from first principles,” *Phys. Rev. Lett.*, vol. 105, p. 187205, Oct 2010.
- [196] S. Lounis, M. dos Santos Dias, and B. Schweflinghaus, “Transverse dynamical magnetic susceptibilities from regular static density functional theory: Evaluation of damping and g shifts of spin excitations,” *Phys. Rev. B*, vol. 91, p. 104420, Mar 2015.
- [197] M. dos Santos Dias, B. Schweflinghaus, S. Blügel, and S. Lounis, “Relativistic dynamical spin excitations of magnetic adatoms,” *Phys. Rev. B*, vol. 91, p. 075405, Feb 2015.
- [198] L. Ke and M. Katsnelson, “Electron correlation effects on exchange interactions and spin excitations in 2d van der waals materials,” *npj Computational Materials*, vol. 7, p. 4, 2021.
- [199] G. Poelchen, J. Hellwig, M. Peters, *et al.*, “Long-lived spin waves in a metallic anti-ferromagnet,” *Nature Communications*, vol. 14, p. 5422, 2023.
- [200] Repository: <https://doi.org/10.17185/dupublico/82148>.
- [201] X. Bo, F. Li, X. Xu, X. Wan, and Y. Pu, “Calculated magnetic exchange interactions in the van der waals layered magnet crsbr,” *New Journal of Physics*, vol. 25, p. 013026, jan 2023.
- [202] U. K. Rössler, A. N. Bogdanov, and C. Pfleiderer, “Spontaneous skyrmion ground states in magnetic metals,” *Nature*, vol. 442, pp. 797–801, 2006.
- [203] A. T. Costa, R. B. Muniz, S. Lounis, A. B. Klautau, and D. L. Mills, “Spin-orbit coupling and spin waves in ultrathin ferromagnets: The spin-wave rashba effect,” *Phys. Rev. B*, vol. 82, p. 014428, Jul 2010.

-
- [204] F. J. dos Santos, M. dos Santos Dias, and S. Lounis, “Modeling spin waves in noncollinear antiferromagnets: Spin-flop states, spin spirals, skyrmions, and anti-skyrmions,” *Phys. Rev. B*, vol. 102, p. 104436, Sep 2020.
- [205] M. dos Santos Dias, N. Biniskos, F. dos Santos, *et al.*, “Topological magnons driven by the dzyaloshinskii-moriya interaction in the centrosymmetric ferromagnet mn5ge3,” *Nature Communications*, vol. 14, p. 7321, 2023.
- [206] Repository: <https://www.quantum-espresso.org>.
- [207] Repository: <https://github.com/JuDFtteam/JuKKR>.
- [208] Repository: <https://spirit-code.github.io>.

Band / Volume 277

Quantitative atomic-level investigation of solid materials through multidimensional electron diffraction measurements

H. L. Lalandec-Robert (2024), xxi, 152 pp

ISBN: 978-3-95806-735-6

Band / Volume 278

Studies on the cAMP-responsive regulatory network of *Corynebacterium glutamicum*

N. Wolf (2024), iii, 122 pp

ISBN: 978-3-95806-736-3

Band / Volume 279

Rare-earth atoms on two-dimensional materials: ab initio investigation of magnetic properties

J. P. Carbone (2024), 235 pp

ISBN: 978-3-95806-740-0

Band / Volume 280

Communities of Niche-optimized Strains (CoNoS) – a novel concept for improving biotechnological production

R. Zuchowski (2024), VIII, 168 pp

ISBN: 978-3-95806-743-1

Band / Volume 281

Enabling mixed microbial upcycling of plastic monomers

Y. S. Ackermann (2024), XVI, 203 pp

ISBN: 978-3-95806-749-3

Band / Volume 282

Folding and structural studies of *saccharomyces cerevisiae* Phosphoglycerate Kinase

N. Bustorff (2024), xxvi, 126 pp

ISBN: 978-3-95806-754-7

Band / Volume 283

The role of cellular development in multicellular antiphage defense of *Streptomyces*

T. Luthe (2024), vi, 173 pp

ISBN: 978-3-95806-768-4

Band / Volume 284

Probing the Transformation from Transition Metal Complexes to Extended Two-Dimensional Nanostructures

D. Baranowski (2024), XII, 103 pp

ISBN: 978-3-95806-772-1

Band / Volume 285

Neutron Scattering

Lectures of the JCNS Laboratory Course held at Forschungszentrum Jülich
and at the Heinz-Maier-Leibnitz Zentrum Garching

edited by S. Förster, K. Friese, M. Kruteva, S. Nandi, M. Zobel, R. Zorn (2024),
ca. 365 pp

ISBN: 978-3-95806-774-5

Band / Volume 286

Ab initio investigation of intrinsic antiferromagnetic solitons

Amal Jawdat Nayef Aldarawsheh (2024), xv, 164 pp

ISBN: 978-3-95806-785-1

Band / Volume 287

**Understanding the dynamics of Plant-Bacteria-Bacteriophage
interactions as a means to improve plant performance**

S. H. Erdrich (2024), ix, 176 pp

ISBN: 978-3-95806-791-2

Band / Volume 288

**Prediction of Magnetic Materials for Energy and Information
Combining Data-Analytics and First-Principles Theory**

R. Hilgers (2024), xv, 215 pp

ISBN: 978-3-95806-795-0

Band / Volume 289

Biodegradation and microbial upcycling of plastics

J. de Witt (2025), XVI, 259 pp

ISBN: 978-3-95806-804-9

Band / Volume 290

**Practical Methods for Efficient Analytical Control in Superconducting
Qubits**

B. Li (2025), 202 pp

ISBN: 978-3-95806-807-0

Band / Volume 291

**Ab initio investigation of topological magnetism in two-dimensional van
der Waals heterostructures**

N. Abuawwad (2025), xviii, 135 pp

ISBN: 978-3-95806-808-7

Schlüsseltechnologien / Key Technologies

Band / Volume 291

ISBN 978-3-95806-808-7